



UNIVERSITETET I AGDER

DESIGN OPTIMIZATION OF VERTICAL PIPE
HANDLING SYSTEM

BY

GEIR-ARNE MOSLÅTT

MAY 31, 2012

SUPERVISOR:

MICHAEL RYGAARD HANSEN

CONFIDENTIAL

*This Master's Thesis is carried out as a part of the education at the
University of Agder and is therefore approved as a part of this education.*

*However, this does not imply that the University answers for the
methods that are used or the conclusions that are drawn.*

DEPARTMENT OF ENGINEERING

FACULTY OF TECHNOLOGY AND SCIENCE

Abstract

Due to the demand for high performance and reliability of the offshore systems from the industry the concern about finding the optimal components in a system is increasing. What is called optimal could vary, but keywords that are repeated include, performance, reliability, price and maintenance. To be able to predict the consequences of parameter changes and to a greater extent be able to improve the the system in the most cost-effective way, it is a key factor to have robust and accurate simulation models.

This project is based on the vertical pipe handler from Aker Solutions MH. A simulation model for this system is created in Matlab Simulink. The simulation model components are simulated and compared to data specification sheets to obtain correct properties. The motion control valve VAA-B-SICN-ST-250 is also lab-tested to verify and adjust the simulation model. The test was conducted to verify crack pressure settings, define spring stiffness, and obtain a realistic spool response.

The study explores the possibility of implementing the model in an optimization routine. The model used in optimization is simplified to only contain one of the drive lines of the bridge crane (the bridge travel). The simplified model contains a servo valve, over center valve, motors, and inertias and friction models describing the physical system. The model is used together with the so-called Complex optimization algorithm. The optimization examines the effect of changes in the controller parameter, valve frequency, load, and motion control valve parameters such as spring stiffness and pilot ratio. The results indicate that the optimal controller parameters are highly dependent on the load case. The investigation of the controller also showed that adding a velocity feedback gain to the existing controller (velocity forward gain and a position feedback PI-regulator) will improve accuracy with about 70%. The investigation of the directional servo valve response discovered that an improvement from 8.2Hz to 12Hz will improve the toolpoint position accuracy with over 20%.

Preface

I would like to express special thanks to the supervisor, Michael R. Hansen. In addition, I would like to thank Morten Bak for the help I have received with the execution of the experimental tests, and Anne Muller for guidance on the design and structure of the report.

Contents

Contents	2
List of Figures	6
List of Tables	10
1 Introduction	12
1.1 Motivation	12
1.2 Goal	14
1.3 Thesis outline	14
1.4 Project overview	15
2 Simulation Model	16
2.1 Introduction	16
2.2 Proportional Directional Valve, WRLE	18
2.2.1 Use and functionality	18
2.2.2 Model	19
2.3 Proportional Directional Valve, PVG 32	23
2.3.1 Use and functionality	23
2.3.2 LS pressure characteristics	24
2.3.3 Simulation model	25
2.4 Motion control valve	28
2.4.1 General use and functioning	28

CONTENTS

2.4.2	Motion Control Valve VAA-B-SICN-ST	31
2.4.3	VBSO overcenter valve	42
2.5	Hydraulic motors	49
2.6	Effective friction	52
2.7	Effective mass moment of inertia, BC	54
2.8	Effective mass and mass moment of inertia, LGA	57
2.8.1	Geometry LGA	58
2.8.2	Obtain $\theta_1(d_1)$	59
2.8.3	Local mass moment of inertia	61
2.8.4	Slewing MMI	65
2.8.5	Trolley travel MMI	68
2.8.6	Effective mass	69
2.9	Effective force due to gravity	71
2.10	Simulink model	73
2.10.1	Bridge Crane	73
2.10.2	Lower guiding arm	76
3	Experimental Test	77
3.1	Test introduction	77
3.2	Test rig and measure points	78
3.3	Test Sequences	79
3.4	Result	80
3.4.1	Test sequence 1	80
3.4.2	Test sequence 2	82
3.4.3	Test sequence 3	88
3.5	Comparing physical with simulated results	89
3.5.1	Crack pressure	90
3.5.2	Spring stiffness	91
3.6	Spool response	94
3.7	Sub-conclusions	97
4	Optimization of VPHS	98
4.1	Intro	98

CONTENTS

4.2	Optimization model	99
4.3	Design variables	101
4.4	Design criteria	102
4.5	The complex optimization algorithm	104
4.5.1	Optimization result	106
4.5.2	The controller	106
4.5.3	The servo valve parameters	112
4.5.4	The motion control valve parameters	114
4.6	Sub-conclusions	117
5	Conclusion	118
	Bibliography	120
A	Experimental test	121
A.1	intro	121
A.2	Measurement points	121
A.3	Test procedure	123
A.3.1	Test Setup	123
B	Measurement points, Bridge crane	127
C	Measurement points, Lower guiding arm	131
D	Functions, θ_1 and θ_3	135
E	Valve, Technical data	137
F	Further testing of the complex algorithm	146
F.1	Intro	146
F.2	Results	147
F.3	Effect of changing the error gain	149
F.4	Effect of changing the population	150
F.5	Effect of changing the boundaries	151
G	Simulink model of valve	152

CONTENTS

H	VBSO over center valve	154
I	Hydraulic Motor F12 series	156

List of Figures

1.1	Bridge crane and lower guiding arm [9]	13
1.2	Example of a general sub-system.	14
2.1	Servo solenoid valve 4WRLE-10...35 [3]	18
2.2	Block diagram of the proportional valve	19
2.3	Optimization of transfer function	20
2.4	Flow in control valve in mid position. Pressure drop at 5bar.	21
2.5	Valve port properties	22
2.6	Electrical actuated PVG[2]	23
2.7	Oil flow characteristic at LS pressure limiting	24
2.8	PVG hydraulic sheet	24
2.9	PVG characteristics [2]	25
2.10	Simulink model of PVG 32	27
2.11	Test setup	28
2.12	Velocity with and without mcv	29
2.13	Pressures on each side of overcenter valve	29
2.14	Cross-section and hydraulic chart of motion control valve VAA-B-SICN-ST [6]	31
2.15	Pressure loads	32
2.16	Real motion control valve – > simulated m.c.v.	35
2.17	Simulink model structure	36
2.18	Model for testing of motion control valve parameters	38

LIST OF FIGURES

2.19	Step by step procedure description	39
2.20	Simulation results compared with readings for the mcv [1]	40
2.21	VBSO [6]	42
2.22	Pressures and forces acting on the spool	43
2.23	Flow chart and simulink structure	46
2.24	Simulink block diagram of the calculation of the discharge area, a_1	47
2.25	Simulated overcenter valve response, compared with readings from datasheet [H]	48
2.26	Simulated motor, flowchart	49
2.27	Volumetric efficiency, F12 motor/pump[7]	50
2.28	Comparing simulated volumetric efficiency with readouts.	51
2.29	Coulomb + viscous friction model	52
2.30	Plot verifies the direction of the friction moment	53
2.31	Viscous friction dependent on velocity	53
2.32	Power transfer	54
2.33	Drawing of the LGA showing the functionalities implemented in the simulation model.	57
2.34	Geometry and location of center of mass. Global Z-axis and local ζ -axis works perpendicular to the paper plane pointing outwards	58
2.35	Mass centers	61
2.36	Simplified cross section	62
2.37	Box	64
2.38	The four parts of the LGA.	65
2.39	Interaction between the slewing axis and the motor shaft	67
2.40	Interaction between motor and trolley travel.	68
2.41	Effective mass dependent on cylinder positions	70
2.42	Simplified model of the LGA to calculate cylinder forces	72
2.43	BC model description	73
2.44	Simulation model bridge crane	74
2.45	Simualed results for trolley travel	75
2.46	Simulation model LGA	76
3.1	Test rig assembly	77

LIST OF FIGURES

3.2	Test rig diagram. <i>PVG: Proportional directional valve. MCV: Motion control valve</i>	78
3.3	Flow route through the valve during test	79
3.4	Opening pressure. Setting 1, 2, 3.	80
3.5	Results from test sequence 2	82
3.6	Test assembly overview of the measurement points	83
3.7	Spring stiffness vs flow and pressure	85
3.8	Compared results with and without the additional pressure force, p_F	87
3.9	Step response. 0% - 50%	88
3.10	Step response. 0% - 100%	88
3.11	Simulink model of test assembly	89
3.12	Difference (error) between the pressure drop across the spool ($p_3 - p_2$) in the simulation model and the experimental test	92
3.13	The flow force divided by the ring pressure area, A_r , giving p_F	93
3.14	Response when the PVG spool is stepped from 0 to 100% opening.	94
3.15	Response when the PVG spool is stepped from 0 to 50% opening.	94
3.16	Response plot with a PVG spool step from 0-100%.	95
4.1	Simulation model used for optimization	100
4.2	Original and new velocity reference	101
4.3	Second order high pass filter	102
4.4	Example of a signal with and without the high pass filter.	103
4.5	Population and centroid [4]	104
4.6	Worst design mirrored over the centroid [4]	104
4.7	Block diagram of the controller	106
4.8	Optimized K_v , relative to position error and load	107
4.9	Modified controller	108
4.10	Comparison of position and velocity error with (right side) and without (left side) a controller with proportional velocity error gain.	109
4.11	Comparison of the pressures with (right side) and without (left side) a controller with proportional velocity error gain.	109
4.12	Max position error for each load case, with and without the modified controller.	110

LIST OF FIGURES

4.13	Friction moment during the simulation. The results are simulated with the parameters from table 4.3	111
4.14	Spool position and the integrated error	112
4.15	Results of spool response test.	113
4.16	Optimized design of pilot ratio and spring stiffness. Note: the bars for the cost function, C_{vib} continues to a cost of 10353 and 10551.	115
4.17	The effect of vibration reduction in the inlet pressure on the motor.	116
A.1	Measurepoints	122
F.1	Effect of changing the parameter K. $C = 3$, $B = \pm 60\%$	149
F.2	Deviation dependent on population. Stats from tabular F.1. Blue bars has a deviation $< 0.4\%$, red has $< 2\%$ and $> 0.4\%$	150
F.3	Deviation dependent on parameter boundaries	151
G.1	Simulink model of directional control valve	153

List of Tables

2.1	Oil specifications in simulation models.	17
2.2	PVG settings in simulated model	26
2.3	Data from drawing sheet, see appendix C	27
2.4	Overcenter valves, Bridge crane, [6]	30
2.5	Overcenter valves, LGA, [6]	30
2.6	Variable table	34
2.7	The parameters determined through the test	37
2.8	Best parameter results for VAA-B-SICN-ST valves	41
2.9	Results from experimental test in chapter 3	41
2.10	Best parameter results for the VBSO-DE-CC valve	48
2.11	Temporary variables. <i>*Where bar is the force divided by the ring area, A_r, and one unit represent the spool movement from 0 to 1.</i>	49
2.12	Variables in eq 2.26	50
2.13	Discharge areas, volumetric efficiency	51
2.14	MMI caused by moving mass presented on motor shaft. Masses and geometry values were obtained in component drawings	55
3.1	Measure points	78
3.2	Crack pressures, test settings and results	81
3.3	Crack pressures from experimental test and simulation	90
3.4	Multistep results	91
4.1	Design parameters	101

LIST OF TABLES

4.2	Optimized position parameters, for different load cases	108
4.3	Optimized position parameters for different friction coefficients . .	111
4.4	Parameters obtained in optimization	115
A.1	Measure points, bridge crane	124
A.2	Measure points, lower guiding arm	125
F.1	Experimental data	148

Introduction

1.1 Motivation

The current vertical pipe handling system (VPHS) of Aker Solutions, is basically a combination of two machines (bridge crane and lower guiding arm (fig 1.1)). They must move in a coordinated manner in order to move pipe stands to or from the drill center. There is an increasing demand for improved performance with the dominant criteria being reliability. Other important criteria are: price, speed, accuracy, ease of maintenance and efficiency.



Figure 1.1: Bridge crane and lower guiding arm [9]

1.2 Goal

The project has mainly three goals. Firstly, precise and accurate models of the components in the bridge crane and lower guiding arm should be created. To ensure the accuracy of the models experimental test work will be introduced. The test results will verify or lead to modifications on the simulation model such that the model will maintain a sufficient accuracy. In this context a sufficiently accurate model is one that can be used for design optimization. This test will focus on the motion control valves. The motion control valves are essential in the hydraulic sub-systems, and is located between the hydraulic actuator and the directional valve (fig 1.2).

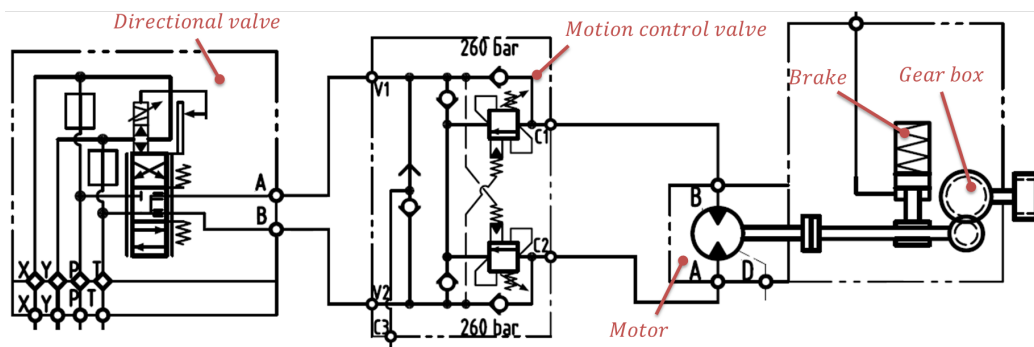


Figure 1.2: Example of a general sub-system.

Secondly, the obtained simulation components will be assembled to create a model of the VPHS. Thirdly, an optimization routine should be performed to discover how the system parameters could be changed to improve the system performance. This will demand a simulation model where the complexity have been reduced with a view to reduce simulation time without compromising accuracy.

1.3 Thesis outline

The thesis starts with the development of the simulation model components. This involves assumptions and modeling methods that are used to simulate the system components. These components are combined to yield the model of the lower guiding arm (LGA) and the bridge crane (BC). Next the experimental work is presented with the test procedures to verify and calibrate the simulation model of the motion control valve (MCV). The results are compared to the simulation model and evaluated. In the end of the thesis the Complex optimization algorithm is introduced, and is applied to optimize part of the bridge crane.

1.4 Project overview

- Simulation models of each component in the VPHS are created.
- A simulation model of the VPHS is developed. The model is made to simulate the dynamic behavior in the time domain.
- An experimental test is performed to explore and verify the parameters in the MCV used on the bridge crane.
- An optimization procedure and implementation is described.

Simulation Model

2.1 Introduction

This chapter deals with the structure and composition of the two models, "bridge crane" and "lower guiding arm". To get a practical and fast running model it is useful to do some simplifications. It is important that the approximation is done properly to avoid large deviations from the exact physical result. The following 3 assumptions are made. First of all a stiff mechanical structure is assumed. This assumption says that the guide mast which connects the gripper head to the trolley is infinitely stiff. This is of course not completely true, but because the complex structure of the guide mast and the fact that it actually are quite stiff. It is assumed that this will not affect the overall model in any large scale. Secondly the ring line pressure supply is assumed constant and independent of flow consumption. Hence, it is assumed that the hydraulic power unit can deliver the required amount of flow without losing the pressure. The ring line pressure is assumed to be 207bar. Finally the third assumption is the friction models. In motors, bearings, gears, sliders and so on the friction is represented as a simple coulomb or viscous friction force. No hysteresis or stiction models are used. It is assumed that this will not give any major deviations compared to the physical system, since the crane does not have any oscillating movement patterns and high velocities. If this

CHAPTER 2. SIMULATION MODEL

where the case a more advanced model should be used because the effect of the friction force would be larger.

The following sections in this chapter will deal with the modeling of each component in the the vertical pipe handler. All models are created with Matlab simulink in time domain. The oil used in the hydraulic circuits has a fluid density of $850\text{kg}/\text{m}^3$, a kinematic viscosity $1.8 \cdot 10^{-5}\text{m}^2/\text{s}$, and a bulk modulus of $8 \cdot 10^8\text{Pa}$ (table 2.1)

Parameters	
Fluid density	850 kg/m^3
Kinematic viscosity	$1.8 \cdot 10^{-5}$ m^2/s
Bulk modulus	$8.0 \cdot 10^8$ Pa

Table 2.1: Oil specifications in simulation models.

2.2 Proportional Directional Valve, WRLE

2.2.1 Use and functionality

All three directions of the gripper head (trolley travel, bridge travel and slewing) on the bridge crane are controlled by the same type of directional valve, 4WRLE 16 WZ180SJ-3X/G24ETK0/A1M. This servo valve has a positive overlap and on-board electronics (fig 2.1).

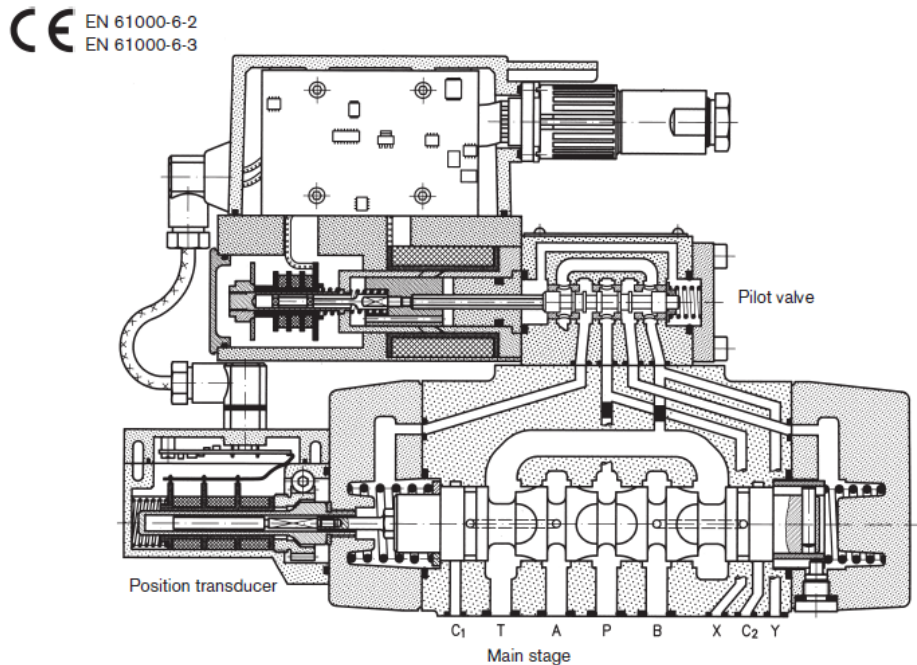


Figure 2.1: Servo solenoid valve 4WRLE-10...35 [3]

2.2.2 Model

The valve is modeled as four variable area orifices in simulink. These four orifices are determined through the input signal and the given valve properties (appendix E and G). To obtain the correct dynamics for this valve, a second order transfer function is added to the input signal. This transfer function would then express the response of the spool as if it was a mass connected to a damper and a spring.

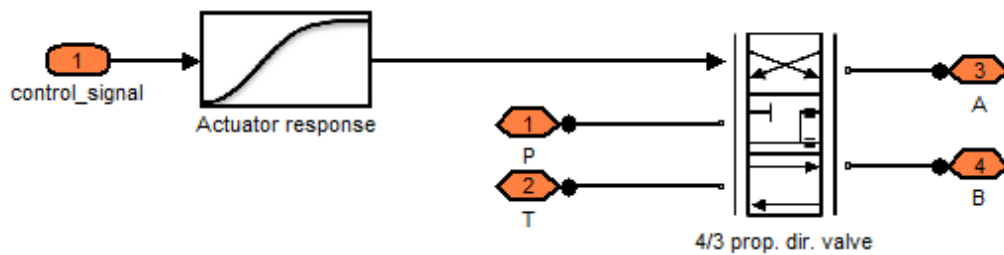


Figure 2.2: Block diagram of the proportional valve

The response block (fig 2.2) contains the second order valve response, described in the technical data sheet(see appendix E). To obtain this second order response as a transfer function with correct parameters, the response plot from the data sheet was converted manually to points. Then these points were used together with a general second order transfer function (eq; 2.1) inside an optimization algorithm (the complex method).

The 2nd order transfer function representing the spool response is,

$$TF_{2.nd} = \frac{\omega_n^2}{s + 2 \cdot \zeta \cdot \omega_n \cdot s + \omega_n^2} \quad (2.1)$$

where ζ is the damping ratio and ω_n is the natural frequency. When using a optimization algorithm it is needed to have a cost function. This cost function represents the error of the results and the optimization algorithm tries to minimize it. In this case the cost function was set to be the sum of the squared error. Eleven points were read out from the data sheet curve, and the defined cost function were

dependent on deviation between each point and estimated step response. Thus,

$$E = \sum_1^n E_i^2 \quad (2.2)$$

where E_i is the deviation between the reading and simulated value at point i , and n is the total amount of points, in this case 11.

The optimization gave a response that corresponds well to the response given in the data sheet[3]. In fig 2.3 the red dots indicate the values of the response curve in the data sheet, while the black line indicates the final simulated design. The blue lines indicates tested responses before the algorithm settles on the black line.

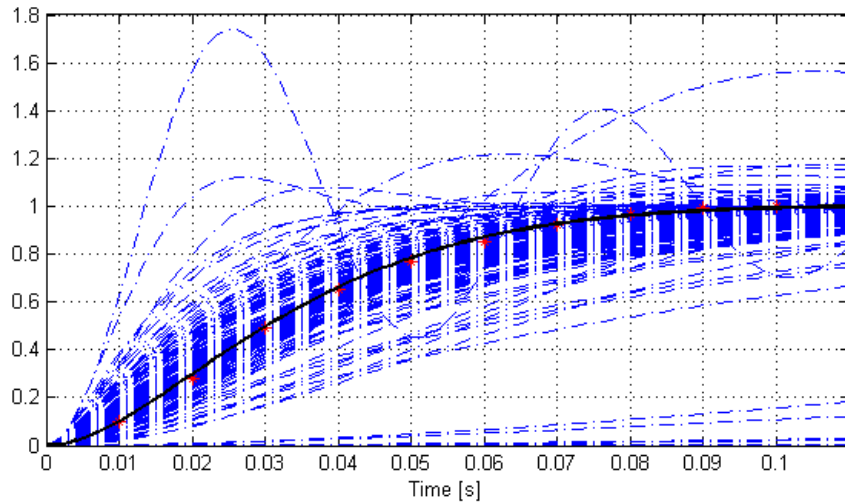


Figure 2.3: Optimization of transfer function

The result gave a response with a frequency about $52.6rad/sec$ and a damping ratio of 0.90. This gave an error of $E = 8.1 \cdot 10^{-4}$ due to the cost function eq.2.2.

CHAPTER 2. SIMULATION MODEL

Next, the maximum discharge areas and deadband was determined. These properties were obtained by looking at the flow charts in the data sheet (see "flow in mid position" and "technical spec" in appendix E). The data sheet describes the flow around the flow characteristics at a pressure drop of 5bar. From the technical specifications and graphics, the nominal flow at a pressure drop of 5bar is 180l/min if the valve is fully opened. From this fact and the orifice equation, the maximum discharge area was determined to be $125mm^2$. To determine the discharge area in the deadband area the data sheet gave the following plot shown in fig 2.4.

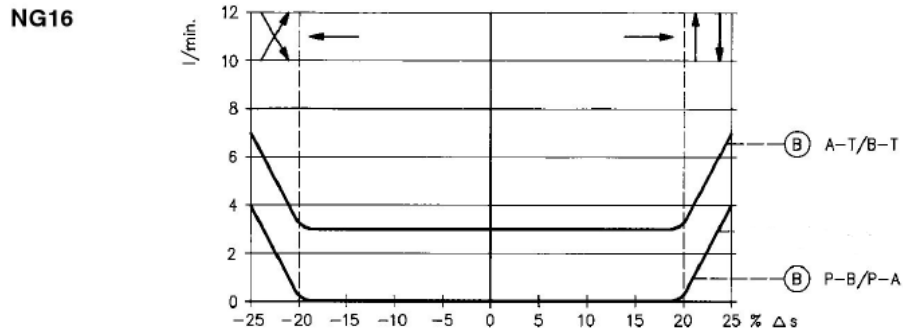


Figure 2.4: Flow in control valve in mid position. Pressure drop at 5bar.

At 5Bar pressure drop, the nominal flow between A-T and B-T is 3l/min in the mid position. With this flow and pressure specification the discharge area for these ports deadband zone ($\pm 2\%$) was determined. The area was calculated to be $2.1mm^2$.

$$Q = A_d C_D \sqrt{\frac{2}{\rho} \Delta p} \quad C_D = 0.7 \quad \rho = 850 kg/m^3 \quad \Delta p = 5bar$$

Hence, the following areas were found:

$$Q = 180l/min \rightarrow A_{d,max} = 124.9mm^2 \quad Q = 3l/min \rightarrow A_{d,min} = 2.1mm^2$$

CHAPTER 2. SIMULATION MODEL

Below the deadband zone it was assumed that the area was ramped to zero over the next 20% (fig 2.5). This was assumed since it was not possible to extract this information from the data sheet. Because of that assumption and the previously determined areas, the following properties for the simulated valve was obtained (fig 2.5).

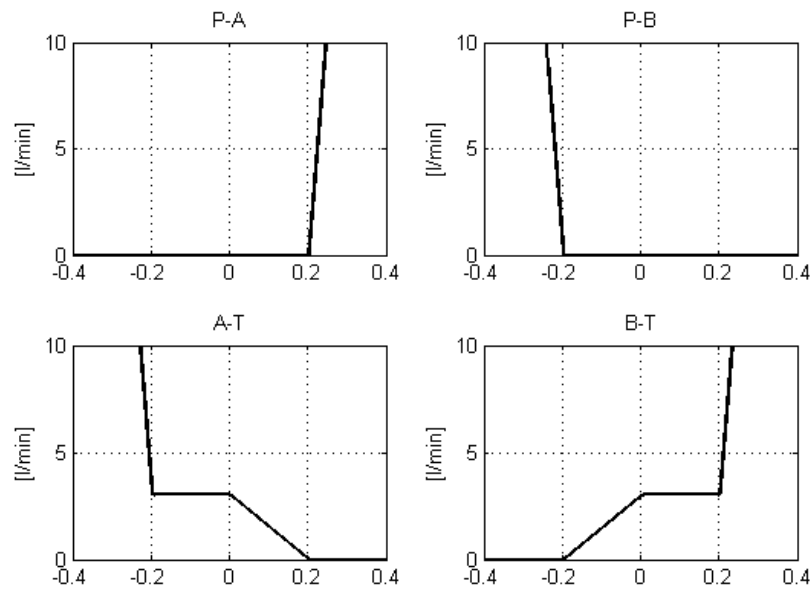


Figure 2.5: Valve port properties

The figure show the flow characteristics around the deadband. The deadband corresponds to the deadband given in fig 2.4 and the deadband flow to tank (A-T and B-T) is 3 l/min .

2.3 Proportional Directional Valve, PVG 32

2.3.1 Use and functionality

The lower guiding arm uses the proportional valve PVG 32, which is an electrical actuated valve. This valve is also pressure-compensated to keep a pressure drop of 7 bar over the valve. The use of constant pressure drop give a flow rate proportional to the control signal, and is due to this easier to control.

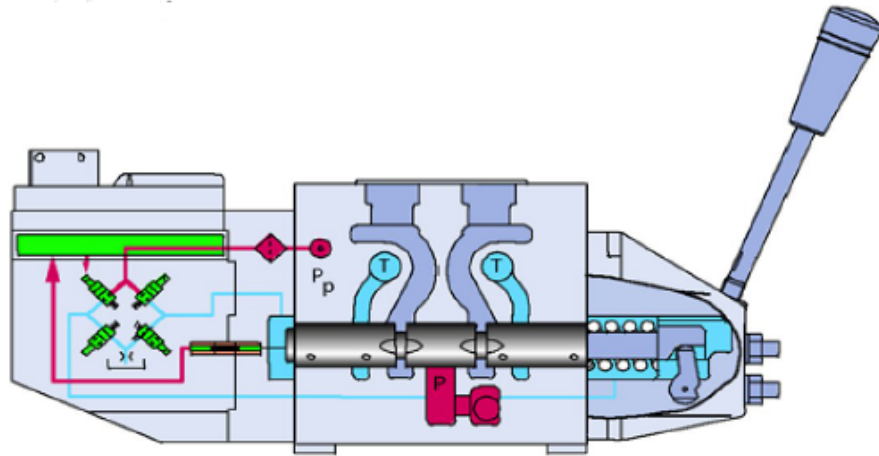


Figure 2.6: Electrical actuated PVG[2]

2.3.2 LS pressure characteristics

A common problem when closing into the LS pressure, is flow loss (fig 2.7).

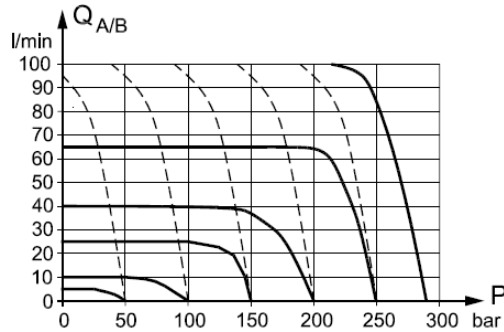


Figure 2.7: Oil flow characteristic at LS pressure limiting

This flow loss is actually caused by the LS pressure setting and a reduced pressure drop over the PVG. As the pressure approach the LS pressure the relief valve(2) will slowly open up about 60bars bellow crack pressure. This will create a small flow through the relief valve(2) and the orifice(1). This flow will create a pressure loss and the measured pressure sent to the pressure compensator will then be lower than the actual pressure at the output port(3). The controller will therefor "assume" that the pressure drop over the control valve is correct while it actually is bellow. As the pressure is increased the flow and pressure drop over the spool is reduced. When the the pressure reaches the LS pressure the relief valve has fully opened and the flow through the PVG has reached zero.

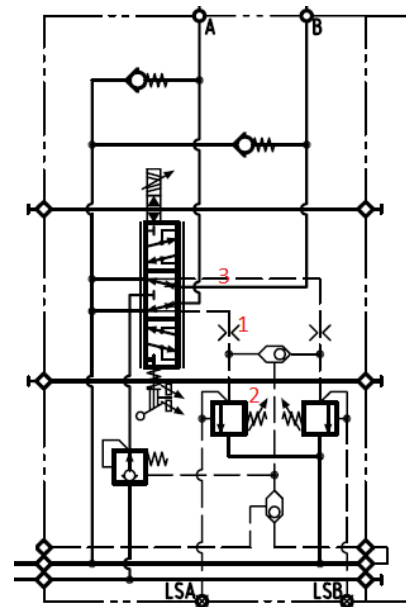


Figure 2.8: PVG hydraulic sheet

2.3.3 Simulation model

The PVG has the same functionality as the 4/3 servo valve (2.2), only this valve has different deadband and opening areas. The deadband was set to 0.8mm due to the specifications for a linear PVG. The maximum discharge area and the discharge area in neutral was determined due to the flow curves for a 100l/min spool (curve E in fig 2.9a and 2.9b) and the orifice equation,

$$Q = A_d C_D \sqrt{\frac{2}{\rho} \Delta p} \quad C_D = 0.7 \quad \rho = 850 \text{ kg/m}^3$$

This give,

$$\begin{aligned} Q = 100 \text{ l/min}, \quad \Delta p = 7 \text{ bar} & \quad \rightarrow \quad A_{d,max} = 58.7 \text{ mm}^2 \\ Q = 60 \text{ l/min}, \quad \Delta p = 205 \text{ bar} & \quad \rightarrow \quad A_{d,min} = 6.5 \text{ mm}^2 \end{aligned}$$

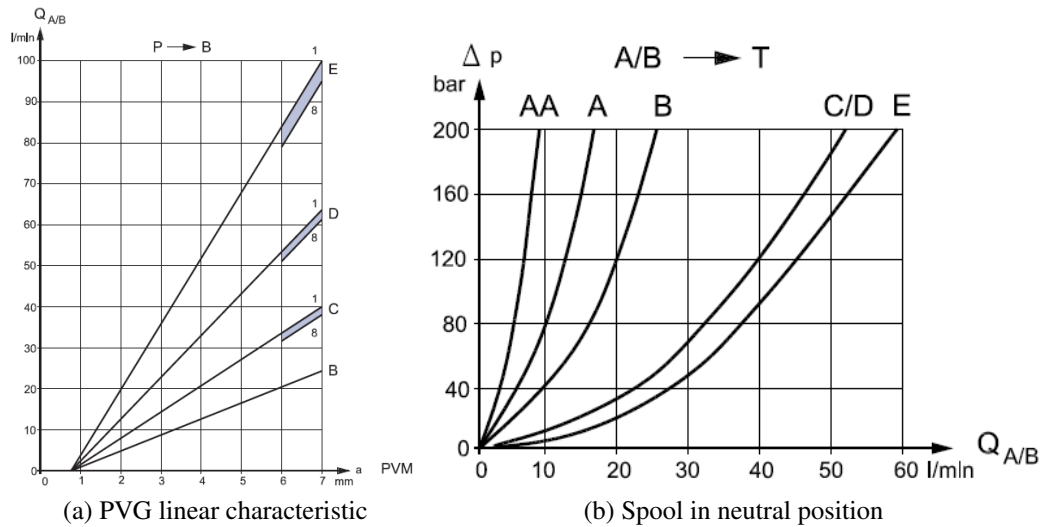


Figure 2.9: PVG characteristics [2]

The spool response was set to a second order transfer with a frequency of 30rad/sec and damping ratio of 0.8. These values is based on earlier test results [5] by Morten Kollerup Bak.

The parameters needed to simulate the valve is now obtained. The simulation model of the valve has three main parts (fig 2.10). Firstly the 4/3 valve functionality with the right spool travel, deadband, and discharge areas (table 2.2). Secondly is the response block which contains the second order transfer function. And the third main part is the pressure compensator. In this case the compensator is simulated as a function coupled to a ideal pressure source. The function is dependent on the output pressure of the PVG and controls the ideal source to keep a pressure 7bar above the output. When the output pressure passes the LS-pressure minus 60bar the function make the pressure drop linearly drop to zero as the output pressure goes towards the LS-pressure, corresponding to fig 2.7. To avoid singularity the function is coupled to a response block and to avoid that this would affect the model the response frequency was set very high ($\omega = 1000rad/sec$).

Max spool travel	$\pm 7mm$
Deadband	$\pm 0.8mm$
Neutral discharge area to tank	$6.5mm^2$
Maximum discharge area	$58.7mm^2$
Response frequency	$30rad/sec$
Response damping ratio	0.8

Table 2.2: PVG settings in simulated model

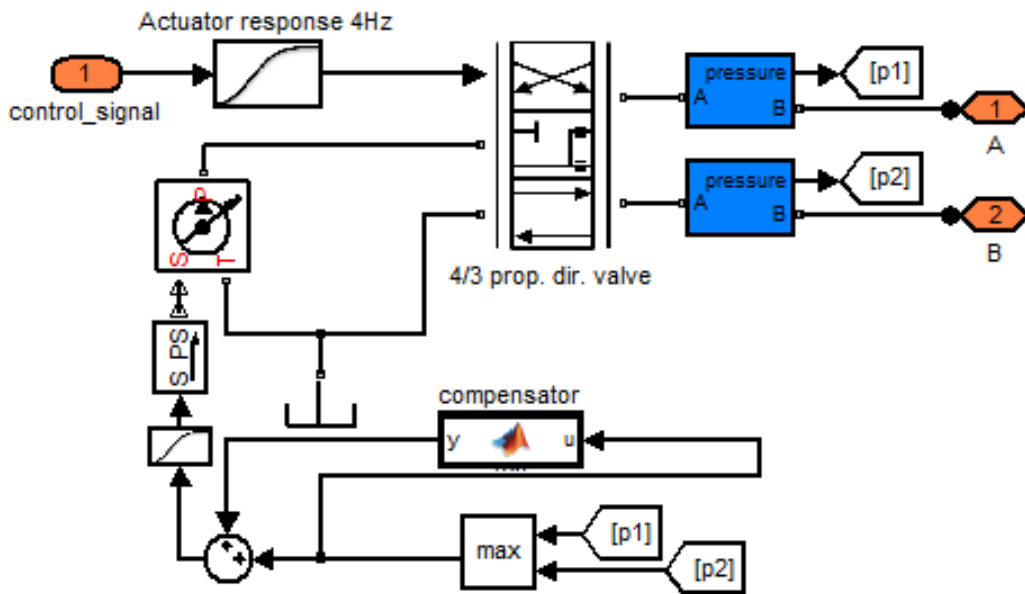


Figure 2.10: Simulink model of PVG 32

The LS pressure settings on the Iga is given from the drawing sheets. The LS pressure used is shown in table 2.3.

Output	Trolley Travel		Jib Tilt		Telescope		Slewing	
	A	B	A	B	A	B	A	B
LS [bar]	207	207	190	190	140	140	207	207
Q [l/min]	78	78	80	49	80	56	53	53
v [mm/s]	600	600	110	110	265	265	30 [°/s]	30 [°/s]
Descr.	FWD	AFT	EXTEND	RETRACT	EXTEND	RETRACT	CW	CCW

Table 2.3: Data from drawing sheet, see appendix C

2.4 Motion control valve

2.4.1 General use and functioning

Motion control valves is used over every motor in the hydraulic system. The valve is primarily used for increased stability during load lowering (negative load). The valve also equalize the difference in acceleration and deceleration for the same spool position (u and $-u$), and therefor make the system easier to control. The check valves between p_t and p_{v1}, p_{v2} (fig 2.14) will prevent cavities in the oil. That the mcv equalizes the difference in acceleration and deceleration, and prevent cavities are shown in the following example/test. The test contains a constant pressure source, $p_p = 260bar$ (fig 2.13). The flow from the pressure source goes through an orifice with a variable discharge area. The area is ramped up and down as shown in fig 2.11, giving an increase and decrease in flow through the system. The rest of the system consists of a motor subjected to a constant force in opposite direction of the velocity (could for instance illustrate a coulomb friction force), and an orifice to tank. The system is simulated with and without over center valve.

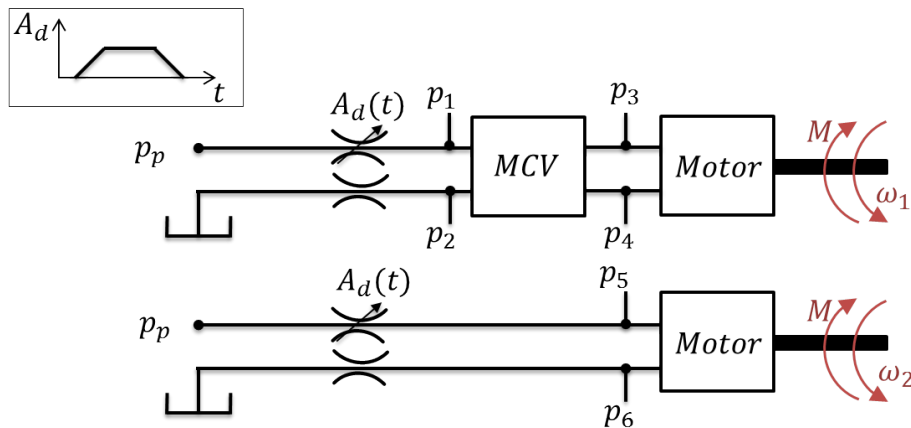


Figure 2.11: Test setup

The results highlighted the functionality of the motion control valve. It gave a stable and more even deceleration compared to the test with no implemented motion control valve (fig 2.11). In the system with no mcv, the pressure falls below 0bar. This is a sign of cavitation, which can cause instability due to low oil stiffness. On the system which has a motion control valve the cavitation is gone and the pressure settles at 0bar (fig 2.13).

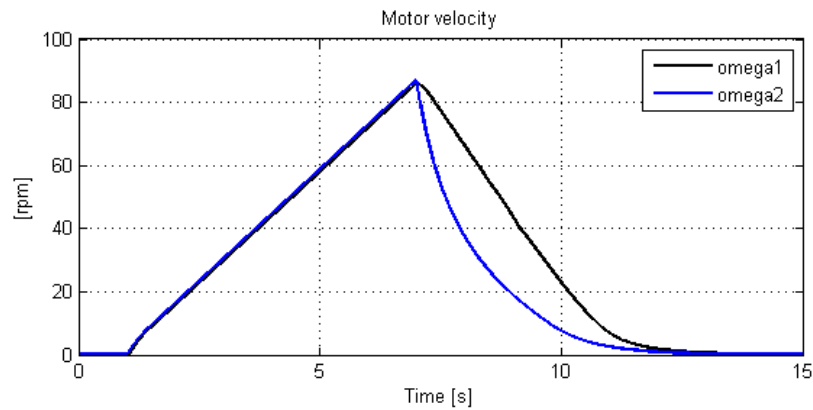


Figure 2.12: Velocity with and without mcv

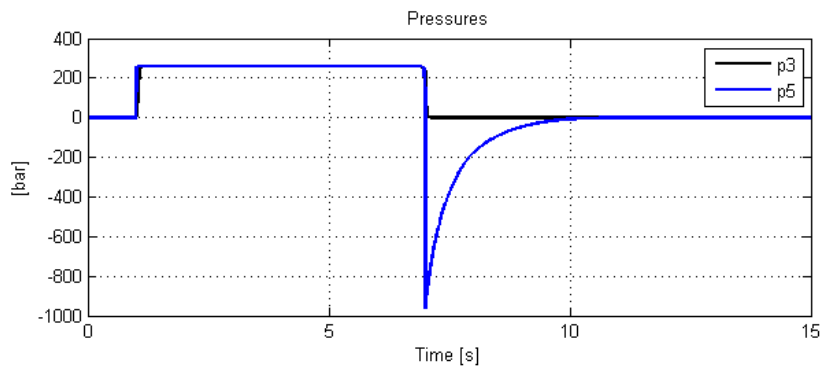


Figure 2.13: Pressures on each side of overcenter valve

CHAPTER 2. SIMULATION MODEL

The vertical pipe handler crane has many different motion control valves, but for this specific simulation model, those in table 2.4 and 2.5 are needed.

Type	Place	Pilot ratio	Crack pressure
VAA-B-SICN-ST-VF250	Bridge travel	2.8	230bar/230bar
VAA-B-SICN-ST-VF250	Trolley travel	2.8	260bar/260bar
VAA-B-SICN-ST-VF250	Slewing	2.8	270bar/270bar

Table 2.4: Overcenter valves, Bridge crane, [6]

Type	Place	Pilot ratio	Crack pressure
VAA-B-SICN-ST-VF050	Trolley travel	9.1	200bar/200bar
VAA-B-SICN-ST-VF150	Slewing	3	200bar/200bar
VBSO-DE-CC	Jib tilt	3.2	100bar/230bar
VBSO-DE-CC	Telescope	3.2	100bar/140bar

Table 2.5: Overcenter valves, LGA, [6]

The VAA-B-SICN-ST valves has the same functionality principle but with different sizes (VF050, VF150, VF250). Each size has its own flow-pressure characteristics, and therefor need individual adjustment. In the next sections the functionality of the VAA-B-SICN-ST valves and VBSO-DE-CC valves will be explained as well as the modeling and individual adjustments.

2.4.2 Motion Control Valve VAA-B-SICN-ST

Valve information

The valve provides a static and dynamic motion control by regulating the flow and pressure in and out of the hydraulic motor at ports C1 and C2. If the valve is placed close to the motor it will also stop runaway in case of hose failure. The check valves allow free flow into the motor and prevent reverse movement and the pilot assisted relief valves control the movement when pilot pressure is applied. The system of check valves at the end of each relief valve allows cross line relief (after crossing the pressure relief valve, the flow continuous either line one or line two, dependent on where the pressure is the lowest). Through port C3 (brake release port) a shuttle valve directs the highest pressure from V2 and V1 to the spring actuated brake for brake releasing. In this way the brake will always be on as long as maximum system pressure is bellow the needed brake release pressure.[6]

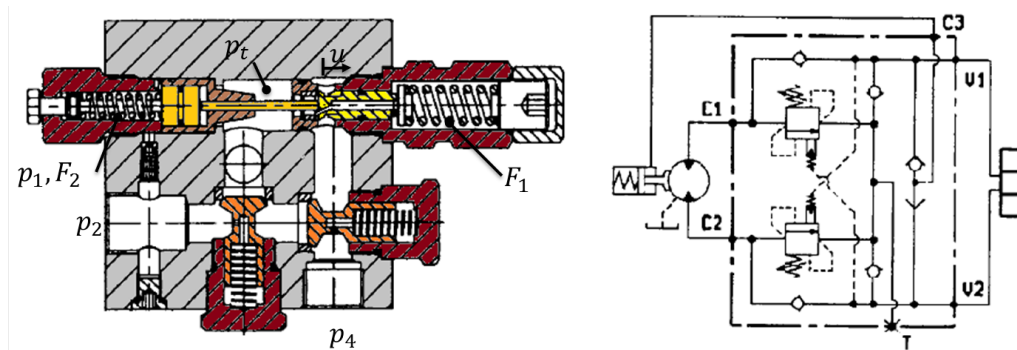


Figure 2.14: Cross-section and hydraulic chart of motion control valve VAA-B-SICN-ST [6]

The pressure relief valve opening

To calculate the spool position a static equilibrium is assumed. Hence, the valve opening is given by the pressure forces and the spring stiffness.

From fig 2.14 the static equilibrium state of the yellow spool was derived. The cross section in fig 2.14 show the valves between V2 and C2. By looking at the pressure in each chamber the figure 2.15 was drawn. The figure show the two parts of the spool and the pressures working on it. The pressures are pushing on different areas and the areas are shown in cross section A and B (fig 2.15). Since the spool has two parts it is necessary to have an equilibrium equation that depends on whether they are in contact or not. Hence the force N ,

$$\sum F = 0 \rightarrow N_2 A_r = p_1 A_r \alpha - p_t A_r \alpha + (p_{cr2} - k_{p2} \cdot u_2) A_r \quad (2.3)$$

$$\sum p = \frac{\sum F}{A_r} = 0 \rightarrow N_2 = p_1 \cdot \alpha - p_t \cdot \alpha + p_{cr2} - k_{p2} \cdot u_2 \quad (2.4)$$

where the pressures corresponds to the pressures subjected to the left spool piece (fig 2.15) and α is the pilot ratio. The p_{cr2} and k_{p2} is crack pressure and spring stiffness relative to the ring area A_r . While N is larger than zero the two pieces are in contact and the forces on the left piece will try to open the valve (push the right spool to the right).

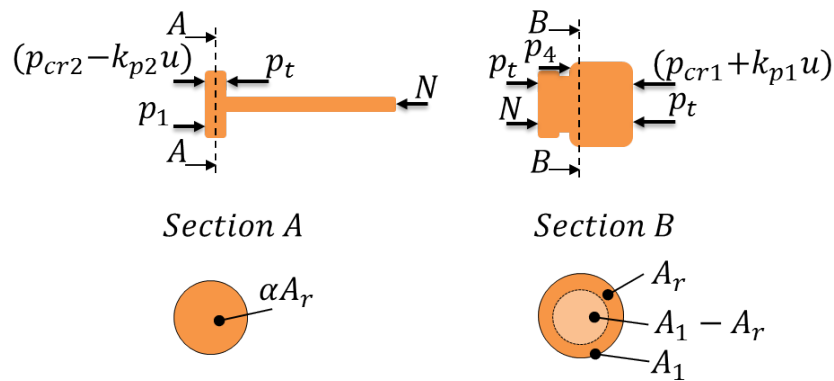


Figure 2.15: Pressure loads

The equilibrium forces on the right spool determines the discharge area for the flow from C2 to V2. An equilibrium equal or less than zero means that the spool

CHAPTER 2. SIMULATION MODEL

is pushed to the position zero. Dependent on the spring stiffness and the pressures the static position of the spool is determined.

Equilibrium for the pressure relief valve between V2 and C2 is,

While $N_2 < 0$

$$\sum F = p_t(A_1 - A_r) + p_4 \cdot A_r - (p_{cr1} + k_1 \cdot u_2) \cdot A_r - p_t \cdot A_1 \quad (2.5)$$

$$\sum p = p_{eq} = -p_t + p_4 - (p_{cr1} + k_{p1} \cdot u_2) \quad (2.6)$$

Static solution, hence $p_{eq} = 0$ gives:

$$u_2 = \frac{p_4 - p_t - p_{cr1}}{k_{p1}}, \quad 0 \leq u_2 \leq 1 \quad (2.7)$$

While $N_2 > 0$

$$\sum F = p_1 \alpha A_r + (p_{cr2} - k_2 \cdot u_2) A_r - p_t \alpha A_r + p_t(A_1 - A_r) + p_4 A_r - (p_{cr1} + k_1 \cdot u_2) A_1 - p_t A_1$$

$$\sum p = p_{eq} = \frac{\sum F}{A_r} \quad (2.8)$$

$$p_{eq} = p_1 \alpha + p_{cr2} - k_{p2} \cdot u_2 - p_t \alpha + p_t \left(\frac{A_1}{A_r} - 1 \right) + p_4 - (p_{cr1} + k_{p1} \cdot u_2) - p_t \left(\frac{A_1}{A_r} \right) \quad (2.9)$$

$$p_{eq} = p_1 \alpha + p_{cr2} - k_{p2} \cdot u_2 - p_t(\alpha + 1) + p_4 - p_{cr1} - k_{p1} \cdot u_2 \quad (2.10)$$

Static solution, hence $p_{eq} = 0$ gives:

$$u_2 = \frac{p_1 \cdot \alpha + p_{cr2} - p_t(\alpha + 1) + p_4 - p_{cr1}}{k_{p1} + k_{p2}}, \quad 0 \leq u_2 \leq 1 \quad (2.11)$$

The equation 2.11 give the opening position of the relief valve between port C2 and V2, given by the pressures and the spring stiffness. The static equilibrium for the pressure relief valve between V1 and C1 is identical, except $p_1 \rightarrow p_2$, and $p_4 \rightarrow p_3$.

CHAPTER 2. SIMULATION MODEL

Static equilibrium for the pressure relief valve between V1 and C1,

While $N_1 < 0$

$$u_1 = \frac{p_3 - p_t - p_{cr1}}{k_{p1}}, \quad 0 \leq u_1 \leq 1 \quad (2.12)$$

While $N_1 > 0$

$$u_1 = \frac{p_2 \cdot \alpha + p_{cr2} - p_t(\alpha + 1) + p_3 - p_{cr1}}{k_{p1} + k_{p2}}, \quad 0 \leq u_1 \leq 1 \quad (2.13)$$

where u_1 is the position of the spool in line 1 (between C1 and V1), p_t is the pressure in the end of the relief valves, p_{cr} and k_p is the crack pressure and spring stiffness due to the springs.

A_r	: Ring pressure area, which is related crack pressure
p_{cr1}	: Crack pressure, spring 1, [Pa]
k_{p1}	: Stiffness spring 1, Pascal per unit displacement of u, [Pa/unit]
p_{cr2}	: Crack pressure, adjustable, spring 2, [Pa]
k_{p2}	: Stiffness spring 2, Pascal per unit displacement of u, [Pa/unit]
α	: Pilot pressure ratio
p_1	: Pressure at V1, see fig 2.14, [Pa]
p_2	: Pressure at V2, see fig 2.14, [Pa]
p_3	: Pressure at C1, see fig 2.14, [Pa]
p_4	: Pressure at C2, see fig 2.14, [Pa]
p_t	: Pressure between relief and check valve, see fig 2.14, [Pa]
u_i	: Spool position for line 1 or 2 ($i = 1$ or $i = 1$). Saturates at zero and one

Table 2.6: Variable table

Simulink model

The motion control valve (fig 2.16) is simulated with two orifices with variable discharge area. One for each relief valve and four check valves (all from simscape library in matlab). The variable discharge areas were calculated through the pressure/force equilibrium equations (eq:2.10 and 2.13). When this equilibrium is equal or less than zero, the valve is closed.

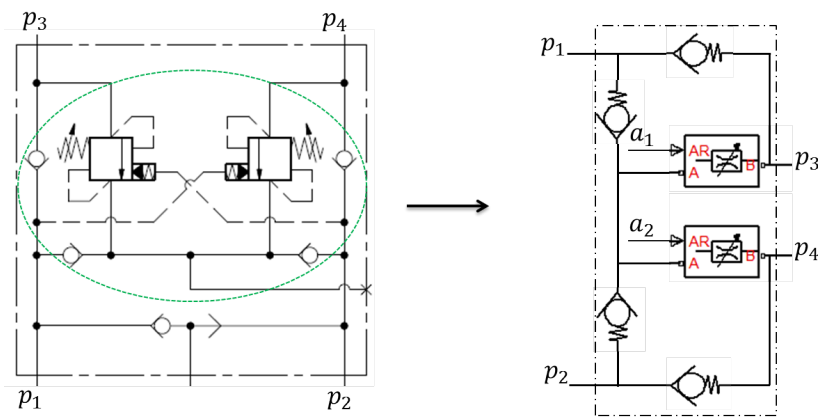


Figure 2.16: Real motion control valve – > simulated m.c.v.

Assumed that the discharge area increase linearly with the spool position, the variable discharge area was calculated based on the pressures pressure equilibrium defining u (eq.2.13) and $A_{d,max}$, hence,

$$a_1 = u_1 \cdot A_{d,max} \quad (2.14)$$

$$a_2 = u_2 \cdot A_{d,max} \quad (2.15)$$

where a_1 and a_2 are the discharge areas for pressure relief valve 1 and 2 and corresponds to the a_1 and a_2 in fig 2.16, and u_1 and u_2 are calculated through equation 2.13 and 2.11. The spring stiffness for the springs on each side of the relief valve determines when the valve is fully open ($u = 1$, see eq 2.11 and 2.7), and are therefore important parameters. The spring stiffness parameter is not given in the datasheets and will be determined with some valve testing in section 3.4.2.

CHAPTER 2. SIMULATION MODEL

The Simulink model structure contains mainly 3 parts (fig 2.17). Firstly the equilibrium equation determine the static position of the spool. Second part is the dynamic response of the spool inserted as a transfer function. The third and last part is the hydraulic model with orifices and check valves.

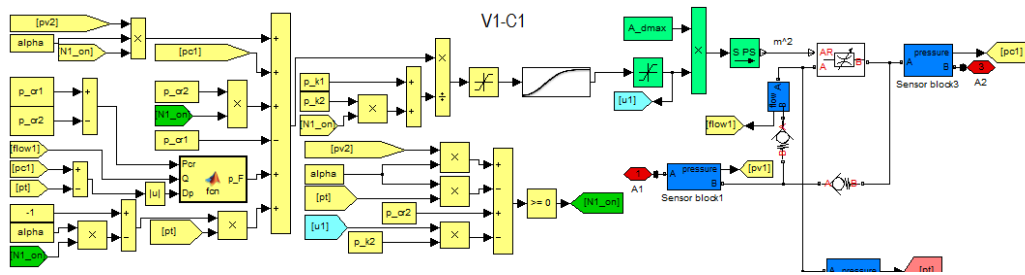


Figure 2.17: Simulink model structure

Tuning motion control valve parameters

To obtain good model for the overcenter valve it is important to have the right parameter values. Some of these values is obtained through some simulations and comparisons to specifications from the data sheet[6]. These are the parameter values that belong to the check valves and the maximum opening area of the relief valves. The values that cannot be evaluated this way are the crack pressures, the spring stiffness and the spool response. These parameters looked into in chapter 3. The test simulation was executed with a simple model (fig 2.18). The model was built to determine the parameters based on some flow curves taken from the data specification sheet[6]. The data sheet gave flow curves through V1/V2 to C1/C2, and C1/C2 to V1/V2 when the spool was fully opened. With this data the maximum discharge areas for check valves and pressure relief valves could be obtained, as well as some crack pressures and areas for the check valves.

$A_{m,prv}$:	Maximum discharge area in the pressure relief valve
p_{cr1} :	Crack pressure, check valve 1
$A_{m,cv1}$:	Maximum passage area, check valve 1
$p_{max,cv1}$:	Maximum opening pressure, check valve 1
p_{cr2} :	Crack pressure, check valve 2
$A_{m,cv2}$:	Maximum passage area, check valve 2
$p_{max,cv2}$:	Maximum opening pressure, check valve 2

Table 2.7: The parameters determined through the test

To perform this test, a model was built in simulink. The connection between V and C only have a check valve, referred to as check valve 1, and the other direction (from C to V) was simulated with an orifice in series with a check valve, referred to as check valve 2 (2.18). The orifice illustrates a fully opened pressure relief valve.

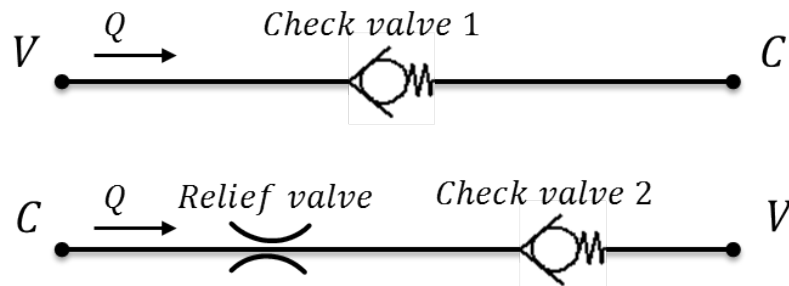


Figure 2.18: Model for testing of motion control valve parameters

The simulation was executed by connecting a ideal flow source to each test model (fig 2.18), The flow was ramped to $200l/min$. The results were compared to readings from the actual curves in the data sheet.

To determine these parameters (table 2.7) a certain approach was used. This approach is explained below step by step. Each step has a number which refers to the numbers in fig 2.19 (except step 5 which refers to point 3).

1. Determine the maximum discharge area in "check valve 1" by giving the valve a pressure drop of the last given value in the data sheet. Use the same pressure drop and tune in the discharge area to get the correct flow. The flow and area are in this case linearly dependent.
2. Adjust your crack pressure to fit the given reading at flow equal zero.
3. Move the breakpoint by adjusting the maximum opening pressure. Check valve 1 is now fully determined.
4. Set the maximum discharge area in check valve 2 equal the check valve 1. Then determine the maximum discharge area in the pressure relief valve,

by the same procedure as in point 1. Because of the check valve coupled in series the flow and area is no longer linearly dependent.

- Set the crack pressure to 0.1bar, and start with the fine tuning your plot by changing the maximum opening pressure as in point 3.

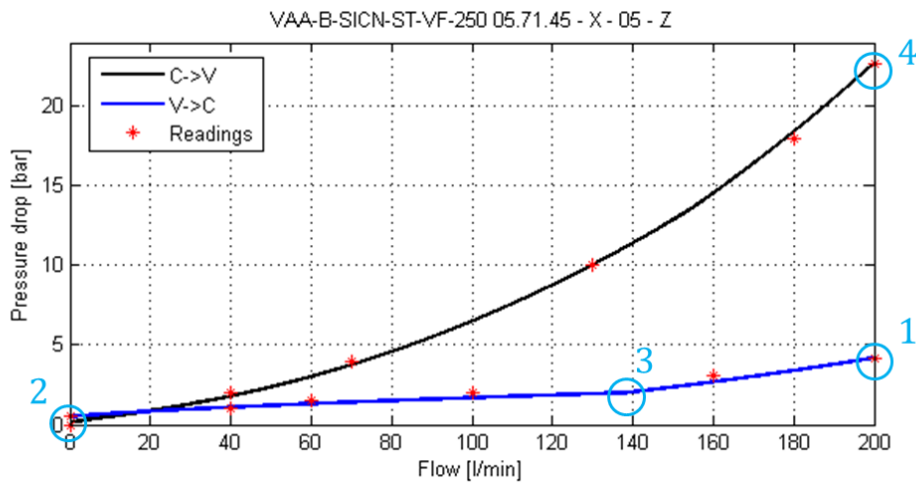


Figure 2.19: Step by step procedure description

The approach led to pressure-flow curves that was comparable with the datasheet curves. The red dots in fig 2.19 corresponds to readings from data sheets and the simulation results are marked with black and blue lines. The parameter optimization approach is performed for the three different sizes used on the bridge crane (VAA-B-SICN-ST-VF-50, -150, and -250). The curves (fig 2.19) show a remarkable similarity with the values read from the data sheet.

CHAPTER 2. SIMULATION MODEL

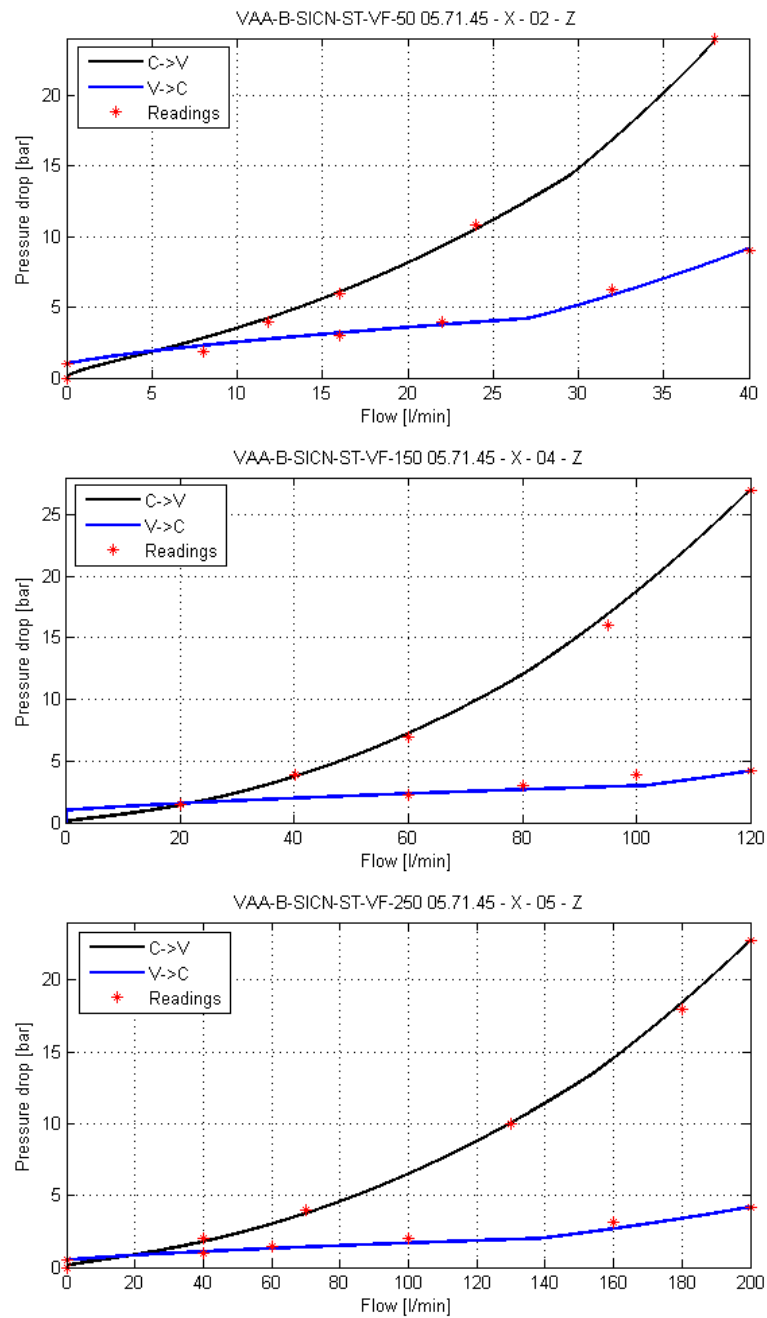


Figure 2.20: Simulation results compared with readings for the mcv [1]

CHAPTER 2. SIMULATION MODEL

As a result of this optimization approach these parameters were found (table 2.8), where $A_{m,prv}$ is the maximum discharge area of the pressure relief valve,

	VAA-B-SICN-ST-VF050	VAA-B-SICN-ST-VF150	VAA-B-SICN-ST-VF250
$A_{m,prv}$	15mm ²	39mm ²	72.1mm ²
p_{cr1}	1bar	1bar	0.5bar
$A_{m,cv1}$	20.5mm ²	90.9mm ²	151.5mm ²
$p_{max,cv1}$	4.2bar	3bar	2bar
p_{cr2}	0.1bar	0.1bar	0.1bar
$A_{m,cv2}$	20.5mm ²	90.9mm ²	151.5mm ²
$p_{max,cv2}$	5bar	1.9bar	2.5bar

Table 2.8: Best parameter results for VAA-B-SICN-ST valves

p_{cr1} , $p_{max,cv1}$ and $A_{m,cv1}$ are the crack pressure, pressure at maximum opening and maximum discharge area for check valve 1. The similar names are used for check valve 2.

The simulation model of this mcv is now fully determined except for the spool response and spring stiffness. These parameters are found by physical testing of the valves. A physical test of the VAA-B-SICN-ST-VF-250 is executed in chapter 3.

	VAA-B-SICN-ST-VF250
k_{p1}	495bar/unit*
k_{p2}	400bar/unit*
ω	12Hz
ζ	1.0

Table 2.9: Results from experimental test in chapter 3

*The spring stiffness is not determined for each spring, but for the sum of both. Since the two parts of the spool always were connected in the performed test, it was impossible to separate them, hence $k_p = k_{p1} + k_{p2} = 895bar/unit$. The spool response is set as a second order transfer function containing the ω and ζ as frequency and damping ratio.

2.4.3 VBSO overcenter valve

Use and functionality

The valve provides control of load by regulating the flow in and out of the actuator through port C1 and C2. This valve module includes two sections, each one composed by a check and a relief valve with balanced piston. The piston has a pilot pressure assisted from the opposite line. The check valves allow free flow into the actuator, and holds against reversed movement. With pilot pressure applied at the line across, the pressure setting of the relief is reduced in proportion to the stated ratio until opening. Relief operates the valve opening independent of back-pressure, but is always subjected to the piloted pressure from V1 or V2. [6]

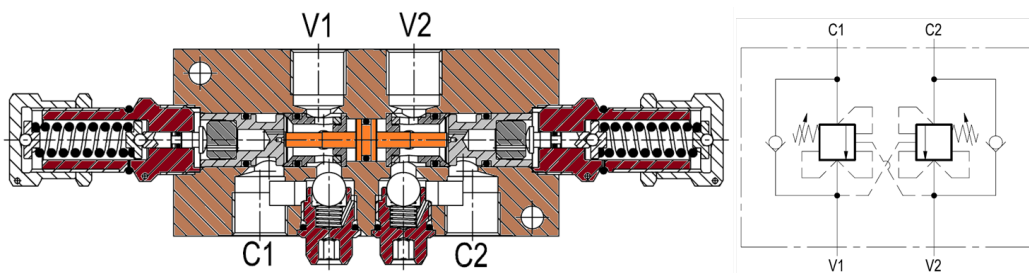


Figure 2.21: VBSO [6]

Determine the pressure relief valve opening

To determine the valve opening, u , the pressure equilibrium was obtained. The pressure equilibrium was determined based on the spool areas and the related pressures.

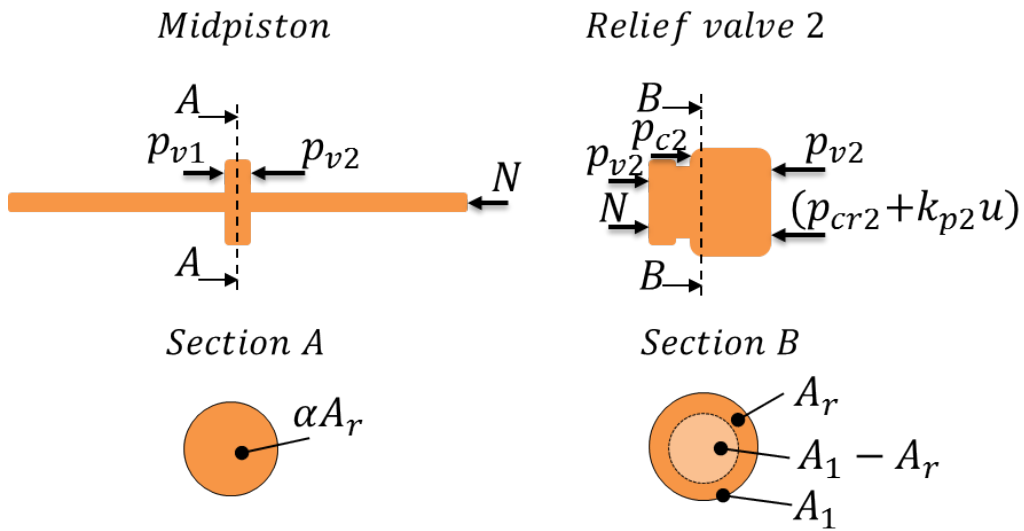


Figure 2.22: Pressures and forces acting on the spool

Since the spool is two folded the force equilibrium of the mid piston is needed to determine whether there is contact between the mid piston and relief valve or not. The contact force N is,

$$\sum F = 0 \rightarrow N_2 = \alpha A_r \cdot (p_{v1} - p_{v2}) \quad (2.16)$$

where α is the pilot ratio and p_{v1} and p_{v2} are the pressures in port V1 and V2 (fig 2.21). Positive N will cause contact between mid piston and relief valve 2 (the one between V2 and C2) and a negative N will cause contact between mid piston and relief valve 1.

Static equilibrium for the pressure relief valve between V2 and C2 (line 2):

While $N < 0$ (no contact)

$$\sum F = p_{v2}(A_1 - A_r) + p_{c2} \cdot A_r - p_{v2}A_1 - (p_{cr2} + k_{p2} \cdot u_2) \cdot A_r \quad (2.17)$$

Divide by the ring area

$$\frac{\sum F}{A_r} = p_{eq} = -p_{v2} + p_{c2} - p_{cr2} - k_{p2} \cdot u_2 \quad (2.18)$$

Static equilibrium, $p_{eq} = 0$, hence

$$u_2 = \frac{-p_{v2} + p_{c2} - p_{cr2}}{k_{p2}} \quad (2.19)$$

where u_2 is the relief valve opening position in line 2 ($0 < u_2 < 1$), p_{cr2} is the crack pressure setting for line 2, and k_{p2} is the spring stiffness for the spring acting on the relief valve 2.

While $N > 0$ (contact)

$$\begin{aligned} \sum F &= \alpha A_r (p_{v1} - p_{v2}) + p_{v2}(A_1 - A_r) + p_{c2}A_r - p_{v2}A_1 - A_r(p_{cr2} + k_{p2}u_2) \\ \sum p &= p_{eq} = \frac{\sum F}{A_r} \\ p_{eq} &= \alpha(p_{v1} - p_{v2}) - p_{v2} + p_{c2} - (p_{cr2} + k_{p2}u_2) \end{aligned} \quad (2.20)$$

Static equilibrium, $p_{eq} = 0$, hence

$$p_{eq} = 0 \rightarrow u_2 = \frac{\alpha p_{v1} - p_{v2}(\alpha + 1) - p_{cr2} + p_{c2}}{k_{p2}} \quad (2.21)$$

CHAPTER 2. SIMULATION MODEL

Same static analysis was done for the pressure relief valve in line 1 (between V1 and C1):

While $N > 0$ (no contact)

$$u_1 = \frac{-p_{v1} + p_{c1} - p_{cr1}}{k_{p1}} \quad (2.22)$$

While $N < 0$ (contact)

$$u_1 = \frac{\alpha p_{v2} - p_{v1}(\alpha + 1) - p_{cr1} + p_{c1}}{k_{p1}} \quad (2.23)$$

Simulink model

The VBSO valve has two relief valves and two check valves (fig 2.23). The simulink model is structured the same way with one check valve in parallel with each relief valve. The relief valves are simulated as orifices with variable discharge areas. The areas (a_1 and a_2) are determined through the spool position, u , and the maximum discharge area, $A_{d,max}$. The discharge areas are assumed to increase linearly with the sled position. Hence,

$$a_1 = A_{d,max} \cdot u_1 \tag{2.24}$$

$$a_2 = A_{d,max} \cdot u_2 \tag{2.25}$$

where u_1 and u_2 are given by equation 2.21 and 2.19.

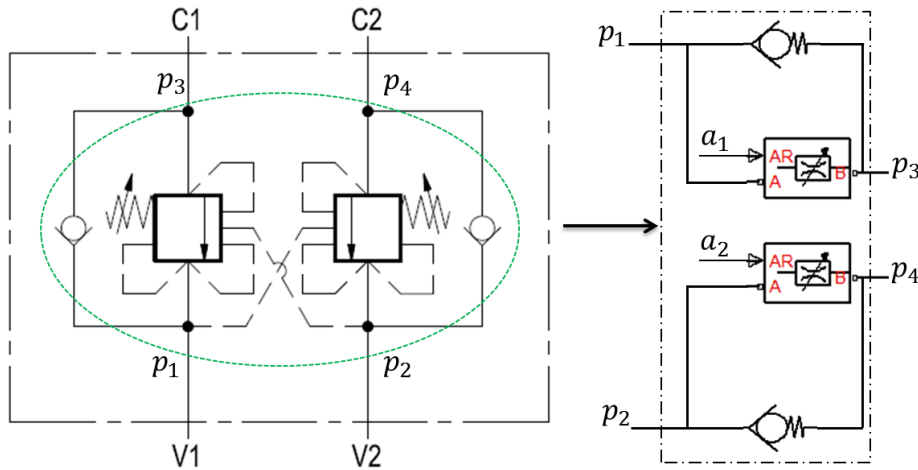


Figure 2.23: Flow chart and simulink structure

The discharge area is calculated through the equation 2.21 and 2.19. These functions are calculated through this block diagram in simulink in fig 2.24. It is also added a response block to represent the spool response.

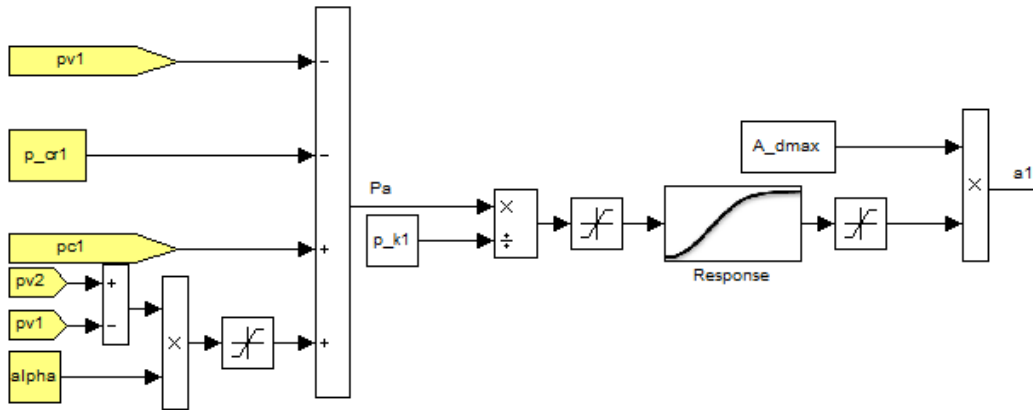


Figure 2.24: Simulink block diagram of the calculation of the discharge area, a_1

Tuning discharge areas

Maximum discharge areas for these valve were found by the same procedure as in section 2.4.2. A pressure drop over the pressure relief valve was ramped from 0 to 26bar, while the valve was fully opened. At 26bar the flow across the relief valve should be 140l/min (app. H). The area was determined by setting the area to fit the final value at $Q = 140l/min$ and $\Delta p = 26bar$. On the directional valve the pressure drop was ramped from 0 to 7bar. At 7bar pressure drop the flow should be 140l/min. The check valve tuning was found in three steps. Firstly the 7bar at 140l/min determined the discharge area when the check valve is fully open. Secondly the crack pressure was set to 0.5bar according to the data sheet (app. H), which determined the starting offset at $Q = 0$. The third setting was the pressure needed to fully open the check valve. The results were plotted and compared to the values obtained from the data specification sheet (marked with red dots in fig 2.25).

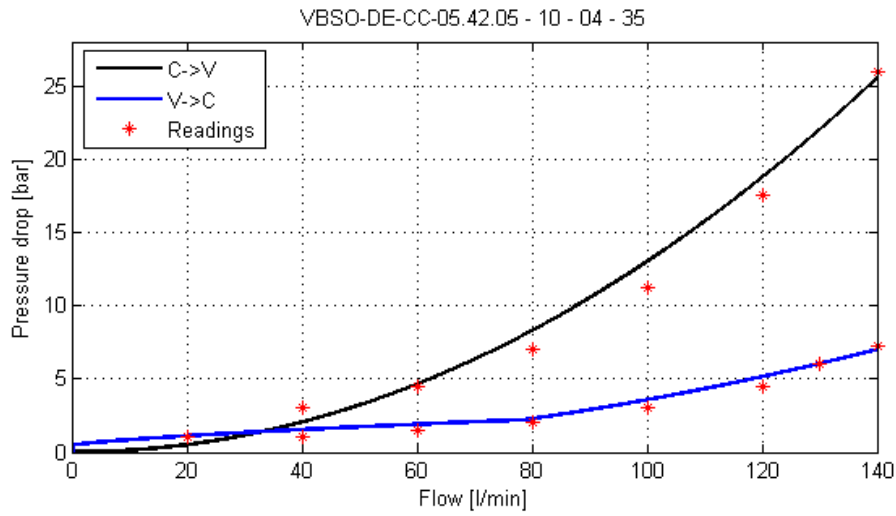


Figure 2.25: Simulated overcenter valve response, compared with readings from datasheet [H]

The curves gave a satisfying match with the obtained parameters (table 2.25).

	Description	VBSO-DE-CC-05.42.05-10-04 -35
$A_{m,prv}$	Max area, relief valve	$43mm^2$
$p_{cr,cv}$	Crack pr., check valve	$0.5bar$
$A_{m,cv}$	Max area, check valve	$82mm^2$
$p_{max,cv}$	Max opening pr., check valve	$2.2bar$

Table 2.10: Best parameter results for the VBSO-DE-CC valve

The remaining parameters to be considered are the frequency and damping ratio in the response block (fig 2.24), and the spring stiffness of the spring acting on the spool. These parameters are set to some temporary values to be able to use the model (table 2.11). To get a more accurate model these parameters should be determined through some experimental testing of the valve.

Response frequency	ω	$30Hz$
Response damping ratio	ζ	1
Spring stiffness*	k_p	$900bar/unit$

Table 2.11: Temporary variables.

Where *bar* is the force divided by the ring area, A_r , and one unit represent the spool movement from 0 to 1.

2.5 Hydraulic motors

The hydraulic motors are simulated with both leakage flow and friction (mechanical efficiency). The hydraulic motors used on the bridge crane and lower guiding arm are produced by Parker Hannifin and are of the F12 and F11 series (table 2.13). The volumetric efficiency is caused by leakage flow inside the motor and is simulated as a small orifice with the area, A_{lm} (fig 2.27). This makes the motor leakage dependent of the inlet- and back- pressure. The model also contains two drain orifices, A_{ld} . These orifices are very small and their mission is to prevent static pressure in the system.

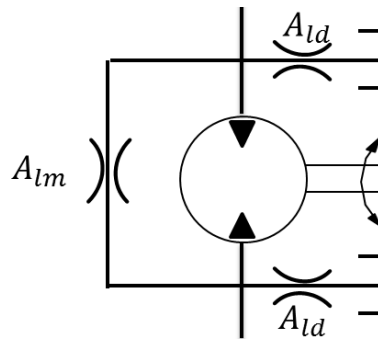


Figure 2.26: Simulated motor, flowchart

It is assumed that the volumetric efficiency for these is more or less the same[7]. The volumetric efficiency show a low efficiency at low velocities and a efficiency about 95% at high velocities (fig 2.27).

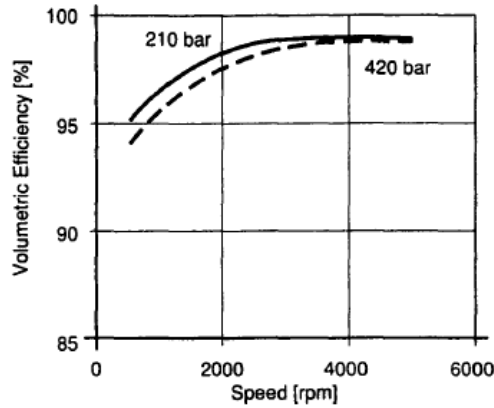


Figure 2.27: Volumetric efficiency, F12 motor/pump[7]

To tune in the leakage orifices, a small test was executed for each motor displacement (19, 30, 60). In this test the pressure drop over the motor was set to 210bar due to fig 2.27, and then curve fitted with readings from fig 2.27. To perform a curve fitting the expression for the volumetric efficiency was needed. This was found by measuring the inlet flow and output shaft velocity. The inlet flow was used to calculate the theoretical velocity, and a velocity sensor on the output shaft gave the angular velocity. The volumetric efficiency was then calculated through this formula,

$$\eta_{vM} = \frac{Q_{tM}}{Q_M} = \frac{\omega \cdot D_M}{Q_M \cdot 2\pi} \quad (2.26)$$

where ω is the output velocity, D_M is the motor displacement, Q_M is the inlet flow, and Q_{tM} is the theoretical flow demand.

- η_{vM} : Volumetric efficiency
- Q_{tM} : Theoretical flow demand of the motor, [m^3/s]
- Q_M : Actual flow demand of the motor, [m^3/s]
- D_M : Stroke displacement, [m^3/rev]

Table 2.12: Variables in eq 2.26

The curve fitting gave the following results (fig 2.28).

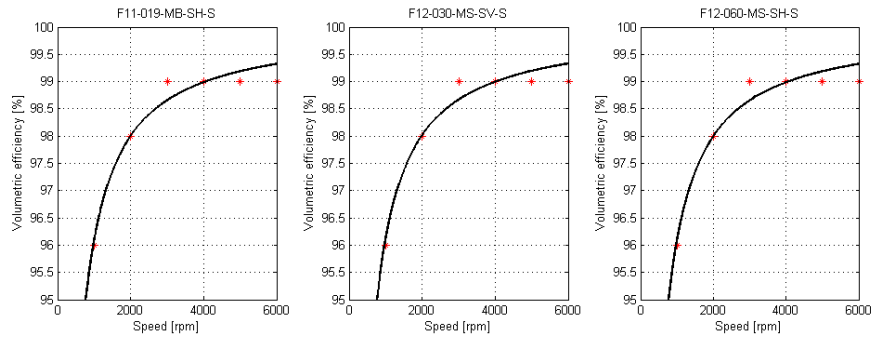


Figure 2.28: Comparing simulated volumetric efficiency with readouts.

Given that the readings is quite rough and that the efficiency graph (from datasheet) is given with an accuracy of $\pm 2\%$ [7], it is assumed that the result is more than accurate enough for this simulation model of the motor. The mechanical efficiency (friction) is implemented as a moment subjected to the outputshaft, this is explained in section 2.6. The obtained orifice values are shown in table 2.13.

Place	Type	Leakage area, A_{lm}	Leakage area, A_{ld}
Bridge travel, BC	F12-030-MS-SV-S VOAC SAE B	$0.13mm^2$	$0.0001mm^2$
Trolley travel, BC	F12-030-MS-SV-S VOAC SAE B	$0.13mm^2$	$0.0001mm^2$
Slewing, BC	F12-060-MS-SH-S VOAC SAE C	$0.263mm^2$	$0.0001mm^2$
Trolley LGA	F11-019-MB-SH-S VOAC SAE B	$0.083mm^2$	$0.0001mm^2$
Slewing LGA	F12-030-MS-SV-S VOAC SAE B	$0.13mm^2$	$0.0001mm^2$

Table 2.13: Discharge areas, volumetric efficiency

The drain orifices were set to a almost negligible area of $10^{-4}mm^2$. The leakage orifice to tank is nonetheless included because it prevents static pressure in the system.

2.6 Effective friction

The applied friction force is added as a moment to the output shaft on the motors. This moment is calculated in a function block and depends on pressure loss over the motor, rotational velocity on output shaft, and motor displacement. The motor friction is simulated with the coulomb plus viscous friction model (fig 2.29), and is dependent on the output moment.

$$F_M = (1 - \nu_{hm}) \cdot M_o = (1 - \nu_{hm}) \cdot \frac{\Delta p \cdot D_M}{2\pi} \quad (2.27)$$

where F_M is the motor friction, ν_{hm} is the hydromechanical efficiency, M_o is the output shaft moment, D_M is motor displacement, and Δp is the pressure loss through the motor. The hydromechanical efficiency is set to 0.9. Since there is no experimental data of the model the additional friction moment/force is set to be 10% of the created moment/force. This 10% could represent among other things, sliding friction, rack pinion friction and so on. How the friction moment model

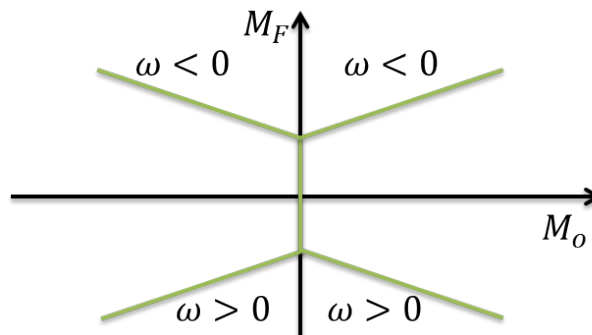


Figure 2.29: Coulomb + viscous friction model

(eq 2.27 and fig 2.29) acts dependent on velocity and moment is shown in fig 2.30.

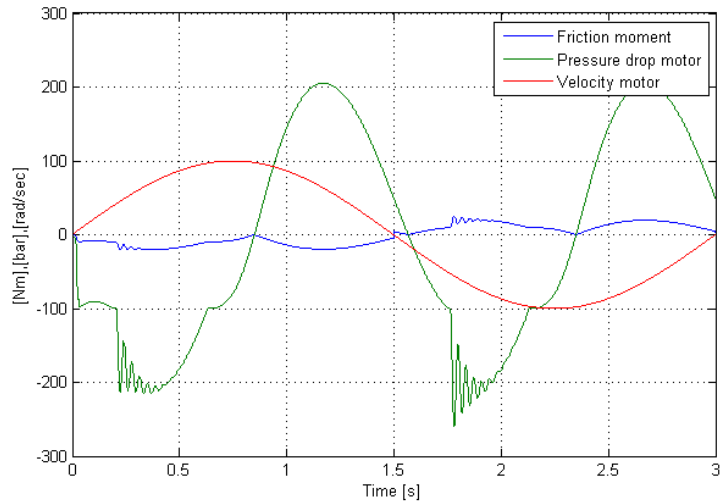


Figure 2.30: Plot verifies the direction of the friction moment

It may be that the actual friction also depends on the velocity, have hysteresis and stiction forces, but because friction is complex and experimental data is vital to get a good friction model it is chosen to use simple friction models. To examine how an increased friction will affect the design parameters of the model, it is in Chapter 4 looked at how an increased viscous friction dependent velocity (fig 2.31) will affect the system.

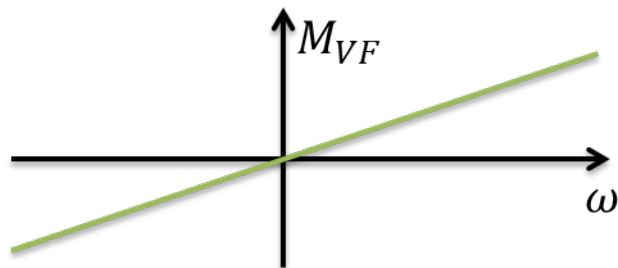


Figure 2.31: Viscous friction dependent on velocity

2.7 Effective mass moment of inertia, BC

The inertia is coupled directly to the motor output shaft. Because of this the effective mass moment of inertia (MMI) was calculated dependent on the masses acting and the shaft and gearing ratios. The mass moment of inertia for the gears and rotational shafts is considered negligible compared to the main parts, bridge, trolley, and guide mast. To keep a low complexity and a fast running simulation model the MMI was calculated dependent on the rotational motor shaft.

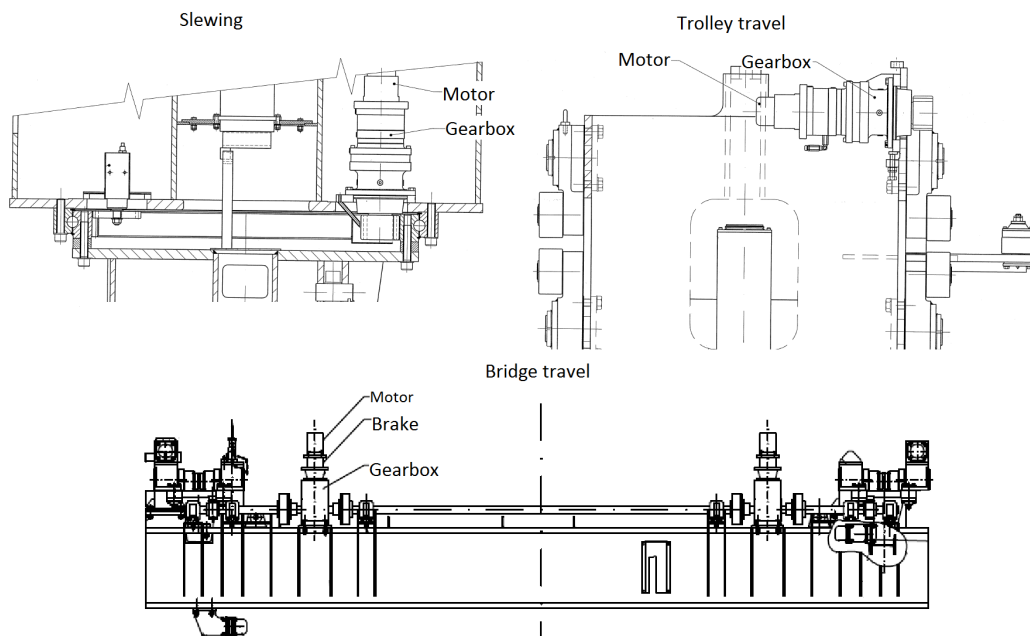


Figure 2.32: Power transfer

To obtain the right gearing ratio it was important to determine how each part moved. As seen in fig 2.32, the trolley travel and bridge travel has a rack and pinion system, which make the gearing dependent on the pinion gear. On the slewing system the pinion on the motor shaft is coupled to a ring gear. Hence the gearing is dependent on both pinion radius and ring gear radius. In addition to this all of the motors have a gearbox.

The MMI for bridge and trolley travel was calculated with the formula,

$$J_m = \frac{(m + m_L) \cdot r^2}{n_g^2} \quad (2.28)$$

where J_m is the MMI for the translational mass ($m+m_L$), m_L is the load mass (the pipe), r is the pinion radius, and n_g is the gearbox ratio. Because of the complex geometry of the guide mast, it was assumed that the guide mast was a cylindrical part with radius of $0.8m$ and the additional load inertia was added as a point mass, with a distance $r_{tp} = 2100mm$ from the slewing axis. This gave,

$$J_m = \frac{1 \cdot mr_S^2}{2 \cdot n_G^2} + \frac{m_L \cdot r_{tp}^2}{n_G^2} \quad (2.29)$$

where m is guide mast mass, r_S is the assumed radius, and n_G is the gearing ratio between the rotating guide mast and motor shaft. Hence the n_G is dependent on both gearbox ratio, and pinion and ring gear radius.

Motor	Gearing ratio, n_G	Mass, m [kg]	Radius, r [m]	MMI, J [kgm^2]
Bridge travel	39.0	22997	$r_{p,BT} = 75e - 3$	$J_{m,BT} = 0.085 + \frac{m_L \cdot r_{p,BT}^2}{n_g^2}$
Trolley travel	38.4	13006	$r_{p,TT} = 55e - 3$	$J_{m,TT} = 0.027 + \frac{m_L \cdot r_{p,TT}^2}{n_g^2}$
Slewing	$44.6 \cdot \frac{1200}{132}$	5741	$r_S = 0.8$	$J_{m,S} = 0.011 + \frac{m_L \cdot r_{tp}^2}{n_G^2}$

Table 2.14: MMI caused by moving mass presented on motor shaft. Masses and geometry values were obtained in component drawings

The motor inertias was also added, and data was obtained from the motor specification sheets (app. I). Motor inertia for bridge travel (BT), trolley travel (TT) and slewing (S) were:

$$J_{m,mBT} = 0.0034kgm^2 \quad J_{m,mTT} = 0.0017kgm^2 \quad J_{m,mS} = 0.005kgm^2$$

CHAPTER 2. SIMULATION MODEL

The inertias inserted in the model was the sum of these inertias,

$$J_{BT} = J_{m,mBT} + J_{m,BT} \quad J_{TT} = J_{m,mTT} + J_{m,TT} \quad J_S = J_{m,mS} + J_{m,S}$$

where J_{BT} , J_{TT} , J_S is the total MMI for BT, TT, and S.

Note that these are rough estimates of the inertias and that more accurate measurement could be found by using 3D cad models. However these estimates are believed to be accurate enough for this model.

2.8 Effective mass and mass moment of inertia, LGA

The LGA model consists of four actuators. Two cylinders and two motors. The cylinders perform the telescope extension and the jib tilt, and the motors perform trolley travel and slewing (fig 2.33). Since the system is modeled as a one dimensional system, there is a need for effective inertias and masses to replace the multibody dynamics. Most of these masses and inertias are dependent of the position and the velocity LGA. For example one can easily see that the slewing (rotating the LGA) inertia is dependent on the extension of the telescope. The key parameters to obtain the effective masses and inertias with are θ , J_A , and J_S . The θ is the telescope angle, J_A is the MMI around joint A and J_S is the effective slewing inertia (fig 2.34).

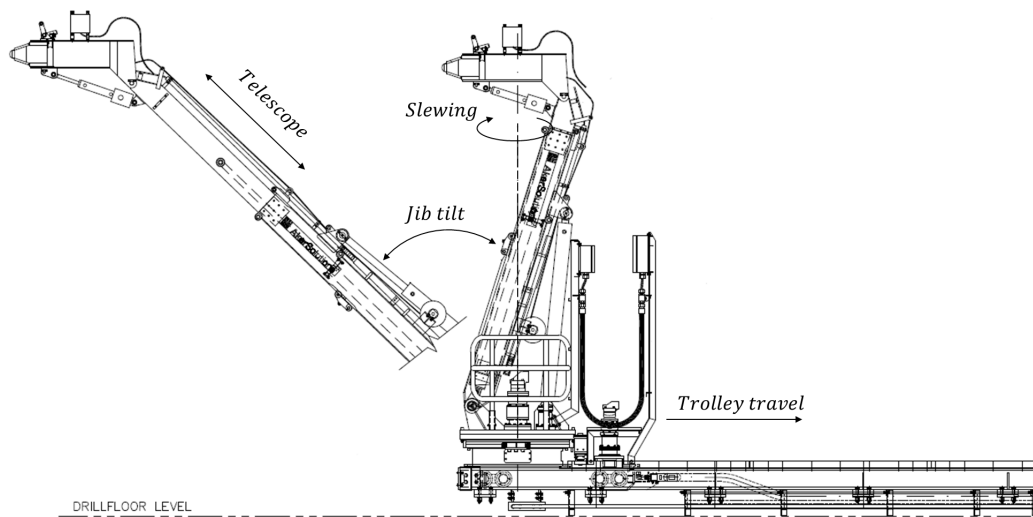


Figure 2.33: Drawing of the LGA showing the functionalities implemented in the simulation model.

2.8.1 Geometry LGA

The geometry of the LGA is important to determine the local inertias and the kinematics, which will give the inertias J_A , J_S and the relationship between the cylinder extension and θ_1 .

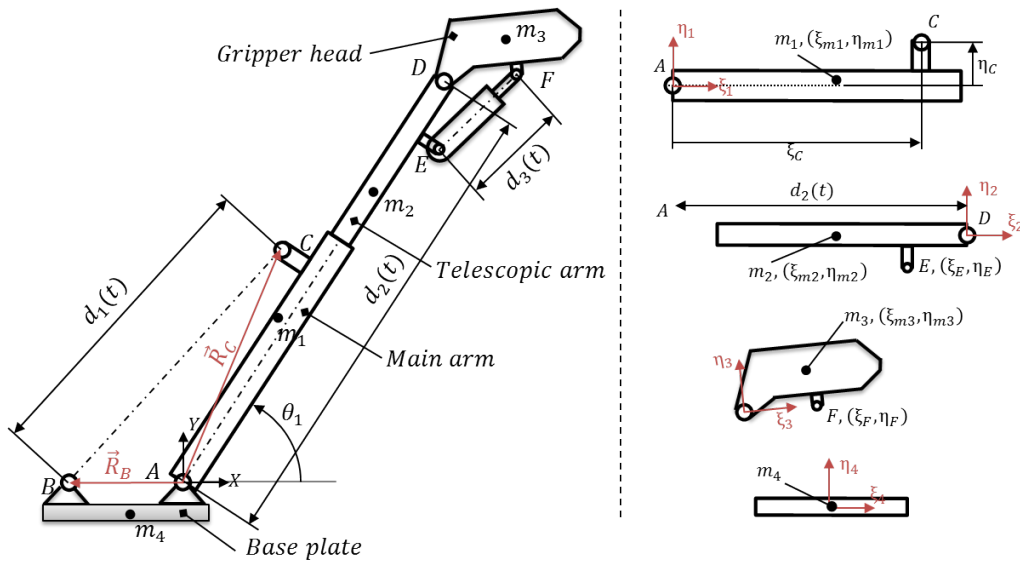


Figure 2.34: Geometry and location of center of mass. Global Z-axis and local ζ -axis works perpendicular to the paper plane pointing outwards

- $m_i, (\xi_i, \eta_i)$: Mass and local mass center coordinates(referred to as r_{mi}).
- R_{mi} : Global coordinates to mass center, part i .
- r_{mi} : Local coordinates to mass center, part i , referred to fig 2.34
- A_i : Transformation matrix from local to global vectors, part i ,
- θ_i : Angle between the global and the local coordinate system, i .

From the figure above one can see that the angle θ_1 depends on the cylinder extraction d_1 . Extracting the telescope will affect the inertia and mass center, and so on.

2.8.2 Obtain $\theta_1(d_1)$

To calculate the different inertias and effective masses, it is necessary to know the position of the LGA. This include the telescope angle, θ_1 , that is a function of the cylinder extension d_1 (fig 2.34) This relationship is given by the kinematics of the model. The basic equations are related to the ABC triangle (fig 2.34).

Local vector to joint C, and global vector to joint B:

$$\vec{r}_c = \begin{bmatrix} 2191 \\ 340 \end{bmatrix} \quad \vec{R}_B = \begin{bmatrix} -775 \\ 0 \end{bmatrix}$$

Transformation matrices (transforms from local to global coordinates):

$$A_i = \begin{bmatrix} \cos \theta_i & -\sin \theta_i \\ \sin \theta_i & \cos \theta_i \end{bmatrix} \quad B_i = \frac{\delta A_i}{\delta \theta_i} \begin{bmatrix} -\sin \theta_i & -\cos \theta_i \\ \cos \theta_i & -\sin \theta_i \end{bmatrix}$$

The relationship between distance, d_1 , and angle θ_1 according to Pythagoras:

$$0 = d_1^2 - \left(A_1 \begin{bmatrix} 2191 \\ 340 \end{bmatrix} - \begin{bmatrix} -775 \\ 0 \end{bmatrix} \right)^T \left(A_1 \begin{bmatrix} 2191 \\ 340 \end{bmatrix} - \begin{bmatrix} -775 \\ 0 \end{bmatrix} \right) \quad (2.30)$$

$$d_1 = \sqrt{(2191 \cos \theta_1 - 340 \sin \theta_1 + 775)^2 + (2191 \sin \theta_1 + 340 \cos \theta_1)^2} \quad (2.31)$$

The velocity relationship was found by time differentiation of eq 2.30.

$$0 = 2 \cdot d_1 \cdot \dot{d}_1 - 2 \cdot \left(A_1 \begin{bmatrix} 2191 \\ 340 \end{bmatrix} - \begin{bmatrix} -775 \\ 0 \end{bmatrix} \right)^T \left(\dot{\theta}_1 \cdot B_1 \begin{bmatrix} 2191 \\ 340 \end{bmatrix} \right) \quad (2.32)$$

$$\begin{aligned} C1 & -263500mm^2 \\ C2 & -1698025mm^2 \end{aligned}$$

Then solved for \dot{d}_1 and simplified.

$$\begin{aligned} \dot{d}_1 &= \frac{\dot{\theta}_1}{d_1} ((2191 \cos \theta_1 - 340 \sin \theta_1 + 775) \cdot (-2191 \sin \theta_1 - 340 \cos \theta_1) + \\ & \quad (2191 \sin \theta_1 + 340 \cos \theta_1) \cdot (2191 \cos \theta_1 - 340 \sin \theta_1)) \\ \rightarrow \dot{d}_1 &= \frac{\dot{\theta}_1}{d_1} (-263500 \cos \theta_1 - 1698025 \sin \theta_1) \end{aligned} \quad (2.33)$$

Where $\dot{\theta}_1$ is the angular velocity (s^{-1}) of the main arm and \dot{d}_1 is the translational velocity of cylinder 1 in mm/s . The equations 2.31 and 2.33 show the connection between position and velocity of the cylinder and the rotation and angular velocity of the telescopic arm.

From equation 2.31 and 2.33 these expressions are solved for θ_1 and $\dot{\theta}_1$:

$$\theta_1 = f_1(d_1) \quad (2.34)$$

Function $f_1(d_1)$ is a very large expression and is shown in appendix D.

$$\dot{\theta}_1 = \frac{\dot{d}_1 \cdot d_1}{(-263500 \cos \theta_1 - 1698025 \sin \theta_1)} \quad (2.35)$$

The expressions for θ_1 in eq 2.34 and 2.35 is now possible to implement in the simulation model, and are used to calculate the inertias J_A and J_S .

2.8.3 Local mass moment of inertia

To calculate the total MMI for jib tilt (parallel to the Z axis) and slewing (parallel to the Y axis) it was necessary to calculate the MMI for each part. These local inertias is together with the parallel-axis theorem used to obtain the jib tilt MMI, J_A and slewing MMI, J_S . The local MMI was calculated for the four moving parts (fig 2.35). The parts are simplified to be able to do some simple hand calculations. It is assumed that these rough hand calculations will be more than accurate enough for this simulation model, if necessary one could obtain the exact inertias with use of data from cad-models.

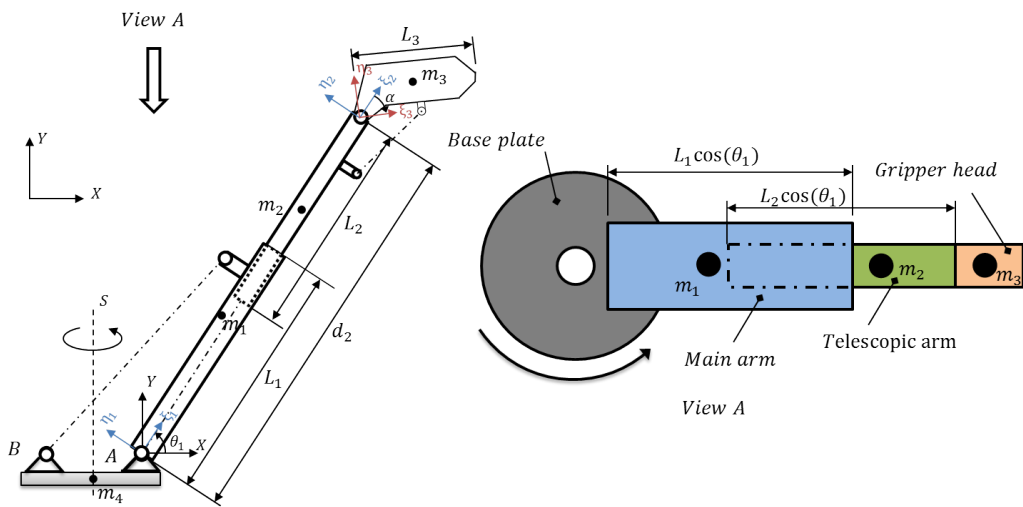


Figure 2.35: Mass centers

Part 1, Main arm

The main arm is modeled as a beam with a square cross-section, with height, S_1 and length, L_1 .

$$m_1 = 401.3kg \quad \vec{r}_{m1} = [1.5m \quad 0.05m \quad 0m]$$

$$S_1 = 0.300m \quad L_1 = 3.0m$$

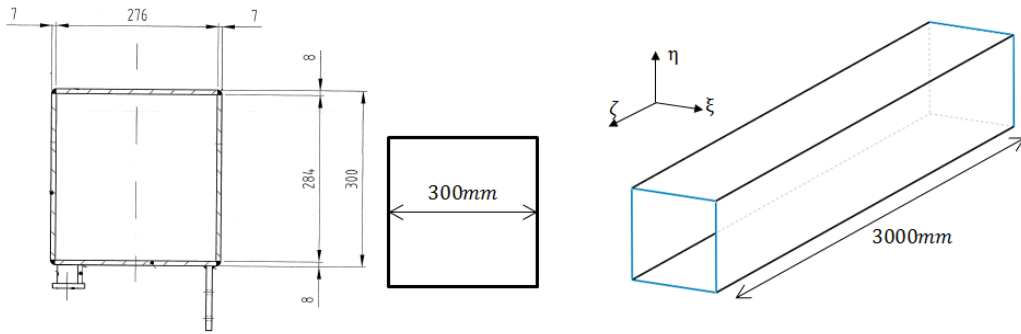


Figure 2.36: Simplified cross section

The local MMI around the mass center,

$$J_{1,\xi} = \frac{7}{24}m_1S_1^2 + \frac{m_1L_1}{12} \quad (2.36)$$

$$J_{1,\eta} = \frac{7}{24}m_1S_1^2 + \frac{m_1L_1}{12} \quad (2.37)$$

$$J_{1,\zeta} = \frac{m_1S_1^2}{3} \quad (2.38)$$

where $J_{1,\xi}$, $J_{1,\eta}$ and $J_{1,\zeta}$ are the local MMI around the mass center.

Part 2, Telescopic arm

The telescopic arm is also modeled as if it was cylindrical:

$$\begin{aligned} m_2 &= 265.2kg & \vec{r}_{m_2} &= [1565m \quad 0.075m \quad 0m] \\ S_2 &= 0.250m & L_2 &= 3.13m \end{aligned}$$

Where R_2 is the cylinder radius, L_2 is the length, and \vec{r}_{m_2} is the mass center location with local coordinates.

$$J_{2,\xi} = \frac{7}{24}m_2S_2^2 + \frac{m_2L_2}{12} \quad (2.39)$$

$$J_{2,\eta} = \frac{7}{24}m_2S_2^2 + \frac{m_2L_2}{12} \quad (2.40)$$

$$J_{2,\zeta} = \frac{m_2S_2^2}{3} \quad (2.41)$$

where $J_{2,\xi}$, $J_{2,\eta}$ and $J_{2,\zeta}$ are the local MMI around the mass center.

Part 3, Gripper head

The gripper head was modeled as a solid box (fig 2.37). The gripper head was also assumed to always be horizontally ($\theta_3 = 0$).

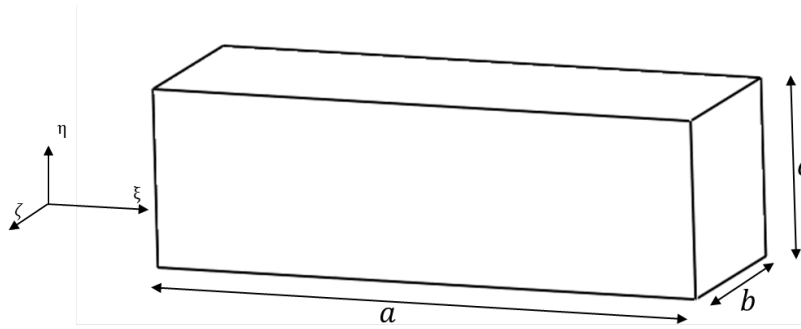


Figure 2.37: Box

$$a = 1.26m \quad b = 0.40m \quad c = 0.43m \quad m_3 = 175.2kg$$

$$J_{3,\zeta} = \frac{m_3(a^2 + c^2)}{12} \quad (2.42)$$

$$J_{3,\eta} = \frac{m_3(a^2 + b^2)}{12} \quad (2.43)$$

Part 4, Baseplate

When slewing, the baseplate is also rotating. The baseplate is assumed to be a disk with an inner and outer diameter, yielding:

$$J_{4,Y} = J_{4,S} = \frac{m_4(R^2 + r^2)}{2} \quad R = 1.2m \quad r = 0.6m \quad m_4 = 362kg$$

where R is the outer diameter, r is the inner diameter, and m_4 is the baseplate weight.

The local inertias are now established for the LGA with four parts. Inertias from cylinders and pistons are neglected.

2.8.4 Slewing MMI

To obtain the effective MMI for slewing the system is looked at as a two dimensional system (fig 2.38). The two interesting MMIs are the ones around the local ξ and η axis, because these will affect the global MMI parallel to the Y axis.

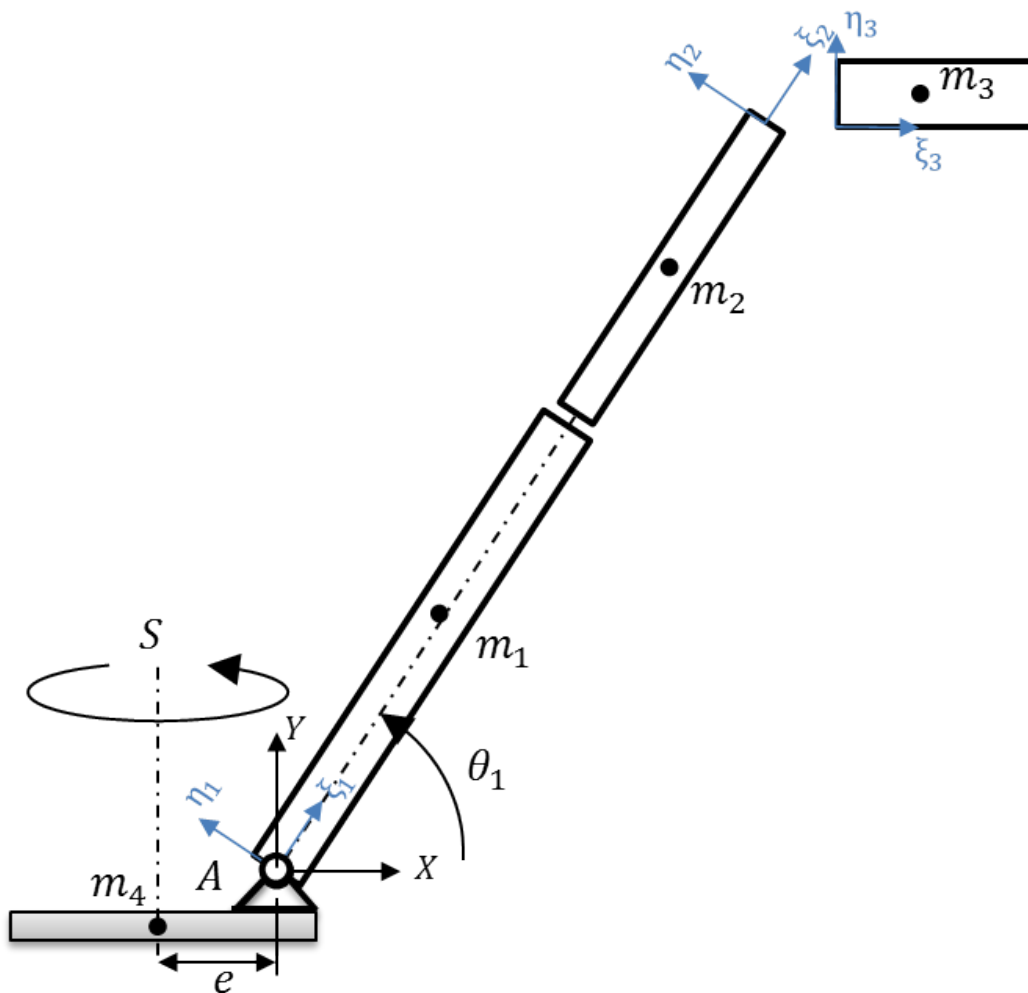


Figure 2.38: The four parts of the LGA.

Trough Nikravesh equation for 2-dimensional dynamics, the local MMIs are converted to global inertias.

$$J_i = A_i J'_i A_i^T \quad A_i = \begin{bmatrix} \cos \theta_i & -\sin \theta_i \\ \sin \theta_i & \cos \theta_i \end{bmatrix} \quad J'_i = \begin{bmatrix} J_{i,\xi} & 0 \\ 0 & J_{i,\eta} \end{bmatrix} \quad (2.44)$$

$$J = \begin{bmatrix} J_{i,X} \\ J_{i,Y} \end{bmatrix} \quad (2.45)$$

$$\rightarrow J_{i,Y} = J_\xi \sin \theta_1^2 + J_\eta \cos \theta_1^2 \quad (2.46)$$

Where $J_{i,Y}$ is the local MMI around an axis parallel to the global Y-axis. Using eq. 2.46 and the parallel-axis theorem give,

$$J_{1,S} = m_1 \left(e + \frac{L_1}{2} \cos \theta_1 \right)^2 + J_{1,\xi} \sin \theta_1^2 + J_{1,\eta} \cos \theta_1^2 \quad (2.47)$$

$$J_{2,S} = m_2 \left(e + \left(d_2 - \frac{L_2}{2} \right) \cos \theta_1 \right)^2 + J_{2,\xi} \sin \theta_1^2 + J_{2,\eta} \cos \theta_1^2 \quad (2.48)$$

$$J_{3,S} = m_3 \left(e + \frac{L_3}{2} + (d_2) \cos \theta_1 \right)^2 + J_{3,\eta} \cos \theta_1^2 \quad (2.49)$$

$$J_{4,S} = J_{4,Y} \quad (2.50)$$

where e is the distance from joint A to the slewing axis (fig 2.38), d_2 is the telescope extension (fig 2.35), and $J_{i,S}$ is the local MMI around mass center of part i (section 2.8.3).

The MMI for slewing around the slewing axis (s-axis in fig 2.38):

$$J_S = J_{1,S} + J_{2,S} + J_{3,S} + J_{4,S} \quad (2.51)$$

Where the J_S depends on the rotated parts (part 1, 2, 3, 4 see fig 2.38). To obtain the effective MMI subjected to the motor shaft, the gearing between the slewing axis and the motor shaft need to be considered (fig 2.39).

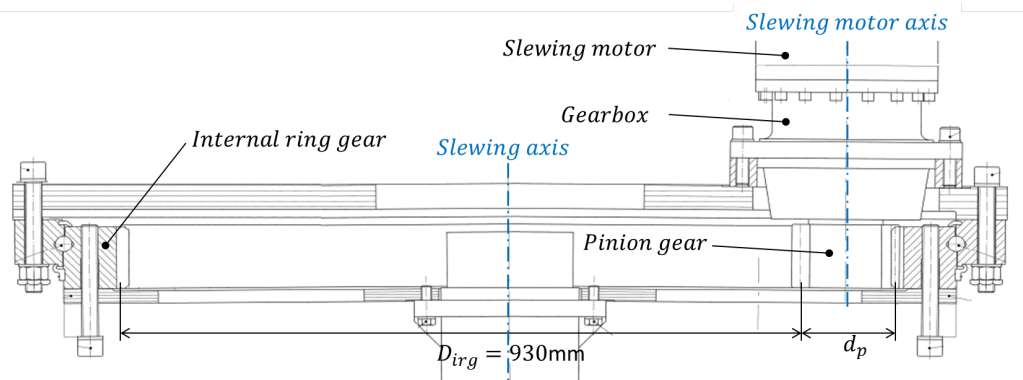


Figure 2.39: Interaction between the slewing axis and the motor shaft

This geometry (fig 2.39) give,

$$n_{tot} = \frac{n_g \cdot D_{irg}}{d_p} \quad (2.52)$$

where n_{tot} is the gearing ratio between motor axis and slewing axis, n_g is the gearbox ratio, D_{irg} is the pitch diameter of the internal ring gear, and d_p is the pitch diameter of the pinion gear connected to the motor. This give an effective MMI for slewing acting on the motor shaft,

$$J_{sm} = \frac{J_S}{n_{tot}^2} + J_m + J_g \quad (2.53)$$

Where J_m is the MMI for the motor, J_g is the MMI for the gearbox, and n_{tot} and J_S correspond to the variables in equation 2.52 and 2.51.

2.8.5 Trolley travel MMI

The effective MMI for the trolley travel is given by the trolley mass and the gearing ratio. The gearing ratio is given by the gearbox ratio and the pitch diameter of the pinion gear (fig 2.40).

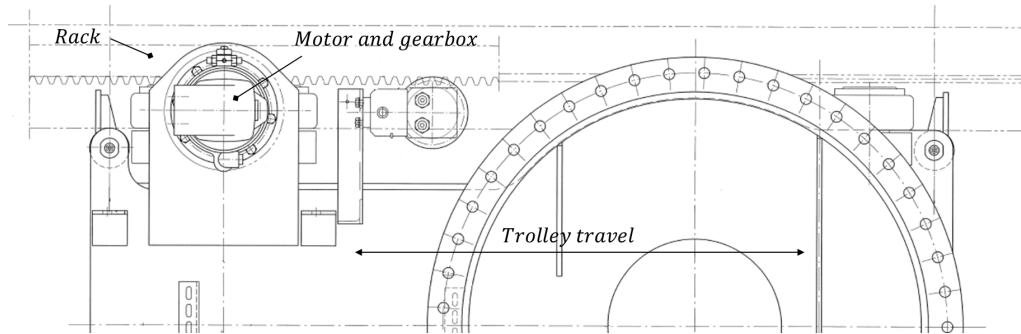


Figure 2.40: Interaction between motor and trolley travel.

$$m_{tt} = 1500kg \quad r_p = 110mm \quad n_g = 39.1$$

$$J_{tt} = m_{tt} \frac{r_p^2}{n_g} + J_m + J_g \quad (2.54)$$

where J_{tt} is the effective MMI, m_{tt} is the mass of the trolley included the mass of the LGA, r_p is the pitch radius, n_g is the gearing ratio of the gearbox, J_m is the MMI for the motor, and J_g is the MMI for the gearbox,.

2.8.6 Effective mass

The effective mass of cylinder one is calculated from a kinematic energy consideration (eq 2.60). The formula is dependent on the angular velocity, translational velocity of the piston, and the MMI around joint A (joint A has a rotational degree of freedom around Z-axis, in fig 2.35). The MMI was obtained dependent on the gravitational center and local MMI for each part.

To calculate the MMI around the center of mass the center of mass coordinates are necessary. Center of mass (global coordinates):

$$\begin{bmatrix} X_G \\ Y_G \end{bmatrix} = \frac{A_1 \vec{r}_{m1} m_1 + (\vec{R}_{cs2} + A_2 \vec{r}_{m2}) \cdot m_2 + (\vec{R}_{cs3} + A_3 \vec{r}_{m3}) \cdot m_3}{m_1 + m_2 + m_3} \quad (2.55)$$

$$\vec{R}_G = \begin{bmatrix} X_G \\ Y_G \end{bmatrix} \quad (2.56)$$

The \vec{R}_{csi} is the global coordinates for the local coordinate systems corresponding to part i , and are respectively:

$$\vec{R}_{cs1} = \begin{bmatrix} 0 \\ 0 \end{bmatrix} \quad \vec{R}_{cs2} = A_1 \begin{bmatrix} d_2 \\ -50 \end{bmatrix}^T \quad \vec{R}_{cs3} = \vec{R}_{c2}$$

The parallel-axis theorem was used to calculate the MMI parallel to the Z-axis in the gravitational mass center of the guiding arm.

$$\begin{aligned} J_{GZ} = & J_{1,\zeta} + m_1 \cdot |\vec{R}_G - A_1 \cdot \vec{r}_{m1}|^2 + \\ & J_{2,\zeta} + m_2 \cdot |\vec{R}_G - (\vec{R}_{cs2} + A_2 \cdot \vec{r}_{m2})|^2 + \\ & J_{3,\zeta} + m_3 \cdot |\vec{R}_G - (\vec{R}_{cs3} + A_3 \cdot \vec{r}_{m3})|^2 \quad (2.57) \end{aligned}$$

where $J_{i,\zeta}$ is the local MMI around the mass center for part i (see eq 2.38, 2.41, and 2.42), m_i is the mass of part i , A_i is the transformation matrix for part i , r_{mi} is the local vector from the local coordinate system to the local mass center in part i (fig 2.34), R_G is the global center of gravity vector, and R_{csi} is the global position of the local coordinate systems.

By using parallel-axis theorem the jib tilt inertia around point A (J_A) is derived

$$J_A = J_G + m_G \cdot r_G^2 = J_G + m_G(X_G^2 + Y_G^2) \quad (2.58)$$

Through the equations to calculate θ_1 and $\dot{\theta}_1$ and J_A (eq: 2.31,2.33, 2.58) the effective mass is calculated. The effective mass was calculated due to the equilibrium between rotational and translational kinetic energy.

$$E_{kin} = \frac{1}{2}m\dot{x}^2 = \frac{1}{2}J\dot{\theta}^2 \quad (2.59)$$

$$m = J \frac{\dot{\theta}^2}{\dot{x}^2} \quad (2.60)$$

Equation 2.60 give a this formula for the effective mass acting on cylinder 1.

$$m_{1,eff} = J_A \frac{\dot{\theta}_1^2}{\dot{d}_1^2} \quad (2.61)$$

The formula gave a variable effective mass working on cylinder 1 (jib tilt cylinder) corresponding to figure 2.41.

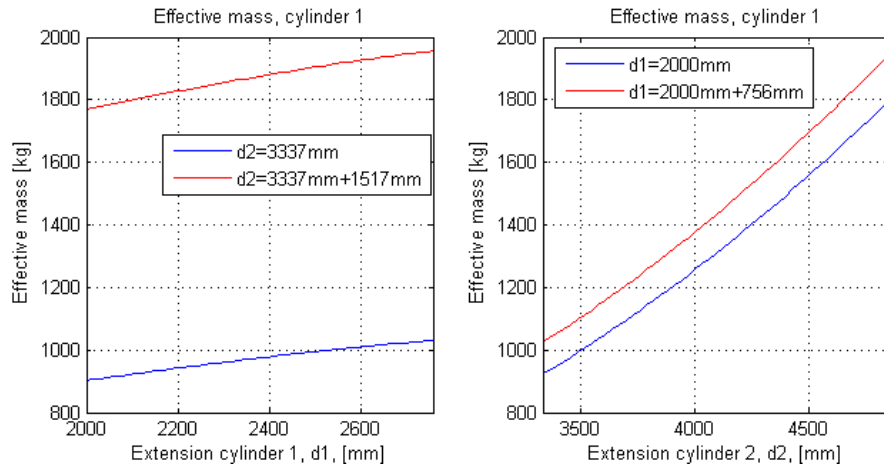


Figure 2.41: Effective mass dependent on cylinder positions

The effective mass of cylinder 2 is simply the sum of m_2 and m_3 , because the cylinder perform a pure translation of the body parts two and three.

$$m_{2,eff} = m_2 + m_3 \quad (2.62)$$

2.9 Effective force due to gravity

The effect of gravity on the BC is nonexistent since all motions occurs in the horizontal plane and is guided with rails. On the LGA the gravity will have a larger influence. Because the simulation model is one dimensional, only the dynamic forces due to accelerations of inertias and masses will be visible. To implement the static forces acting on the cylinders, the forces were calculated in a function block implemented in the simulation model controlling an ideal force acting on each cylinder. Forces due to centripetal acceleration, friction and weight of hydraulic cylinders are neglected. The forces counted for is the gravitational force acting on the telescope arm. The forces acting on the jib tilt cylinder (cylinder 1) is calculated due to moment equilibrium. The cylinder force F_{c1} then becomes,

$$\sum M_A = 0 = X_G m_{tot} g - F_{c1} R_{cy} \cos \theta_2 + F_{c1} R_{cx} \sin \theta_2 \quad (2.63)$$

$$F_{c1} = \frac{X_G m_{tot} g}{R_{cy} \cos \theta_2 - R_{cx} \sin \theta_2} \quad (2.64)$$

where g is the gravitational acceleration ($9.81m/s^2$), X_G is the global x-coordinate of the mass center (eq. 2.55), m_{tot} is the total weight of the moving masses on the LGA ($m_1 + m_2 + m_4$), θ_1 is the telescope angle, θ_2 is the jib tilt cylinder angle, and F_{c1} is the static force acting on cylinder one (fig 2.42).

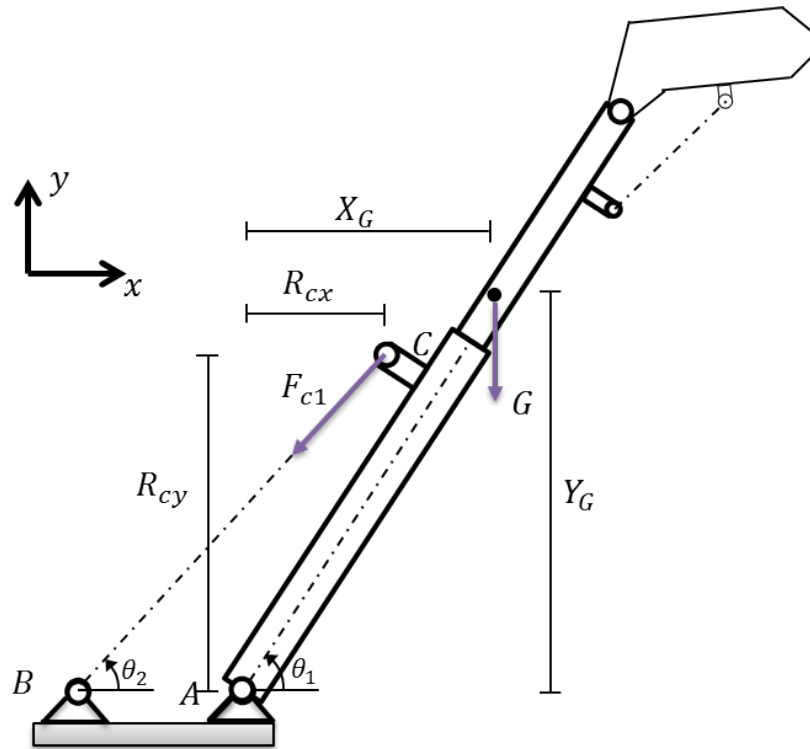


Figure 2.42: Simplified model of the LGA to calculate cylinder forces

The static forces acting on the telescope cylinder (cylinder 2) are caused by the inner telescope arm (m_2) and the gripper head (m_3).

$$F_{c2} = \sin \theta_1 \cdot (m_2 + m_3) \cdot g \quad (2.65)$$

Where m_2 and m_3 are the masses of the telescopic arm and the gripper head, and F_{c2} is the static force acting on cylinder two (inside the telescope arm).

2.10 Simulink model

2.10.1 Bridge Crane

The simulation model was assembled due to the corresponding drawing sheets (app. B). Orifices due to pipes and bendings are not implemented in the model.

To explain the initial positions of the bridge crane, the figure below is made. The tool point (TP) position in fig 2.43 is at point [0,0].

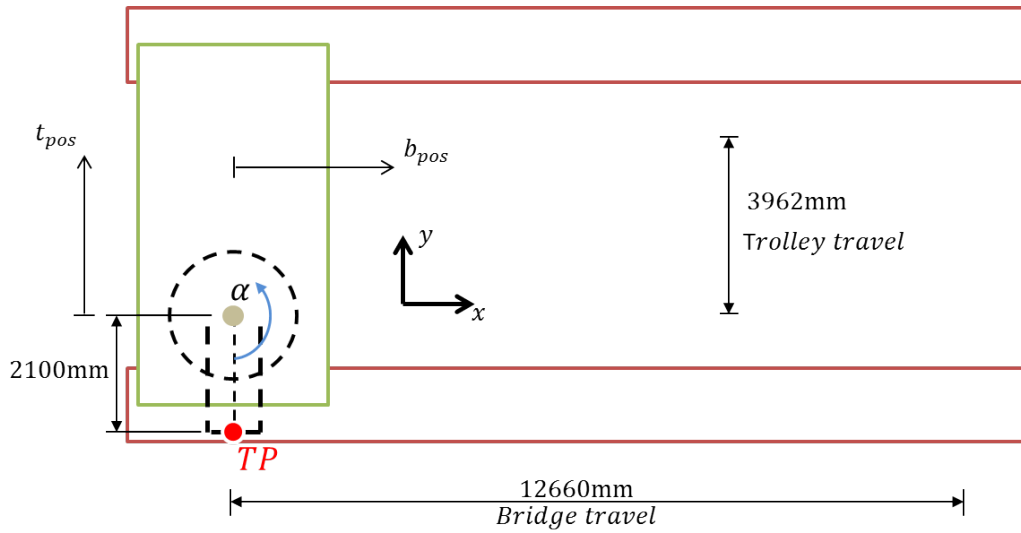


Figure 2.43: BC model description

Hence to the geometry in fig 2.43 the tool point position,

$$x = 2100 \sin \alpha + b_{pos} \quad (2.66)$$

$$y = 2100 - 2100 \cos \alpha + t_{pos} \quad (2.67)$$

where b_{pos} and t_{pos} is the bridge travel and trolley travel position given by the motor rotation angle in the model.

CHAPTER 2. SIMULATION MODEL

The simulink model consists of three main circuits (fig 2.44), bridge travel, trolley travel and slewing. Each circuit is very similar and consists of a directional servo valve, mentioned in section 2.2. All circuits are connected with a hydraulic motor, and in between of the motor and the directional valve it is placed a motion control valve. On the motor shafts there is connected a friction moment, and an inertia corresponding to the weight and gearing of the mechanical system.

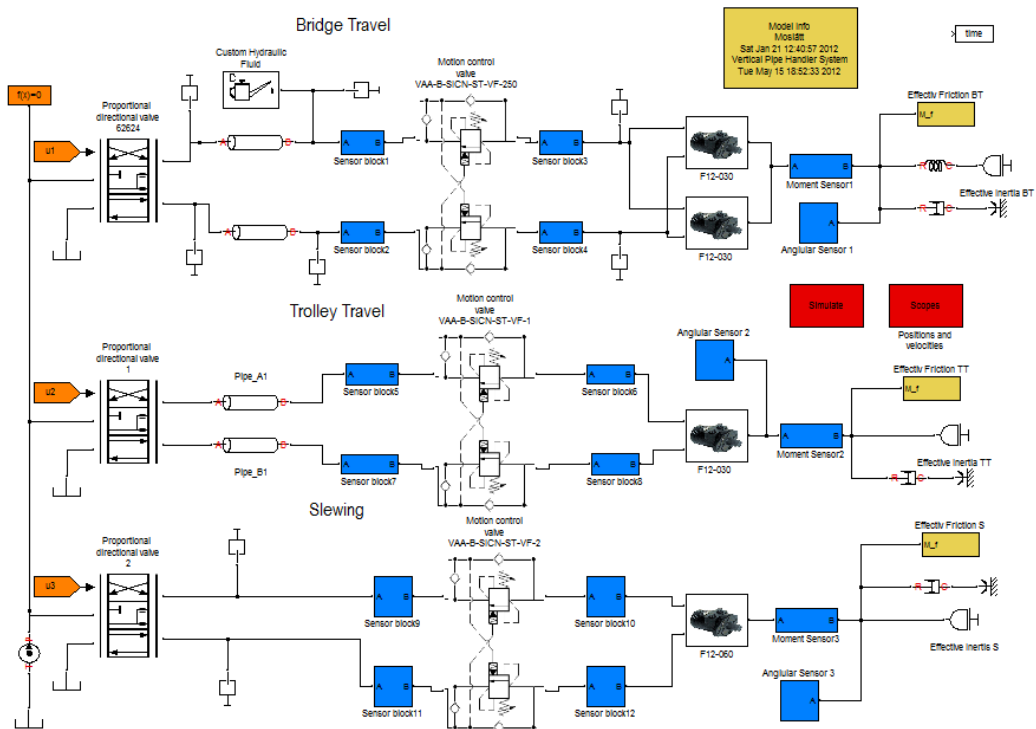


Figure 2.44: Simulation model bridge crane

CHAPTER 2. SIMULATION MODEL

From the model it is possible to extract a lot of data, for instance pressures, spool positions, motor shaft moment, velocities, control signals, and flow consumption. To demonstrate this a the trolley travel is simulated (fig 2.45).

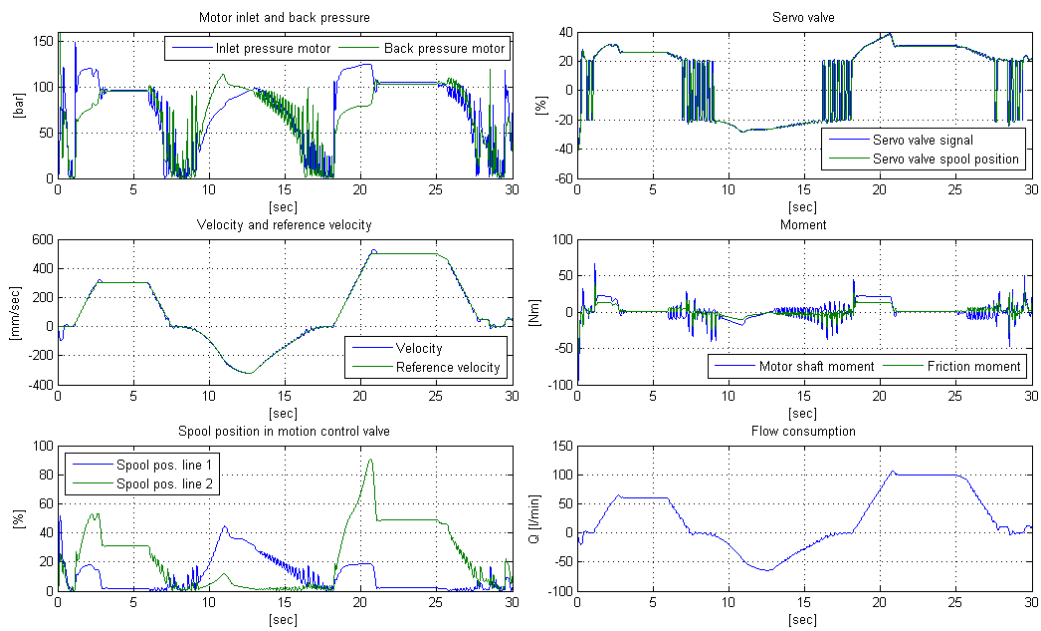


Figure 2.45: Simualed results for trolley travel

2.10.2 Lower guiding arm

The lower guiding arm is built due to the drawing sheets (app. C). The forces and variable inertias are calculated in the yellow function block (on the right side in fig 2.46).

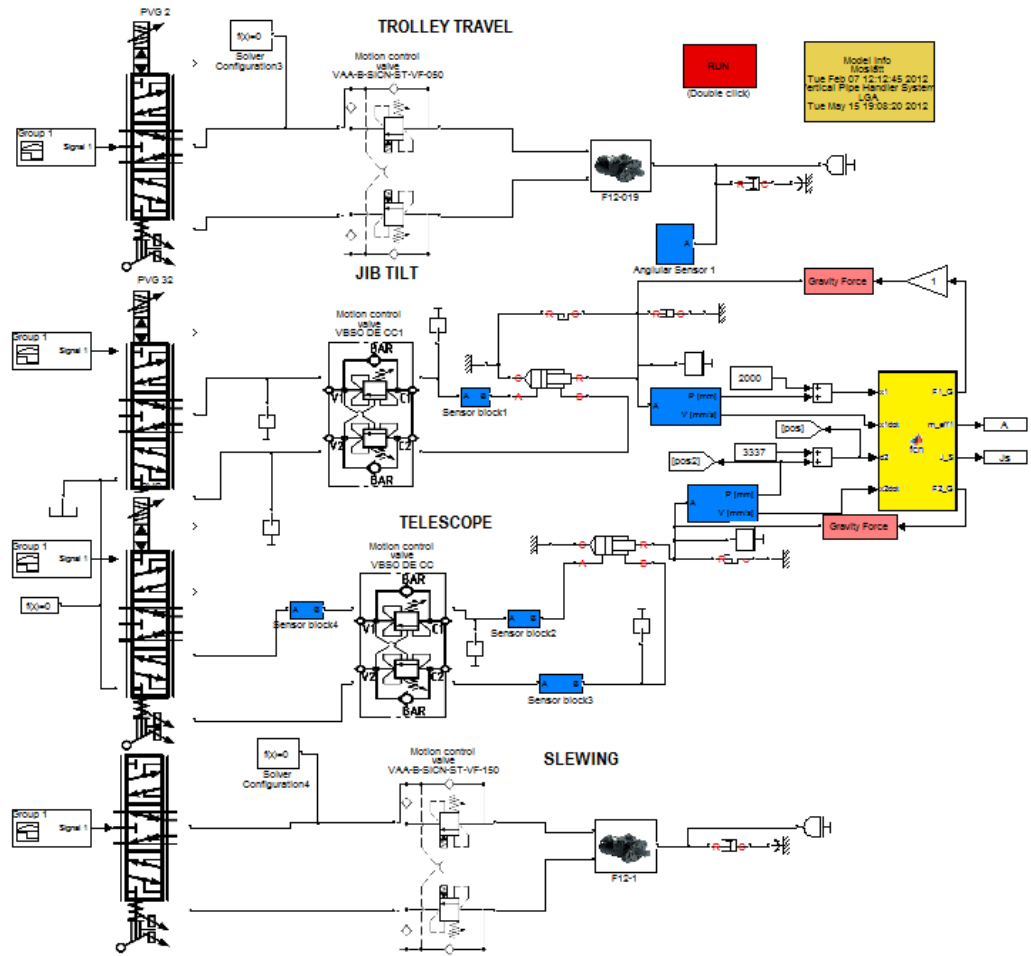


Figure 2.46: Simulation model LGA

Experimental Test

3.1 Test introduction

The modeling of the overcenter valves is important for the overall modeling of the bridge crane and the lower guiding arm. Therefore, experimental work was carried out to investigate validity of the modeling approach and for identify parameters. A test was performed on the VAA-B-SICN-ST-VF-250 overcenter valve from Bosch Rexroth Oil Control. This specific valve is used with all three hydraulic motors on the bridge crane. The test was conducted to determine spring stiffness, spool response and to validate the crack pressure setting of the valve.

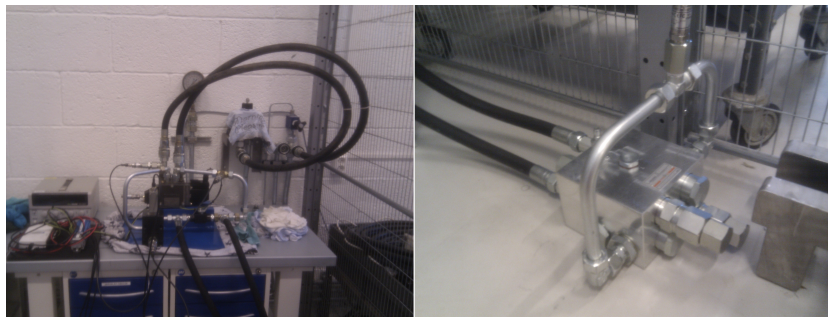


Figure 3.1: Test rig assembly

3.2 Test rig and measure points

The test assembly was built up as shown in figure 3.2, seen bellow. Between the PVG and measure point p_1 and p_2 there is used pipes, and from the flow sensor and p_2 it is used tubes with a length of approximately 1m each. Measure point p_3 is connected with pipes.

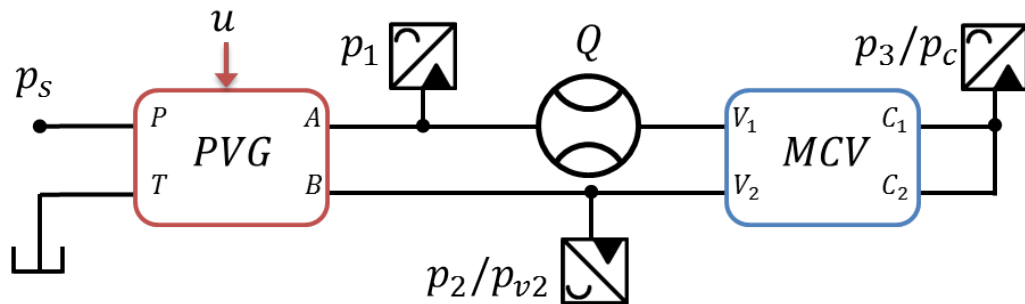


Figure 3.2: Test rig diagram.

PVG: Proportional directional valve. MCV: Motion control valve

The measure points (MP) signal names are related to figure 3.2

MP	Signal	Description	Type	Unit
1	p_1	A-port pressure, control valve	State	Bar or MPa
2	p_2	B-port pressure, control valve	State	Bar or MPa
3	p_3	Pressure on "load side" of mcv	State	Bar or MPa
4	Q	Flow through port A, control valve	State	Bar or MPa
5	u	Command signal, PVG	Input	%

Table 3.1: Measure points

3.3 Test Sequences

These three tests were executed with three different spring settings. The first one was with approximately the standard setting, the two others was plus and minus one turn on the spring adjustment screw.

Crack pressure test

To find the crack pressure for the specific setting, the PVG spool position was slowly ramped up manually. The test sequence was terminated when a visible flow was measured.

Multistep

To get some static measurements, the spool position was stepped up gradually to maximum travel.

Step response

In this sequence the PVG spool position was stepped from 0% up to 100%.

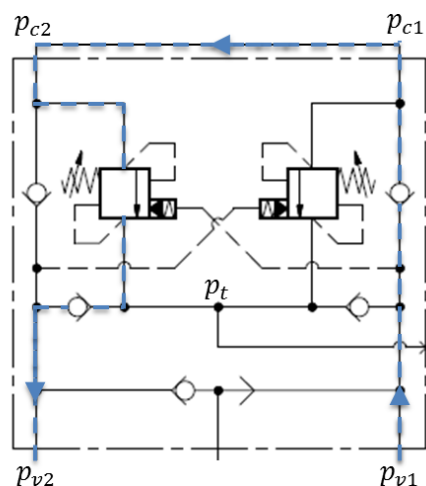


Figure 3.3: Flow route through the valve during test

3.4 Result

3.4.1 Test sequence 1

In this sequence the goal was to determine the actual crack pressure setting for each of the three test settings. This crack pressure is important to later calculations of spool positions in section 3.4.2.

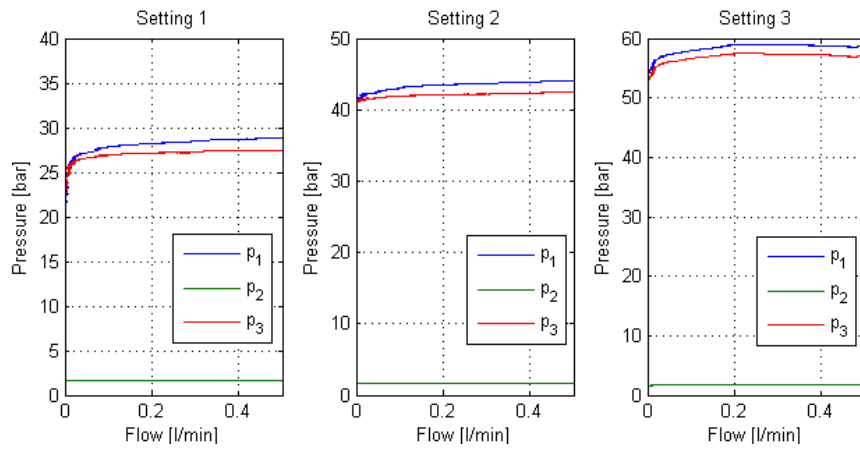


Figure 3.4: Opening pressure. Setting 1, 2, 3.

To calculate the crack pressure from these measurements, it was assumed that the spool position is equal zero when the flow increase becomes measurable. From eq 2.11 the following equation was derived. It assumes that spool positions is equal to zero ($u = 0$), that both parts of the spool are connected ($N > 0$, see fig.2.15) and that the pressure losses across the two check valves (fig.3.3) is equal ($p_t - p_{v2} = p_{v1} - p_c$).

$$p_{cr} = p_{v1} \cdot \alpha + p_{c2} - (p_{v2} + (p_{v1} - p_{c1})) \cdot (\alpha + 1) \quad (3.1)$$

$$p_{cr} = p_c \cdot (\alpha + 2) - p_{v1} - p_{v2} \cdot (\alpha + 1), \quad p_c = p_{c1} = p_{c2} \quad (3.2)$$

p_{cr} describe the total crack pressure including both springs ($p_{cr} = p_{cr1} - p_{cr2}$)

CHAPTER 3. EXPERIMENTAL TEST

Setting	α	p_1	p_{v1}	p_{v2}	p_c	Set screw	Crack pr., p_{cr}
1	2.8	27.8bar	26.8bar	1.7bar	26.8bar	std. -1turn	95.4bar
2	2.8	42.2bar	41.2bar	1.7bar	41.6bar	std.	152.0bar
3	2.8	59.0bar	58.0bar	1.7bar	57.5bar	std. +1turn	211.5bar

Table 3.2: Crack pressures, test settings and results

These results (table 3.2) are manually readings from test result plots, and correspond to the average pressure from 0 to $0.5l/min$. The pressure, p_{v1} , is calculated based on a pressure drop of 1bar over the flow sensor at $Q \approx 0$ (eq 3.4). The datasheet[8] say $2bar$ but this did not correspond with the measurements taken. From the results the assumption about the contact force N being larger than zero is confirmed through eq2.4. The results corresponds quite well with the given specifications in the datasheet[6]. The standard setting should give a crack pressure of $150bar$ and 1 clockwise turn on the set screw should correspond to an increase in crack pressure of $62bar$ [6]. These test results gave a standard setting crack pressure of $152bar$ and an increase of approximately $58bar/turn$. The fact that the crack pressure increases linearly with x turns on the adjustment screw indicates that the spring force is linear and that the spring constant is, indeed, constant. This assumption will be important in the next test sequence (sequence 2).

3.4.2 Test sequence 2

In this sequence the flow from the directional control valve is ramped up in steps. Each step moves the main spool of the directional control valve 8% of max travel. The steady state values from each step are logged and used to estimate the spring stiffness.

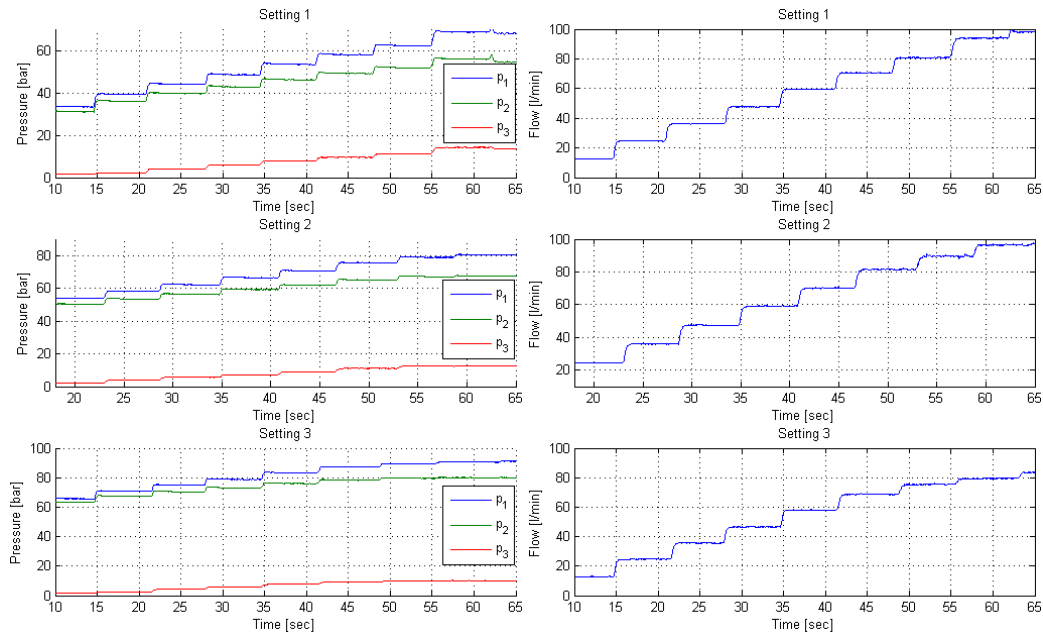


Figure 3.5: Results from test sequence 2

The first seven steps for each setting was manually read out:

$$\begin{aligned}
 SET_1 &= \begin{pmatrix} p_1 & p_2 & p_3 & Q \\ 33.4 & 1.7 & 31.2 & 12.5 \\ 39.3 & 2.3 & 36.0 & 24.6 \\ 44.1 & 4.2 & 39.6 & 36.3 \\ 48.6 & 6.0 & 42.8 & 47.7 \\ 53.3 & 7.9 & 46.2 & 59.6 \\ 58.0 & 9.6 & 49.2 & 70.5 \\ 62.2 & 11.3 & 51.8 & 80.8 \end{pmatrix} &
 SET_2 &= \begin{pmatrix} p_1 & p_2 & p_3 & Q \\ 53.8 & 2.1 & 50.3 & 24.5 \\ 58.0 & 3.8 & 53.5 & 36.0 \\ 62.2 & 5.6 & 56.5 & 47.4 \\ 66.5 & 7.3 & 59.2 & 59.2 \\ 70.6 & 8.95 & 61.9 & 70.2 \\ 75.5 & 11.1 & 65.1 & 81.5 \\ 78.9 & 12.5 & 67.1 & 89.6 \end{pmatrix} &
 SET_3 &= \begin{pmatrix} p_1 & p_2 & p_3 & Q \\ 65.8 & 1.7 & 63.5 & 12.8 \\ 70.8 & 2.4 & 67.4 & 24.6 \\ 74.9 & 4.2 & 70.4 & 35.6 \\ 78.8 & 5.8 & 73.1 & 46.6 \\ 83.3 & 7.6 & 76.0 & 57.9 \\ 87.1 & 9.1 & 78.3 & 68.8 \\ 89.4 & 9.8 & 79.5 & 75.5 \end{pmatrix}
 \end{aligned}$$

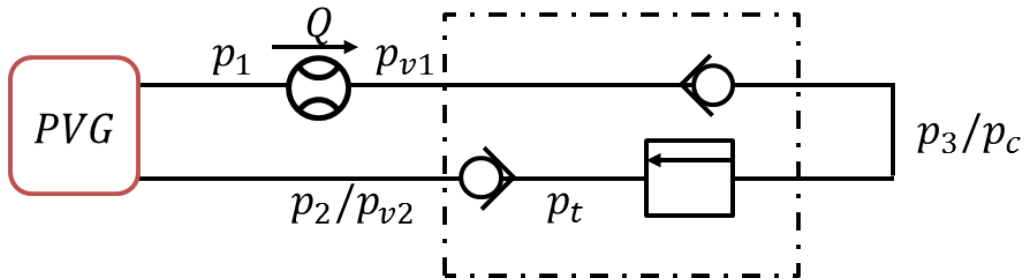


Figure 3.6: Test assembly overview of the measurement points

Fig 3.6 show the transmitter positions. Notice that the logged values are p_1 , p_2 and p_3 , and that they correspond to the p_{v1} , p_{v2} and p_c that are needed to identify the spring stiffness.

$$p_{v1} = p_1 - \Delta p_f \quad p_{v2} = p_2 \quad p_c = p_3$$

Δp_f : Pressure loss across the flow sensor.

The pressure loss across the flow sensor increases linearly with the flow according to the datasheet[8]:

$$\Delta p_f = 2 \cdot 10^5 Pa + 24000 \cdot 10^5 \frac{Pa \cdot s}{m^3} \cdot Q \quad (3.3)$$

This formula did not match the measured data and a change of the formula was made:

$$\Delta p_f = 1 \cdot 10^5 Pa + 30000 \cdot 10^5 \frac{Pa \cdot s}{m^3} \cdot Q \quad (3.4)$$

CHAPTER 3. EXPERIMENTAL TEST

The next steps describe the spring stiffness calculation.

From the orifice equation we get:

$$Q = A_d C_d \sqrt{\frac{2}{\rho} \Delta p} \rightarrow A_d = \frac{Q \sqrt{\rho}}{C_d \sqrt{2 \Delta p}} \quad (3.5)$$

The pressure loss over relief valve is:

$$\Delta p = p_{c2} - p_t \quad (3.6)$$

Assuming that $p_t = p_{v2} + (p_{v1} - p_{c1})$ and $p_c = p_{c1} = p_{c2}$

$$\Delta p = 2p_c - p_{v2} - p_{v1} \quad (3.7)$$

Combining eq3.5 and eq3.7, yields:

$$A_d = \frac{Q \sqrt{\rho}}{C_d \sqrt{2} \sqrt{2p_c - p_{v2} - p_{v1}}} \quad (3.8)$$

The spool position is derived from A_d :

$$u = \frac{A_d}{A_{d,max}} \quad (3.9)$$

The spool position is also given by pressure equilibrium, see eq 2.11 (assumed $p_t = p_{v2} + (p_{c1} - p_{v1})$ and $p_c = p_{c1} = p_{c2}$):

$$u = \frac{p_c(\alpha + 2) - p_{cr} - p_{v2}(\alpha + 1) - p_{v1}}{k_{p1} + k_{p2}} \quad (3.10)$$

Combining equations 3.8, 3.9 and 3.10, yields:

$$k_p = k_{p1} + k_{p2} \quad (3.11)$$

$$k_p = \frac{A_{d,max} C_d \sqrt{2} \sqrt{2p_c - p_{v2} - p_{v1}}}{Q \sqrt{\rho}} \cdot (p_c(\alpha + 2) - p_{cr} - p_{v2}(\alpha + 1) - p_{v1}) \quad (3.12)$$

Adopting the spring stiffness formula in equation 3.12, a highly non-constant spring stiffness was obtained (fig 3.7). The result show curves that are mainly dependent on flow and crack pressure setting. The irregularity in setting 1 is most likely caused by the low crack pressure setting. The minimum allowed crack pressure is set to 100bar [6]. Too low crack pressure setting could cause a gap between spring and spool. This mean that only one of the two springs is in contact with the spool. Hence it would cause a discontinuity in total spring stiffness.

From the crack pressure measurements it is known that the spring stiffness is

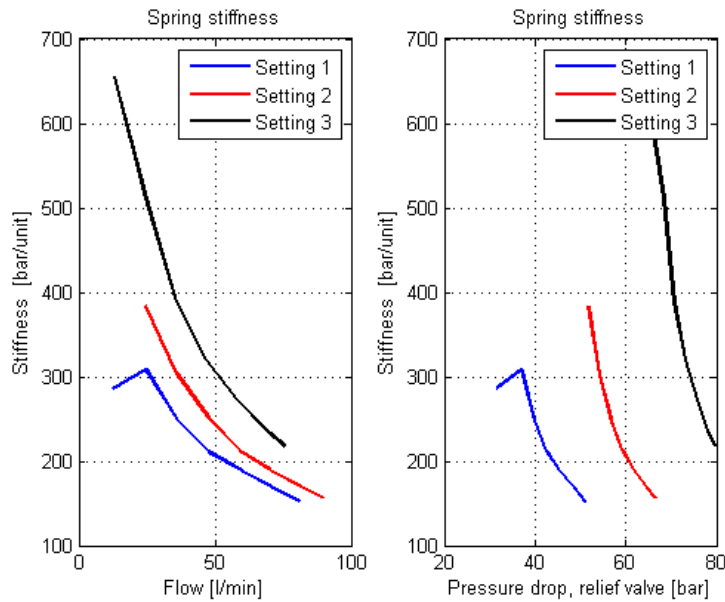


Figure 3.7: Spring stiffness vs flow and pressure

approximately constant. Therefore, the results indicate that there is additional forces acting on the spool that is not yet taken into account. Since this force is complex and dependent of the orifice geometry, it is not possible to find an analytical expression. In stead a force function that ensures a constant spring stiffness has been introduced. Since all three settings have different slopes, it became necessary to make the new function dependent of the p_{cr} setting. Another thing that was important was that the force should not affect the p_{cr} . Hence the force should be equal zero at low flow ($p_F(Q = 0) = 0$). The new force was added in to the existing pressure equilibrium as a positive force/pressure working on the ring pressure area, A_r (fig 2.15).

CHAPTER 3. EXPERIMENTAL TEST

The force was added in the original pressure equilibrium:

$$\begin{aligned}
 p_F(Q) &= (1.66 \cdot 10^{-5} \cdot Q_{l/min}^4 - 3.0 \cdot 10^{-3} \cdot Q_{l/min}^3 + 0.071 \cdot Q_{l/min}^2 + 13.2 \cdot Q_{l/min}) \cdot \frac{Q \cdot z_1}{\sqrt{\Delta p}} & 180bar < p_{cr} \\
 p_F(Q) &= (-1.9 \cdot 10^{-5} \cdot Q_{l/min}^4 + 5.2 \cdot 10^{-3} \cdot Q_{l/min}^3 - 0.55 \cdot Q_{l/min}^2 + 28.9 \cdot Q_{l/min}) \cdot \frac{Q \cdot z_1}{\sqrt{\Delta p}} & 120bar > p_{cr} < 180bar \\
 p_F(Q) &= (-4.4 \cdot 10^{-5} \cdot Q_{l/min}^4 + 0.011 \cdot Q_{l/min}^3 - 1 \cdot Q_{l/min}^2 + 40.5 \cdot Q_{l/min}) \cdot \frac{Q \cdot z_1}{\sqrt{\Delta p}} & p_{cr} < 120bar
 \end{aligned}$$

The constants were manually tuned:

$$z_1 = 4.0847e + 5 \cdot 10^5 \quad \Delta p = p_c - p_t \quad Q_{l/min} = Q \cdot 60000$$

This p_F was added as a pressure in pressure equilibrium equation (eq 2.10)

$$p_{eq} = p_{v1}\alpha + p_{cr2} - k_{v2} \cdot u - p_t(\alpha + 1) + p_{c2} - p_{cr1} - k_{p1} \cdot u + p_F$$

Assumed:

$$p_{eq} = 0, \quad p_t = p_{v2} + (p_{v1} - p_{c1}), \quad \Delta p = p_{c2} - p_t, \quad p_c = p_{c1} = p_{c2}$$

$$\rightarrow u = \frac{p_c(\alpha + 2) - p_{cr} - p_{v2}(\alpha + 1) - p_{v1} + p_F}{k_{p1} + k_{p2}} \quad (3.13)$$

Combine equation 3.8, 3.9, 3.11.

$$k_p = \frac{C_d \sqrt{2} \sqrt{2p_c - p_{v2} - p_{v1}}}{Q \sqrt{\rho}} \cdot (p_c(\alpha + 2) - p_{cr} - p_{v2}(\alpha + 1) - p_{v1} + p_F) \quad (3.14)$$

Using equation 3.14 resulted in a more even spring stiffness (fig 3.8).

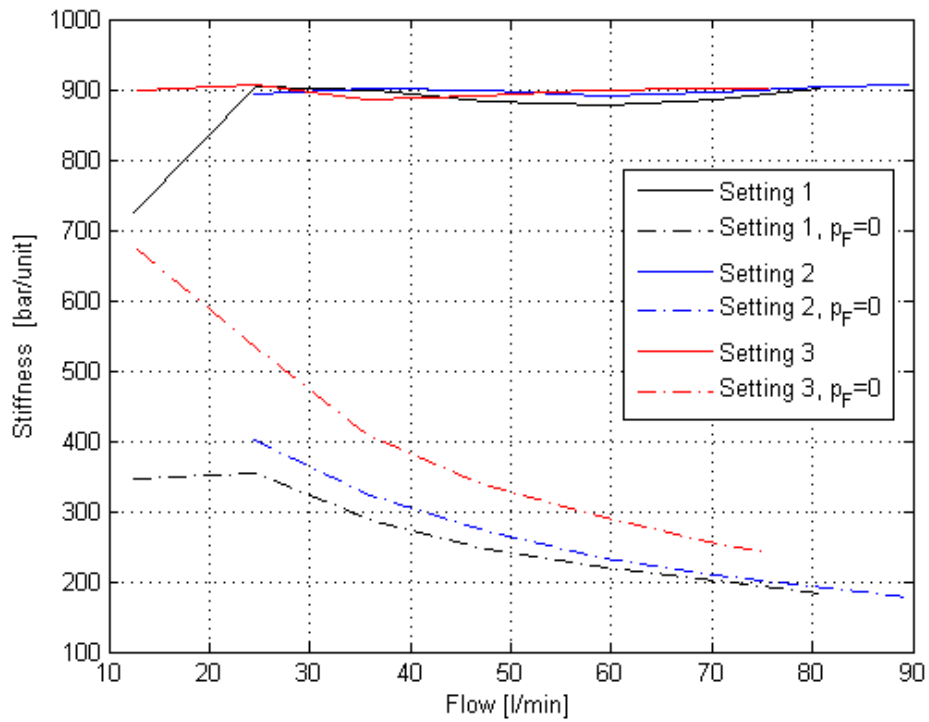


Figure 3.8: Compared results with and without the additional pressure force, p_F

The spring stiffness settled around $895 \pm 15 \text{bar/unit}$. As seen in fig 3.8 the highest accuracy was obtained between 20l/min and 100l/min . This result confirms that the function are making the model more realistically.

3.4.3 Test sequence 3

In this test the PVG was stepped from its neutral position to max opening and half opening. This test gave some pressure peaks before settling. These peaks are mainly caused by the spool response.

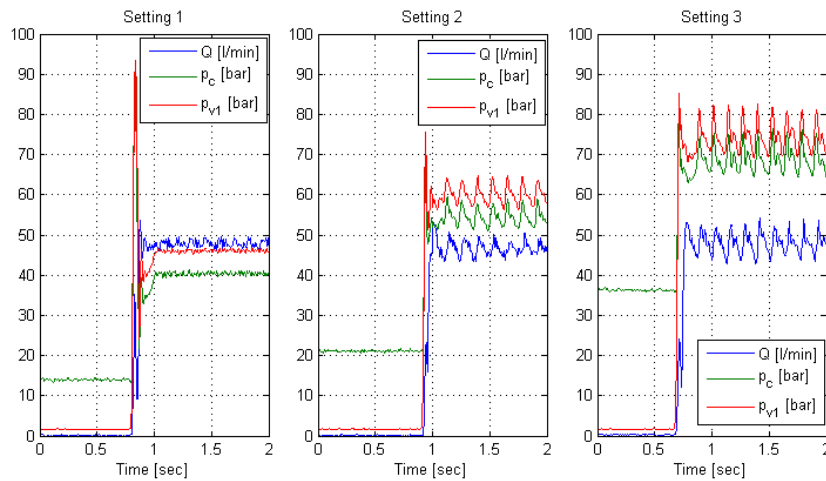


Figure 3.9: Step response. 0% - 50%

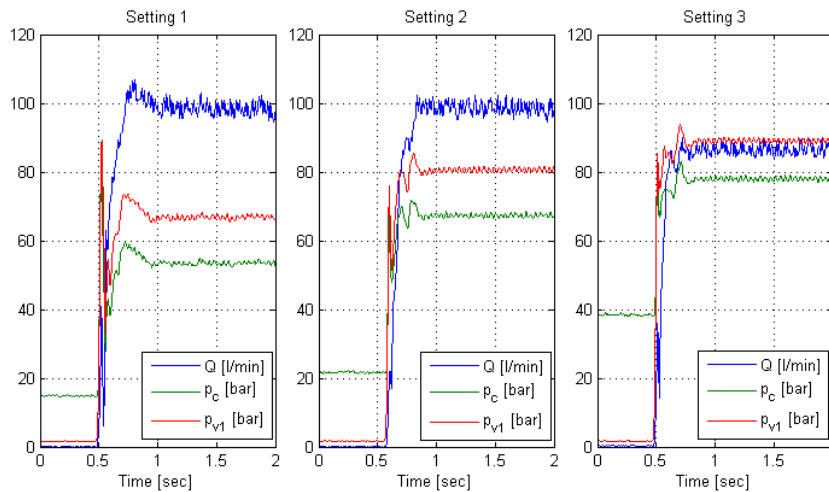


Figure 3.10: Step response. 0% - 100%

3.5 Comparing physical with simulated results

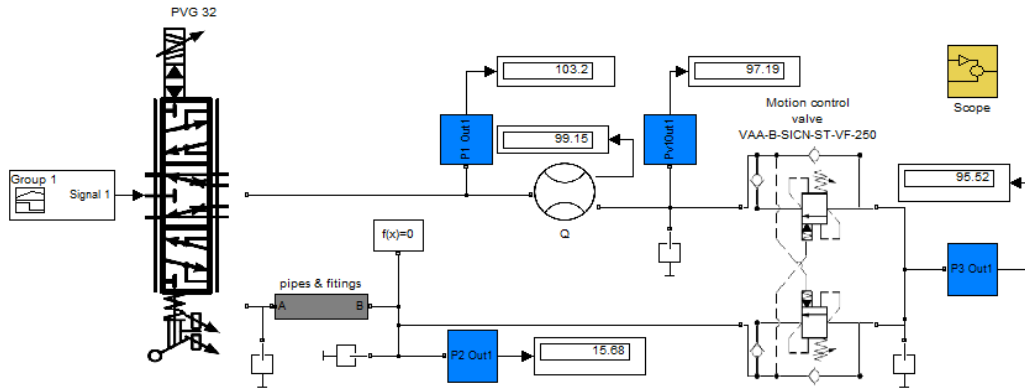


Figure 3.11: Simulink model of test assembly

To compare and validate the results a simulation model in simulink was built corresponding to the physical assembly. The pressure loss across the flow rate sensor was set due to eq 3.4. There is not implemented any pipes and fittings with losses except the gray block. This block has a variable orifice which is implemented to get the correct p_{v2} pressure due to the experimental tests. A deviation of the p_{v2} pressure will cause an offset error in p_c and p_{v1} . This error will also lead to a different spool position and generate an even higher deviation in p_{v1} and p_c .

3.5.1 Crack pressure

The crack pressure is calculated based on p_{v1} , p_{v2} and p_c .

$$p_{v1} = p_1 - \Delta p_f \qquad p_{v2} = p_2 \qquad p_c = p_3$$

Δp_f : Pressure loss across the flow sensor.

The pressure loss across the flow sensor increases linearly with the flow (eq.3.4):

$$\Delta p_f = 1 \cdot 10^5 + 30000 \cdot 10^5 \cdot Q \qquad (3.15)$$

	Setting 1		Setting 2		Setting 3	
	Exp.	Sim.	Exp.	Sim.	Exp.	Sim.
$p_1[bar]$	27.8	28.1	42.2	42.8	59.0	58.6
$p_{v1}[bar]$	26.8	27.1	41.2	41.7	58.0	57.7
$p_2[bar]$	1.7	1.5	1.7	1.5	1.7	1.5
$p_3[bar]$	26.8	26.6	41.6	41.2	57.5	57.2
$p_{cr}[bar]$	95.4	94.9	152.0	150.3	211.5	211.3

Table 3.3: Crack pressures from experimental test and simulation

The results are satisfying and the deviations in p_{cr} varies from 0.2 to 1.7bar. It can be seen that the p_{cr} function is very sensitive. In setting 2 the pressures p_1 , p_2 and p_3 have a maximum deviation of only 0.6bar, but the p_{cr} fails with 1.7bar.

3.5.2 Spring stiffness

The same "multistep" procedure was done in simulink, and the corresponding values are inserted in table 3.4. The simulated values for pressure p_1 , p_2 , p_3 , and flow Q are compared to the experimental test data values.

	p_1 [bar]		p_2 [bar]		p_3 [bar]		Q [l/min]	
	Sim.	Exp.	Sim.	Exp.	Sim.	Exp.	Sim.	Exp.
Set. 1	35.4	33.4	1.6	1.7	33.0	31.2	12.4	12.5
	39.2	39.3	2.5	2.3	36.0	36.0	24.4	24.6
	42.9	44.1	3.9	4.2	39.0	39.6	36.2	36.3
	47.1	48.6	5.6	6.0	42.5	42.8	47.6	47.7
	51.4	53.3	7.6	7.9	46.1	46.2	59.5	59.6
	54.3	58.0	9.4	9.6	48.4	49.2	70.4	70.5
	56.1	62.2	10.9	11.3	49.6	51.8	80.8	80.8
Set. 2	53.3	53.8	2.5	2.1	50.2	50.3	24.5	24.5
	57.1	58.0	3.9	3.8	53.2	53.5	36.0	36.0
	60.6	62.2	5.6	5.6	56.0	56.5	47.4	47.4
	64.2	66.5	7.5	7.3	59.0	59.2	59.2	59.2
	67.3	70.6	9.4	8.9	61.4	61.9	70.3	70.2
	69.7	75.5	11.0	11.1	63.1	65.1	81.6	81.5
	71.2	78.9	11.9	12.5	64.1	67.1	89.6	89.6
Set. 3	65.9	65.8	1.7	1.7	63.5	63.5	12.8	12.8
	70.4	70.8	2.5	2.4	67.3	67.4	24.5	24.6
	73.9	74.9	3.8	4.2	70.1	70.4	35.5	35.6
	77.1	78.8	5.5	5.8	72.6	73.1	46.7	46.6
	80.2	83.3	7.3	7.6	75.0	76.0	57.9	57.9
	82.9	87.1	9.1	9.1	77.1	78.3	68.8	68.8
	84.5	89.4	10.1	9.8	78.3	79.5	75.5	75.5

Table 3.4: Multistep results

CHAPTER 3. EXPERIMENTAL TEST

The interesting value is the pressure drop over the pressure relief valve. The other pressure drops in the motion control valve is already confirmed (see section 2.4.2). The pressure drop over the pressure relief valve is determined by the spool position which again depends on the pressures acting on the spool. Hence the difference between the simulated results and the experimental results of the pressure drop over the main spool will indicate the accuracy of the simulated model (fig 3.12).

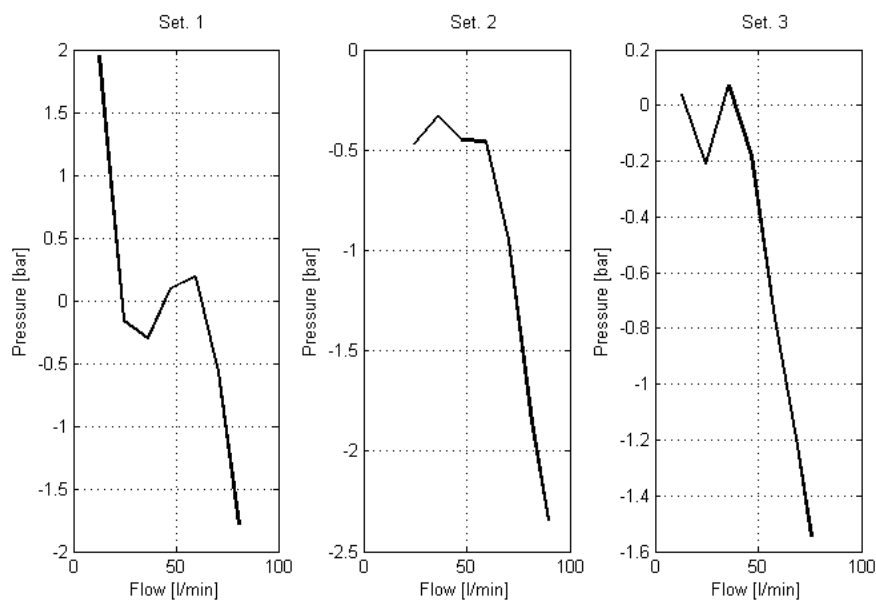


Figure 3.12: Difference (error) between the pressure drop across the spool ($p_3 - p_2$) in the simulation model and the experimental test

The figure show a high accuracy around 50 l/min , with a pressure drop error less than 0.5 bar . As the flow approaches 100 l/min the error increases.

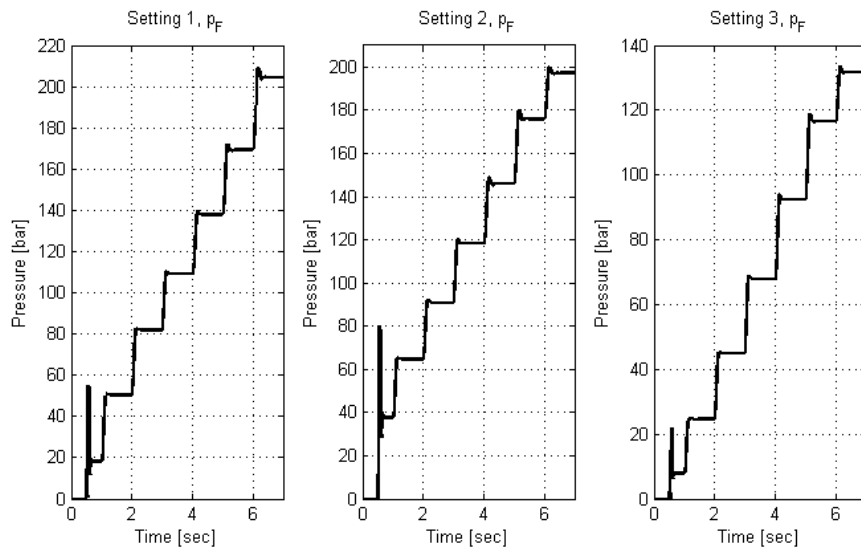


Figure 3.13: The flow force divided by the ring pressure area, A_r , giving p_F

In figure 3.13 the additional flow force added as p_F in the pressure equilibrium is shown. The results correspond with the pressure force added in the multistep test.

3.6 Spool response

The response test was executed by giving a stepped input signal to the PVG. The experiment was conducted with steps from 0-100% and 0-50%. Because this test did not have the ability to measure the spool position directly, the pressure between the two ports p_{c1} and p_{c2} was used, (p_c). The response of this pressure will give a good indication of the correctness of the spool response.

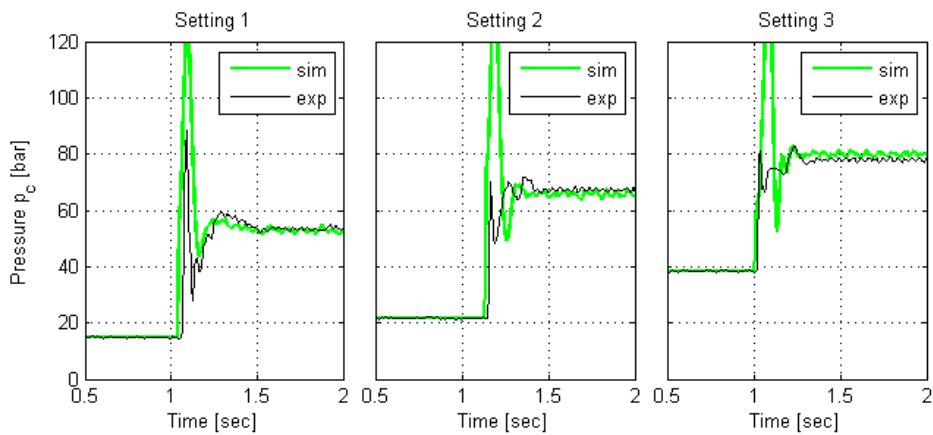


Figure 3.14: Response when the PVG spool is stepped from 0 to 100% opening.

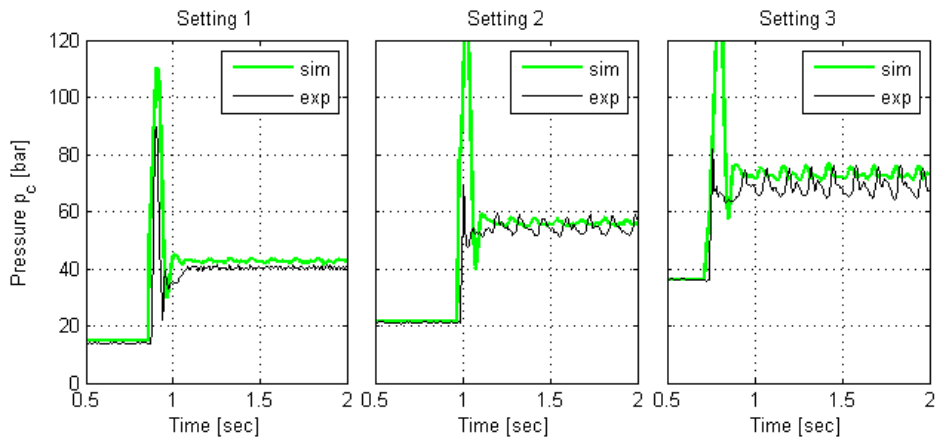


Figure 3.15: Response when the PVG spool is stepped from 0 to 50% opening.

From the results (fig 3.14 and 3.15) we see that most of the curves have a significant first peak. This peak appear because the fluid is pressurized before the

valve opens. Therefore, this peak will depend on the oil stiffness and/or volume of the pressure chamber p_3 (fig 3.11). Figure 3.16 show the effect of increasing the p_3 chamber volume. The next peak have a less steep slope and this slope represents the spool response. The spool response is tuned in such that the slopes of the second peak is quite similar (see left hand side plot in fig3.16).

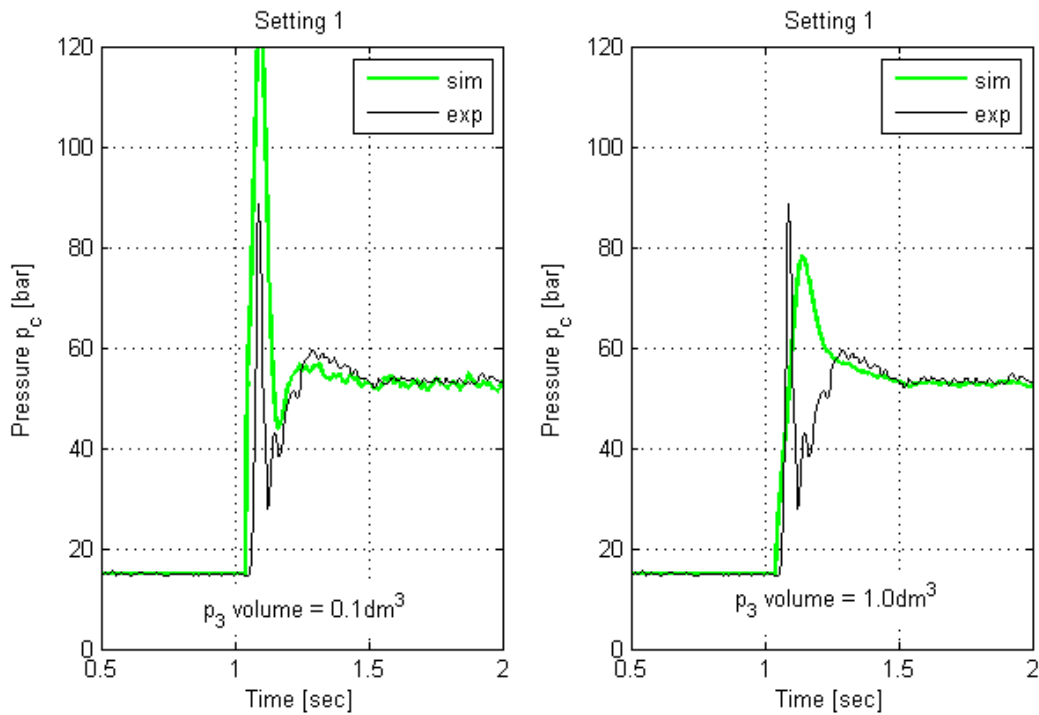


Figure 3.16: Response plot with a PVG spool step from 0-100%.

The results (fig 3.15 and 3.14) show a quite large deviation between the simulated and measured results of the highest crack pressure setting (setting 3, $p_{cr} = 211\text{bar}$). For setting 1 the results are good, and for setting 2 there are similarities but less accurate than setting 1.

With the existing model parameters it was difficult define the best and most correct fit. The pressure response that is measured is not only dependent of the spool response but also the volume sizes surrounding the spool. Another aspect that is not taken into account in the simulation model is the spool friction. The spool friction may have some stick slip properties that could contribute to give a more accurate model of the response. The friction may also include some hystere-

CHAPTER 3. EXPERIMENTAL TEST

sis effect caused by the sealing rings.

Aside from the frictional effects and other possible influences, the best fitted second order response (fig 3.14 and 3.15) was with a frequency about 50Hz, a damping ratio equal 1 and a volume in pressure chamber p_3 of 0.1*litre*.

3.7 Sub-conclusions

The results are good according to data sheets and the model versus experiments.

The spring stiffness measurements clearly revealed the need for an extra steady state force acting on the spool. It was assumed that this was related to the flow force and it was possible to develop a flow force model that supported the idea of a linear spring. Because the fitted force is only accurate for the three tested crack pressure settings (95bar, 152bar and 211bar) the model is only accurate for these settings. To keep the same accuracy for other crack pressure settings it is necessary to make new flow force curves, p_F .

Some important assumptions were made in this simulink model:

- The bendings, tubes and pipes between p_2 and the mcv, mcv and p_3 , and between the flow sensor and the mcv are ignored. This could cause some errors, especially at high flow rates.
- All simulation models uses an oil density of $850kg/m^3$ and a bulk modulus of $8 \cdot 10^8 Pa$.
- The flow force curves is this case only valid up to $100l/min$. If the is increased any further the deviation may increase.

Chapter 4

Optimization of VPHS

4.1 Intro

The subject of this chapter has mainly three objectives. Firstly to create a model and establish a suitable connection between the model and a possible optimization algorithm. Secondly which design parameters to optimize is evaluated. Finally an optimization routines with suitable cost functions and design parameters are executed. The results were used to create an insight of how these design parameters affect the performance.

4.2 Optimization model

To create a suitable model to connect with the algorithm some measures were needed to be carried out. This will involve shrinking and making the simulation model quick enough. By quick enough, it means that the model should be able to simulate the given sequence within such period of time that the time on the optimization routine is kept within reasonable limits. Since the vertical pipe handling system is very complex and has many components, it was necessary to shrink the model.

The pipe handler consists of two main part, the bridge crane and the lower guiding arm. Since a model for the overcenter valve used in the bridge crane was verified (chap. 3), it was beneficial to use parts of the bridge crane. The bridge travel drive line was chosen. This drive line consists of a hydraulic part with servo valve, overcenter valve, two motors, and a mechanical part with inertia and friction (fig 4.1).

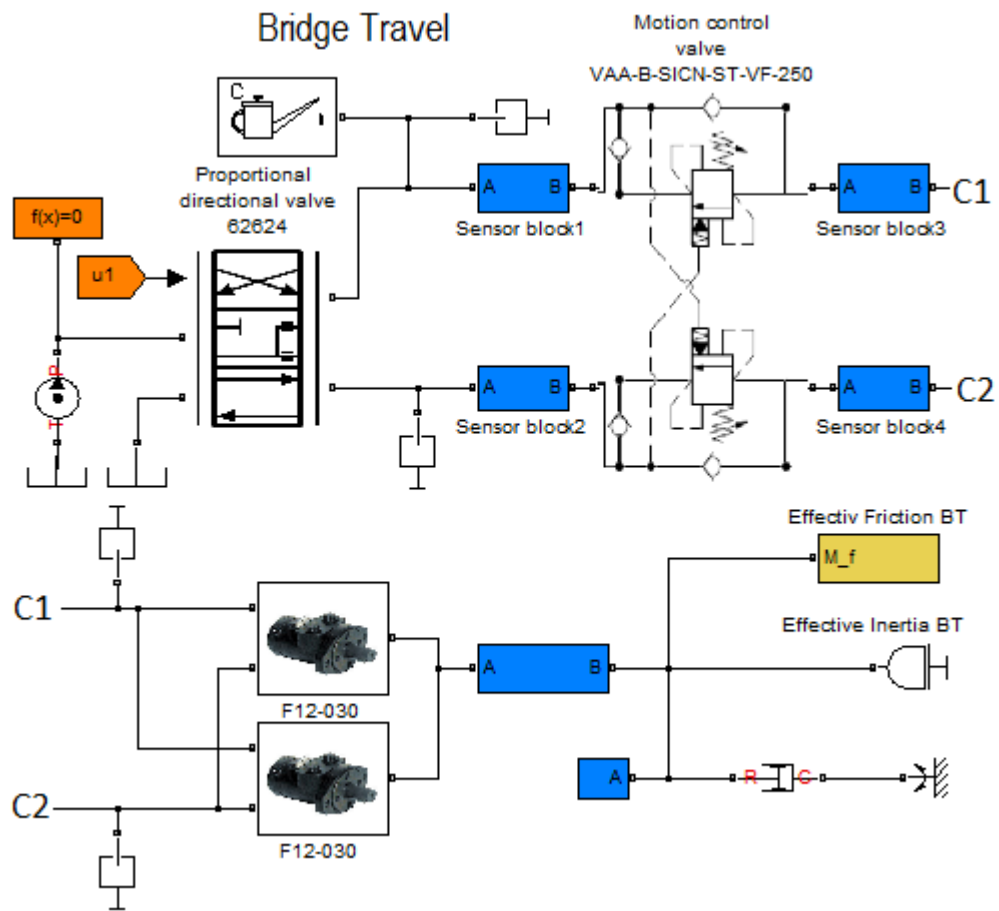


Figure 4.1: Simulation model used for optimization

The model (fig 4.1) was modeled in Matlab Simulink as a time domain model. Using Matlab made it convenient to apply the optimization routine. By implementing the optimization routine in scripts and commands, the model could easily be executed using existing commands in the Matlab program.

Another parameter which also have a large influence on the time consume is the simulated time. The velocity reference for this drive line last for 13seconds. This was shrunk to a simulation time of 3 seconds. To stay conservative the velocity was ramped four times faster than the original reference to a velocity of 400mm/s (fig 4.2).

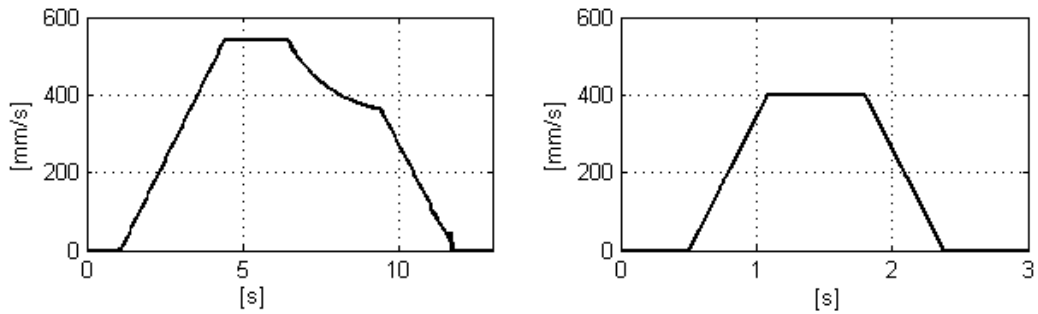


Figure 4.2: Original and new velocity reference

4.3 Design variables

The components that are focused on is mainly the over center valve, the directional servo valve and the controller.

From these components some specific parameters were chosen (table 4.1).

k_v	Feed forward velocity gain
k_p	Position error proportional gain
k_i	Position error integrator gain
k_{vp}	Velocity error proportional gain
ω_{pdv}	Natural frequency of the proportional directional valve spool
k_s	Spring stiffness in motion control valve
p	Pilot ratio in motion control valve

Table 4.1: Design parameters

4.4 Design criteria

In this optimization it has been focused on positioning error and vibrations. To weight the position, the squared position and velocity error was time integrated. The integrated values were scaled such that they had about the same weight (eq 4.1).

$$C_{pos} = 50 \cdot \int e_{pos}^2 dt + \int e_{vel}^2 dt \quad (4.1)$$

To weight the presence of noise and vibrations, the pressure on the inlet side of the motor was evaluated. A second order high pass filter was used on the pressure data to be able to measure the high frequency vibrations (fig 4.3). The high frequent

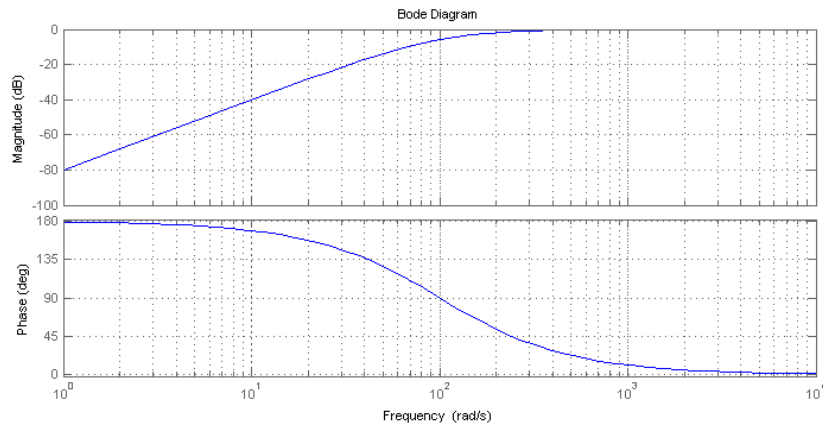


Figure 4.3: Second order high pass filter

signal noise is let through and the smooth signals are neglected (fig 4.4

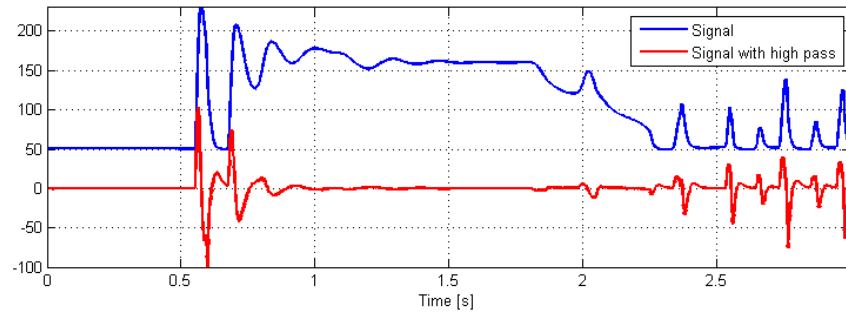


Figure 4.4: Example of a signal with and without the high pass filter.

The noise/vibration data were then integrated over time to obtain one scalar value (eq 4.2). This value represents the cost in terms of vibrations.

$$C_{vib} = 3 \cdot 10^{-8} \cdot \int p_{high}^2 dt \quad (4.2)$$

Where p_{high} is the high pass filtered inlet pressure data.

4.5 The complex optimization algorithm

The complex optimization algorithm is a numerical and heuristic method. The algorithm is based on a population consisting of n designs. The designs are randomly chosen from between the boundaries for the given variables. In each iteration the poorest design is identified, j , and the centroid of the remaining design is computed, \underline{y}^c . [4] The poorest design is the design that give the highest cost due to the chosen cost function and centroid is calculated as a mean value of the randomly chosen parameter population.

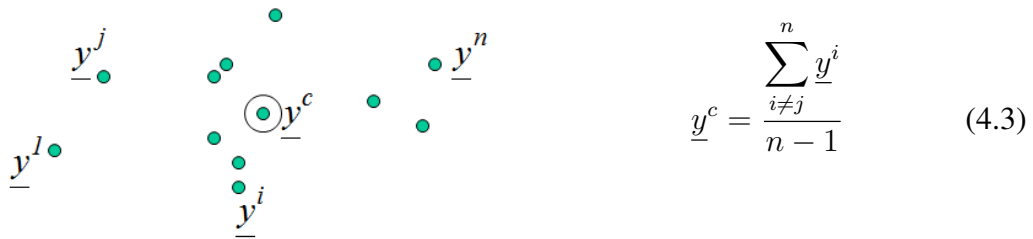


Figure 4.5: Population and centroid [4]

The worst design, j , is then mirrored over the centroid.

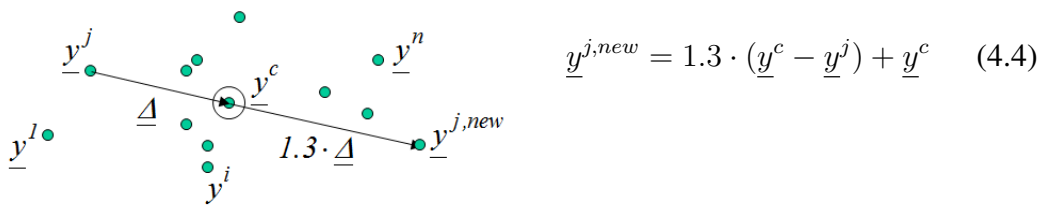


Figure 4.6: Worst design mirrored over the centroid [4]

If the newly mirrored design continues to be the worst design, the design parameters are moved toward the best design. How strongly it should be moved is dependent of how many times this design has been the worst in a row.

$$\underline{y}^{j,new} = 0.5 \cdot |\underline{y}^j + \epsilon \cdot \underline{y}^c + (1 + \epsilon) \cdot \underline{y}^k| \quad (4.5)$$

$$\epsilon = \frac{n_0}{n_0 + n_{rep} - 1} \frac{n_0 + n_{rep} - 1}{n_0} \quad (4.6)$$

- \underline{y}^k = Best design
- \underline{y}^j = Worst design
- \underline{y}^c = Centroid design
- n_0 = Tuning parameter, normally 4 or 5
- n_{rep} = Number of iterations in a row where design #j has been the worst

4.5.1 Optimization result

The optimization of the system is divided into three main sections. First the controller parameters are evaluated dependent on different load cases and friction sizes. Secondly the response of the servo valve, and thirdly the parameters in the motion control valve are evaluated.

4.5.2 The controller

Initially the K_v parameter was optimized. K_v is the feed forward velocity gain (fig 4.7). This gain will be dependent on the specific load case. The load case in this model will be the friction force and the inertia. The inertia is based on a total weight of 23ton the additional maximum load capacity of the crane is 15ton. The K_v parameter was optimized for 15tons added load 7.5tons and no load (0ton). The three load cases are referred to as 100% 50% and 0% of the maximum capacity.

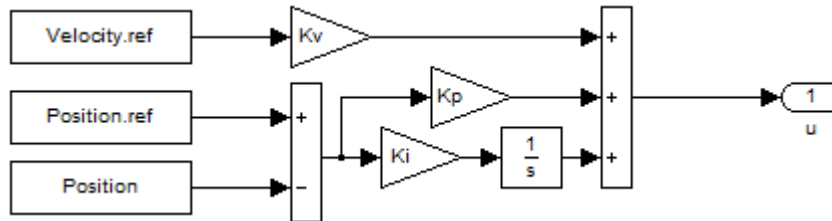


Figure 4.7: Block diagram of the controller

The three load cases resulted in three different K_v , but with a linear spacing (fig 4.8). The three obtained parameters were 0.00025, 0.00026, 0.00027. The parameter tend to increase linear with the load (fig 4.8).

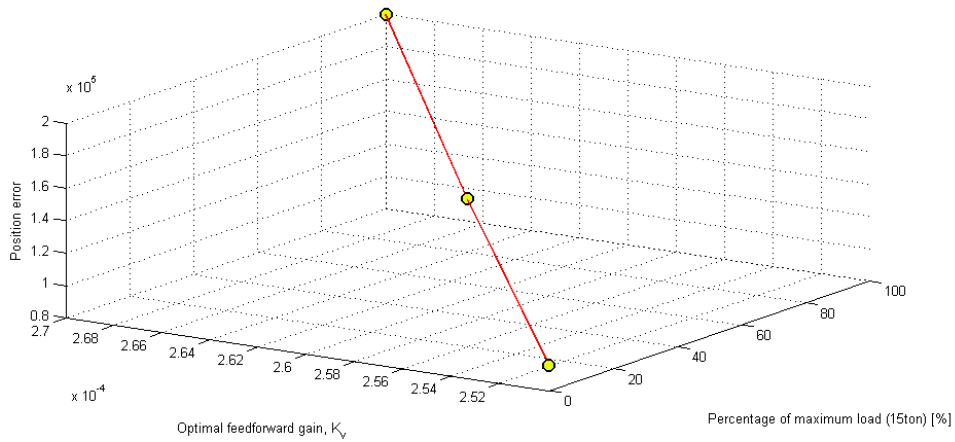


Figure 4.8: Optimized K_v , relative to position error and load

The optimization was performed on the other parameters in the controller (K_p , K_i , fig 4.7). The cost function used was only the C_{pos} to see how good accuracy was possible. The result of this has a clear potential for improvement and resulted in a relatively high position and velocity reference error(fig fig:opt5). Because of this a controller modification was performed followed by a parameter optimization.

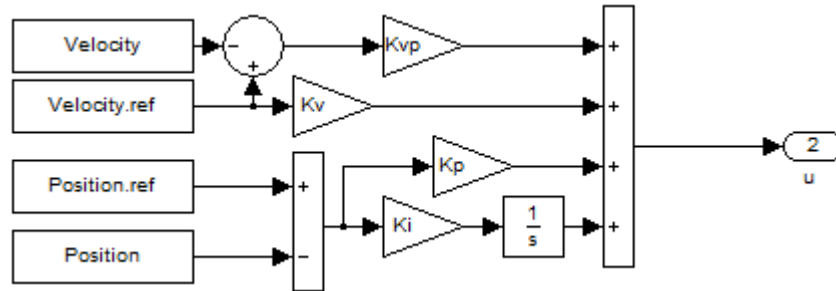


Figure 4.9: Modified controller

The modified (fig 4.9) has a proportional gain on the velocity, K_{vp} . The result of adding this parameter was fundamental and reduced the cost function, C_{pos} , with two-thirds of the original error.

	K_v	K_p	K_i	K_{vp}	C_{pos} , eq 4.1	Max pos error
0% load	0.00025	0.0106	0	NA	1869	6.1mm
	0.00025	0.0139	0.0048	0.000757	622	2.4mm
50% load	0.00026	0.0072	0	NA	3288	10.1mm
	0.00026	0.0157	0.0085	0.000907	640	3.0mm
100% load	0.00027	0.0077	0.0026	NA	4674	12.2mm
	0.00027	0.0186	0.0087	0.0020	672	3.3mm

Table 4.2: Optimized position parameters, for different load cases

A graphical comparison of the two optimized controllers is shown in figure 4.10. On the left the regular controller is used, and on the right the modified controller with a velocity error proportional gain is implemented. In the bottom of this figure there is two plots of the integrated error. These errors refers to the cost functions, equation 4.1 and 4.2. From these two plots one can easily see that the down side of using a proportional velocity error gain is an increase of high frequent noise in the oil (fig 4.11). The advantage is the improved accuracy which is revealed in the integrated position error (fig 4.10).

CHAPTER 4. OPTIMIZATION OF VPHS

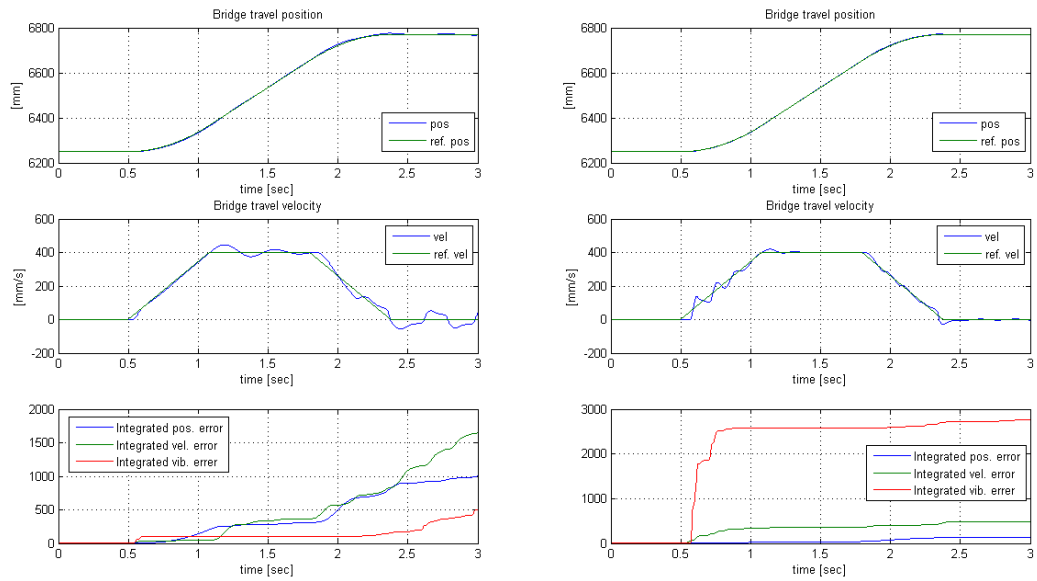


Figure 4.10: Comparison of position and velocity error with (right side) and without (left side) a controller with proportional velocity error gain.

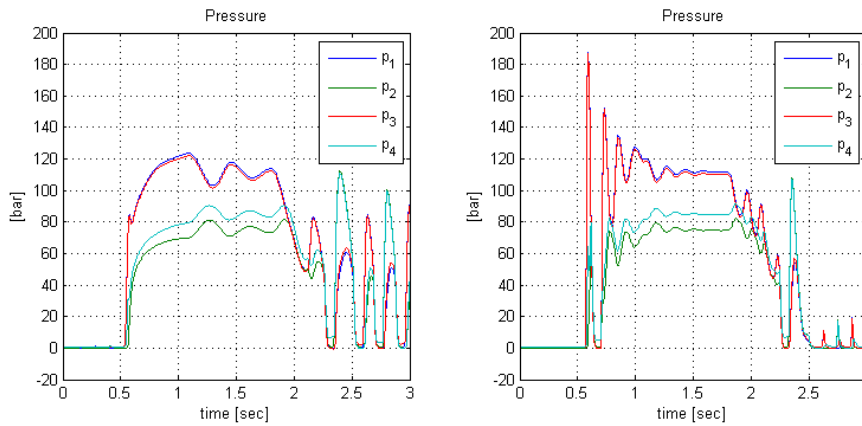


Figure 4.11: Comparison of the pressures with (right side) and without (left side) a controller with proportional velocity error gain.

By looking at the integrated position error one understand that the position are improving with the modified controller. To compare with the actual error and not the generated error by the defined cost function one can look at the figure 4.12. The figure show the maximum positioning error during the simulation period. The same parameters as in table 4.2 are use to generate the results.

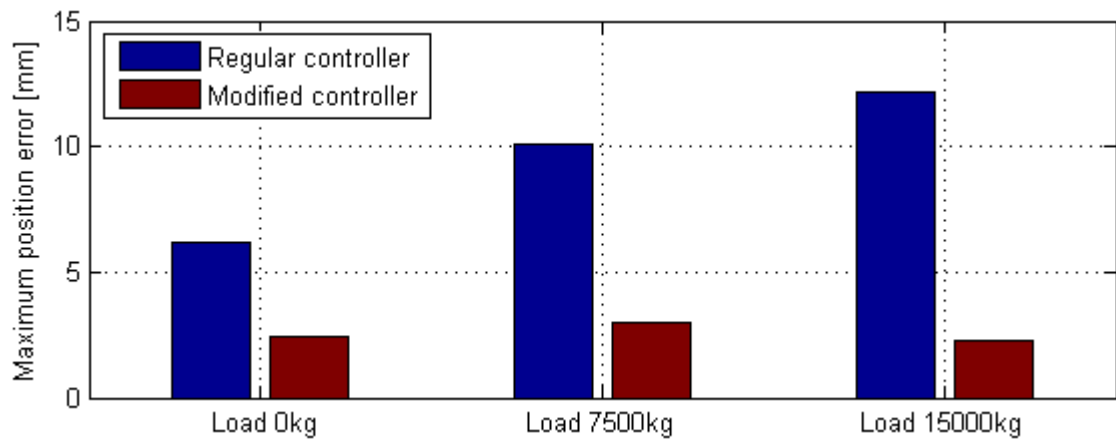


Figure 4.12: Max position error for each load case, with and without the modified controller.

To look at the effect of increased friction a viscous friction dependent on velocity was added. The friction is modeled as a rotational damper coupled to the output shaft of the motor. The results were compared with 4 different damper coefficients, C_d : $0Nm/[rad/s]$, $0.01Nm/[rad/s]$, $0.1Nm/[rad/s]$, and $1Nm/[rad/s]$. To get an image of the size of this friction the added friction moment is compared with the existing (fig 4.13).

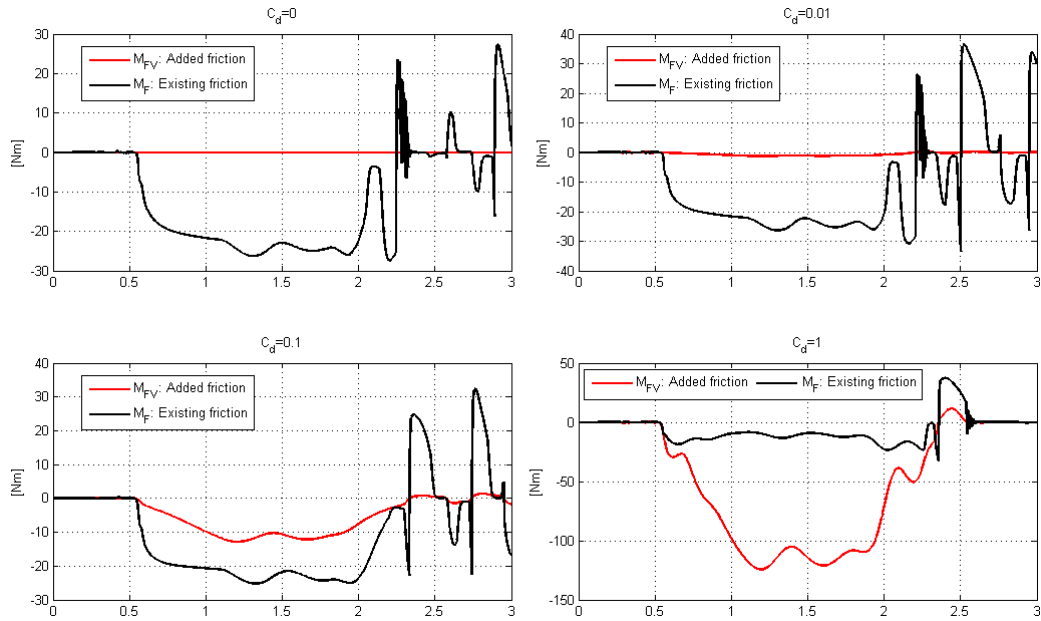


Figure 4.13: Friction moment during the simulation. The results are simulated with the parameters from table 4.3

The parameter optimization was performed with a load case of $7500kg$ and with the cost function dependent on position, C_{pos} (eq 4.1).

Case	C_d	K_v	K_p	K_i	$C_{vib}, eq4.2$	$C_{pos}, eq 4.1$
1	0	0.00026	0.0072	0	373	3288
2	0.01	0.000265	0.0083	0.0057	1097	2230
3	0.1	0.000309	0.0086	0.0153	659	2122
4	1	0.000820	0.0264	0	642	1946

Table 4.3: Optimized position parameters for different friction coefficients

4.5.3 The servo valve parameters

Because of the observed spool position error in the servo valve at high frequent changes in the spool position reference (fig 4.14), there is a reason to believe that the spool response frequency is affecting the position error.

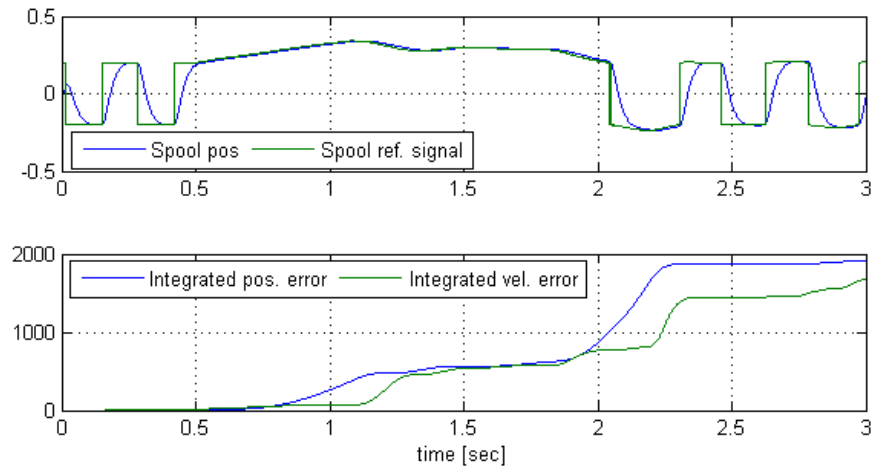
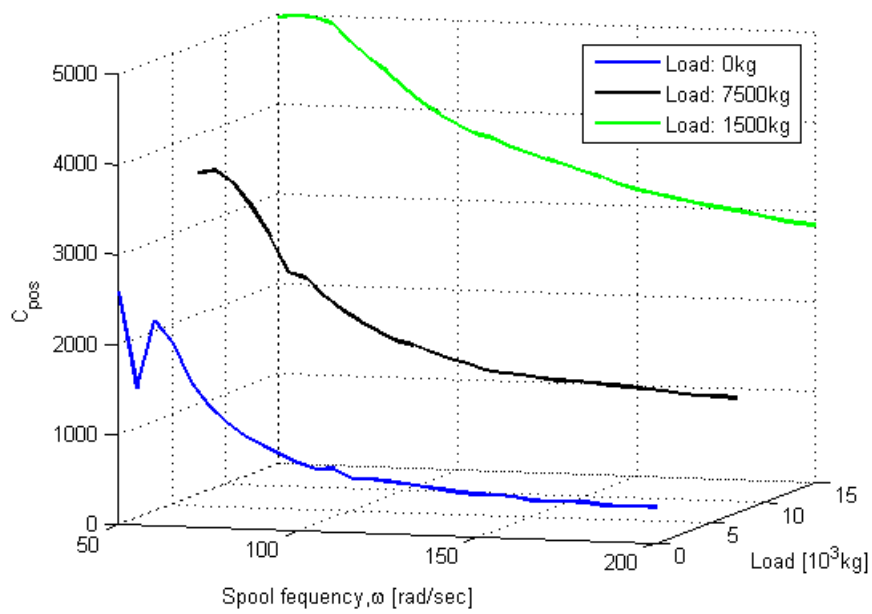


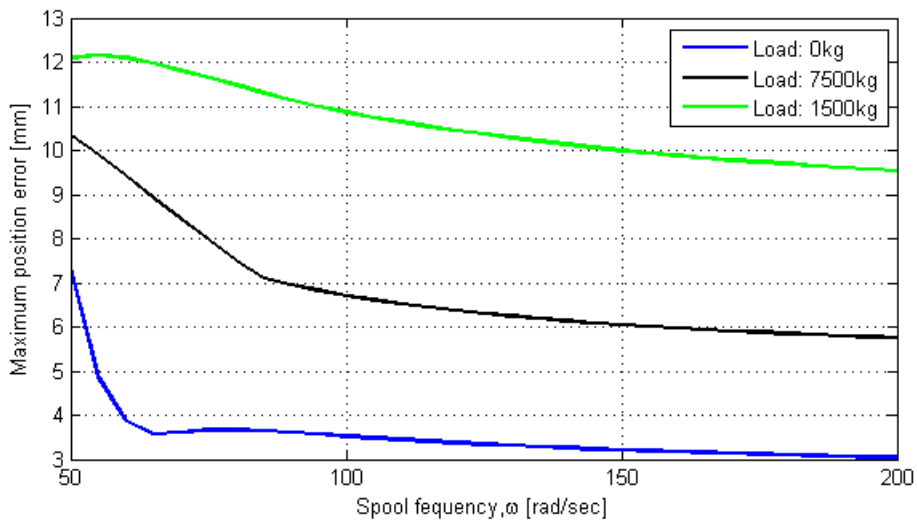
Figure 4.14: Spool position and the integrated error

The spool frequency response test was executed by simulate the system with a frequency increasing from $50rad/sec$ to $200rad/sec$. This was performed on the three different load cases (4.2) with a regular controller (no K_{vp}).

The test revealed that particularly at low load cases (0kg to 7500kg) an increased response frequency of the spool will improve the overall position error (4.15). For example one can see that for an increased spool frequency response from $50rad/sec$ to $75rad/sec$ the accuracy increases with 23% (Load: 7500kg fig 4.15b).



(a) Cost function error



(b) Position error

Figure 4.15: Results of spool response test.

4.5.4 The motion control valve parameters

To finally explore the effect of changing the pilot ratio and the spring stiffness of the spring in the motion control valve, a test with base from case 3 in table 4.3 was executed. In this test an optimization of the parameters P and K_s was performed. The optimization routine was conducted with 3 different cost functions. The three functions were based on the two cost functions in equation 4.1 and 4.2.

$$C_1 = C_{pos} \quad (4.7)$$

$$C_2 = C_{vib} \quad (4.8)$$

$$C_3 = C_{pos} + C_{vib} \quad (4.9)$$

This resulted in three different combinations of P and K_s (fig 4.16). The result shows that it is particularly important to include the position error/cost in the cost function for the optimization algorithm. If one compare the results for the optimization with cost function C_1 versus the C_2 , it is clearly shown that using a cost function only dependent of noise can be very misleading. The vibration cost function, C_{vib} , is reduced to 198, but the position cost function is increased to over 10000. The C_{vib} is lowered to a minimum of 198 which is over 50% lower than for the cost function C_1 . But since the position is out of bounds this result is not acceptable. What can be seen when the cost function C_3 is used is that both the C_{vib} and the C_{pos} is kept at a low level (table 4.4).

If one compares the base design which is case 3 (table 4.3) with the new design, one can see that the original design had a $C_{vib} = 659$ and a $C_{pos} = 2122$, while the new design with cost function C_3 has $C_{vib} = 219$ and $C_{pos} = 2035$.

Cost function	P	K_s	C_{vib}	C_{pos}
None	2.8	895	659	2122
C_1	3.0	868	322	1974
C_2	7.2	673	198	10353
C_3	3.4	855	219	2035

Table 4.4: Parameters obtained in optimization

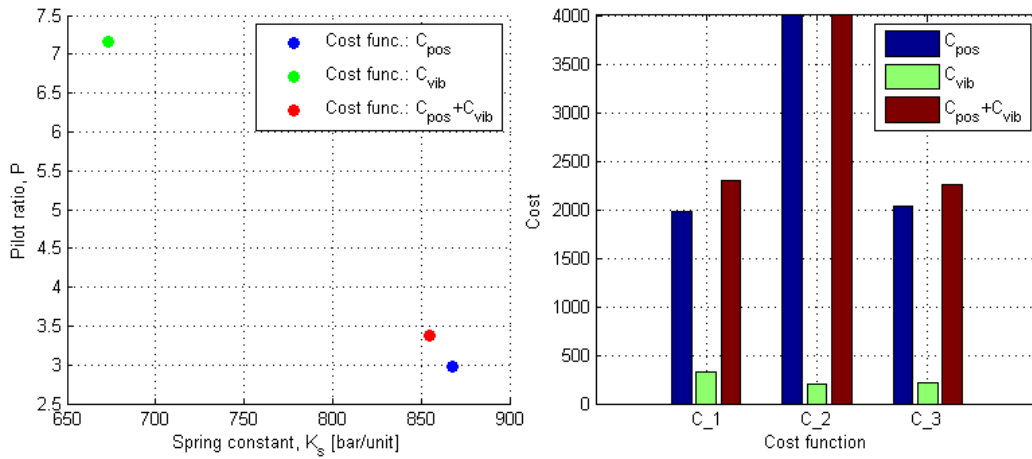


Figure 4.16: Optimized design of pilot ratio and spring stiffness.
 Note: the bars for the cost function, C_{vib} continues to a cost of 10353 and 10551.

You see from table 4.4 and figure 4.16 that both results with cost function C_1 and C_2 give a improved result in terms of high frequent vibrations (fig 4.17).

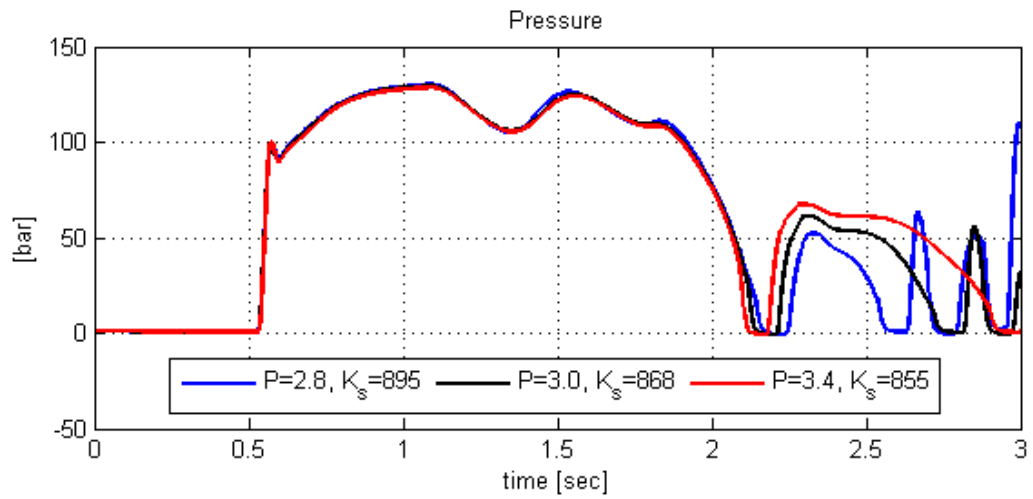


Figure 4.17: The effect of vibration reduction in the inlet pressure on the motor.

4.6 Sub-conclusions

Through this experiment it is shown that the accuracy (position error) is highly dependent on the controller parameters, and that the optimal controller parameters are dependent on the load case in form of inertia or friction. These discoveries points out a need for more a advanced controller. An alternative could be a controller with gain scheduling, where the gain is dependent on one or more observed variables. In this case the load could be this observed variable. If this is necessary or not is of coarse dependent on the necessity for high accuracy, or in other word the highest possible accuracy.

It was also shown that increasing the frequency response of the servo valve with 25% (from 52rad/sec to 75rad/sec) will increase the accuracy with about the same percentage. From this examination it was also revealed that increasing the frequency response above 100rad/sec would actually not improve the accuracy significantly. This means in a larger picture that it is not always beneficial to buy a more expensive and faster valve because it does not guarantee the system will increase its accuracy compared with the cost of upgrading the valve.

The regular controller of the existing system has a feed forward velocity reference and a PI controller acting on the position. A small modification of this controller revealed that adding a proportional velocity gain to the compensator can increase your accuracy with about 70%. It does assume that the velocity sensors has high resolution and is able to give a smooth signal to the controller. If this is possible it will be a very cheap and simple way to improve accuracy. A small downside of adding this term was a slight increase of noise in the system.

The parameter optimization of the motion control valve demonstrated that small adjustments in pilot ratio and spring stiffness will decrease the presence of noise and improve the accuracy slightly.

Conclusion

In this project a complete simulation model of the VPHS, containing the most important functionalities, has been developed. The complexity and simulation time is kept low by modeling the 3D machinery as several one dimensional sub systems. The components are built separately as modules and this makes it convenient to switch or change one single component without changing the complete model.

The motion control valves are identified as critical components and it is therefore important to use accurate models of these. To ensure an accurate model some experimental work was performed. This work revealed the importance of implementing flow forces to the model. The experimental work also verified the spool response, though with a low accuracy.

A model of the bridge travel drive line was customized for optimization purpose. Optimization with the so-called Complex algorithm and parameter variation was performed. This revealed opportunities and changes that could improve the accuracy of the pipe handler. The greatest opportunity for improvement lies in the controller. Implementing a velocity feedback and a proportional controller could increase the accuracy with roughly 70%. The current system only has a classical PI controller with a feedforward velocity gain. The optimization revealed that the optimal parameters change dependent on the load case. This implies that having

a classical controller with constant variables is not ideal in terms of accuracy. An alternative to the current constants could be to implement a gain scheduling. In this case the accuracy will improve without changing the controller states.

Parameter variation was performed on the response frequency of the directional servo valve. The current valve used on the bridge travel has a frequency of 8.3Hz. The parameter variation showed that an increase of the frequency will increase the accuracy until the frequency has reached 15Hz. Increasing the frequency above 16Hz gave negligible or small improvement in accuracy. For example, if the frequency response is increased from 8Hz to 12Hz the tool point accuracy increases with 23% and to 16Hz it increases with 35%, but from 8Hz to 20Hz the accuracy only increases with just 39% (data obtained from fig 4.15b load:7500kg). The figure 4.15b reveals that increasing the frequency above 16Hz has small impact on the toolpoint accuracy.

In this project the different components have been verified through experimental tests and/or with values and properties described in datasheets. The motion control valve VAA-B-SICN-ST-VF250, used in several operations on the bridge crane is verified through an experimental test. The experimental test was used to adapt and verify the simulation model. This resulted in a simulation model with high accuracy in terms crack pressure, spool opening and response. The different components were assembled to create the BC and LGA simulation model. With some experimental test results these models could be verified to obtain the desired accuracy. The models are proven to be used for optimization in terms of controller parameters, valve responses and motion control valve parameters.

The simulation model is modular. The different types of modules include motors, motion control valves, directional valves, inertias and friction forces. The advantage is that the different modules can be reused to create other systems containing the same components. In the future one could imagine that a library of accurate simulation sub models is established. Accurate simulation components give an opportunity to adjust controllers and components in a system to obtain the best possible result before physical testing. Since physical testing is a huge expense for the companies results from realistic simulation models are desired.

Bibliography

- [1] O. C. AS, “Technical data sheet, vaa-b-sicn-st-vf-250,” 1999.
- [2] S. Danfoss, “Pvg 32 proportional valve groups, technical information, catalogue,” 2011.
- [3] R. B. Group, “Servo solenoid valves with positive overlap and on-board electronics (obe), catalogue,” 2005.
- [4] M. R. Hansen, “Numerical optimization in practice (course ma417), lecture notes,” 2009.
- [5] M. R. H. Morten Kollerup Bak, “Modeling, performance testing and parameter identification of pressure compensated proportional directional control valves,” *Proceedings of the 7th FPNI Ph.D. Symposium on Fluid Power (to be published). Reggio Emilia, Italy*, 2012.
- [6] R. B. G. Oil Control, “Load holding - motion control, catalogue,” 2007.
- [7] Parker, “Hydraulic motor/pump series f11/f12, catalogue hy17-8249/us,” 2004.
- [8] —, “Measurement, control, regulation and automation, catalogue 4083-2/uk,” 2011.
- [9] A. Solution, “Songa eclipse, cbt, cd.”

Appendix **A**

Experimental test

A.1 intro

To verify the simulation model, a full scale test is done. This is done on a test rig in Kristiansand, with help from Morten Bak. First of all we had to choose measurement points that easily could be connected to the simulation model.

A.2 Measurement points

The vertical pipe handler system has already some measured signals that are used by the control system. These are signals like position and velocities of hydraulic cylinders and motors. These signals are relatively easy to observe, but to verify the model properly I need some additional measurement points.

These additional points are in the hydraulic system and can be sorted in two categories:

1. Pressure on each side of the motors and cylinders.

For example should one pressure transmitter be placed between 6a and 6b, in fig A.1. This pressure is important to log, because it says how much force

APPENDIX A. EXPERIMENTAL TEST

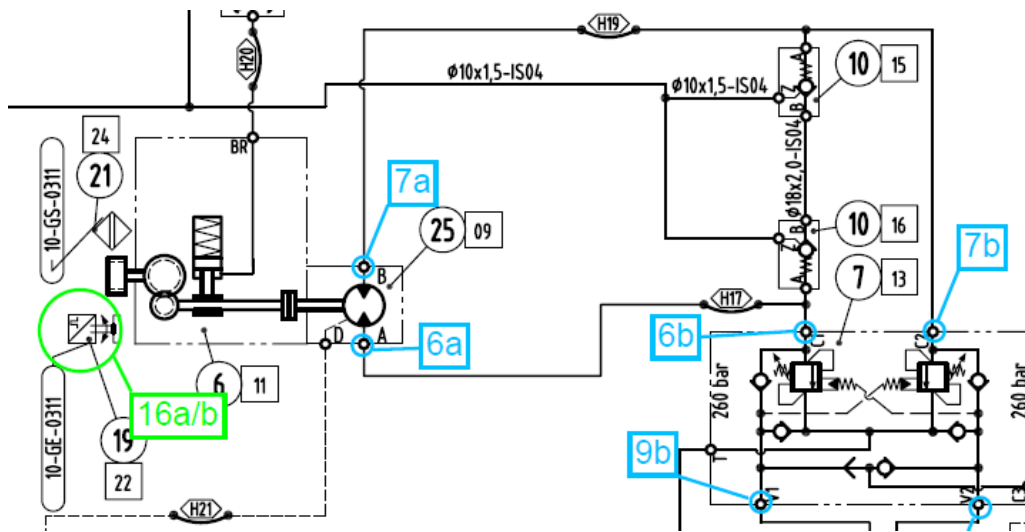


Figure A.1: Measurepoints

that is subjected to the motor. In this way I could use the data to see how much force that disappear in friction and energy losses, by comparing to the real accelerations of the trolley.

2. Pressure on each port between motion control valve and the directional valve.

These pressures are important when tuning the parameters in the simulated motion control valve. These pressures are also useful when the oil stiffness is determined.

A.3 Test procedure

This document is a procedure for experimental testing of the VPHS. The testing is a quantitative test with the purpose to measure and record data describing system behaviour that can be used to validate design calculations and simulation models.

A.3.1 Test Setup

In order to properly validate design calculations or simulation models of the crane, it is necessary to obtain measured data from the actual crane when performing operations identical to the ones from the calculations or simulations. More specifically three types of signals must be measured:

1. Input variables: control signals to hydraulic valves, and external loads (could be wind, or rigg axelerations)
2. State variables: hydraulic pressure, state signals from hydraulic valves, positions of actuators and moving parts.
3. Output variables: positions/velocities of controlled machine components. As in this case these signals are often also included in the state variables and here they are the signals from the various rotary encoders and position sensors.

APPENDIX A. EXPERIMENTAL TEST

Measure Points

The measure points on the bridge crane are described in the table below and in the appendix B.

MP	Signal	Description	Type	Unit	Measure Unit
1	pS	Supply pressure	State	Bar or MPa	
2	pA_BTM	A-port pressure, bridge travel motor	State	Bar or MPa	
3	pB_BTM	B-port pressure, bridge travel motor	State	Bar or MPa	
4	pA_BTC	A-port pressure, bridge travel control valve	State	Bar or MPa	
5	pB_BTC	B-port pressure, bridge travel control valve	State	Bar or MPa	
6	pA_TTM	A-port pressure, trolley travel motor	State	Bar or MPa	
7	pB_TTM	B-port pressure, trolley travel motor	State	Bar or MPa	
8	pA_TTC	A-port pressure, trolley travel control valve	State	Bar or MPa	
9	pB_TTC	B-port pressure, trolley travel control valve	State	Bar or MPa	
10	pA_SM	A-port pressure, slewing motor	State	Bar or MPa	
11	pB_SM	B-port pressure, slewing motor	State	Bar or MPa	
12	pA_SMC	A-port pressure, slewing control valve	State	Bar or MPa	
13	pB_SMC	B-port pressure, slewing control valve	State	Bar or MPa	
14a	s_BTM	Position, bridge travel motor	State	rad	
14b	v_BTM	Velocity, bridge travel motor	State	rad/sec	
15a	u_BTV	Command signal, bridge travel control valve	Input	%	
15b	s_BTV	Position, bridge travel control valve	State	%	
16a	s_TTM	Position, trolley travel motor	State	rad	
16b	v_TTM	Velocity, trolley travel motor	State	rad/sec	
17a	u_TTV	Command signal, bridge travel control valve	Input	%	
17b	s_TTV	Position, bridge travel control valve	State	%	
18a	s_SM	Position, slewing motor	State	rad	
18b	v_SM	Velocity, slewing motor	State	rad/sec	
19a	u_SV	Command signal, slewing control valve	Input	%	
19b	s_SV	Position, slewing control valve	State	%	

Table A.1: Measure points, bridge crane

APPENDIX A. EXPERIMENTAL TEST

For the lower guiding arm the logged states are:

MP	Signal	Description	Type	Unit	Mes. Uni
20	pS	Supply pressure, LGA	State	Bar or MPa	
21	pA_LBTM	A-port pressure, bridge travel motor LGA	State	Bar or MPa	
22	pB_LBTM	B-port pressure, bridge travel motor LGA	State	Bar or MPa	
23	pA_LBTC	A-port pressure, bridge travel control valve LGA	State	Bar or MPa	
24	pB_LBTC	B-port pressure, bridge travel control valve LGA	State	Bar or MPa	
25	pA_LSM	A-port pressure, slewing motor LGA	State	Bar or MPa	
26	pB_LSM	B-port pressure, slewing motor LGA	State	Bar or MPa	
27	pA_LSMC	A-port pressure, slewing control valve LGA	State	Bar or MPa	
28	pB_LSMC	B-port pressure, slewing control valve LGA	State	Bar or MPa	
29	pA_LJTC	A-port pressure, jib tilt cylinder LGA	State	Bar or MPa	
30	pB_LJTC	B-port pressure, jib tilt cylinder LGA	State	Bar or MPa	
31	pA_LTC	A-port pressure, telescope control valve LGA	State	Bar or MPa	
32	pB_LTC	B-port pressure, telescope control valve LGA	State	Bar or MPa	
33	pR_JTC	Rod-side pressure, jib tilt cylinder LGA	State	Bar or MPa	
34	pP_JTC	Piston-side pressure, jib tilt cylinder LGA	State	Bar or MPa	
35	pR_TC	Rod-side pressure, telescope cylinder LGA	Input	Bar or MPa	
36	pP_TC	Piston-side pressure, telescope cylinder LGA	Input	Bar or MPa	
37a	s_LBTM	Position, bridge travel motor LGA	State	rad	
37b	v_LBTM	Velocity, bridge travel motor LGA	State	rad/sec	
38	u_LBTV	Command signal, bridge travel control valve	Input	%	
39a	s_LSM	Position, slewing motor LGA	State	rad	
39b	v_LSM	Velocity, slewing motor LGA	State	rad/sec	
40	u_LJTV	Command signal, slewing motor	State	rad	
41	u_LTV	Command signal, telescope control valve LGA	Input	%	
42	u_LSV	Command signal, slewing control valve	Input	%	
43	s_JTC	Position, jib tilt cylinder	State	m	
44	s_TC	Position, telescope cylinder	State	m	

Table A.2: Measure points, lower guiding arm

APPENDIX A. EXPERIMENTAL TEST

This test was canceled by aker 21.02.2012. The test will probably be completed at a later stage.

Appendix **B**

Measurement points, Bridge crane

COMP ID NO	FUNCTIONAL DESCRIPTION
01	MAN CONTROL VLV, BRIDGE TRAVEL
02	BRIDGE TRAVEL MOTOR
03	BRIDGE TRAVEL MOTOR
04	BRIDGE TRAVEL REDUCTION GEAR
05	BRIDGE TRAVEL REDUCTION GEAR
06	HV BRIDGE TRAVEL
07	DCY RABAL BRIDGE TRAVEL
08	SP FOR DV MAN BRIDGE TRAVEL
09	SP FOR MAN VV BRIDGE TRAVEL
10	DN TRAVEL BRASS
11	DN TRAVEL BRASS
12	BRAKE RELEASE SHUTTLE
13	DP MAN PRESSURE
14	DP MAN PRESSURE
15	DP BRAKE RELEASE - BRIDGE TRAVEL
16	BRIDGE TRAVEL - BRACK BRACK FALL
17	BR TRAVEL - BRACK OWN INTERFACE EXT
18	SPEED AND POSITION SENSOR
19	SPEED AND POSITION SENSOR RESET
20	ANTIPLANTATION - BRIDGE TRAVEL

This document and all information and data obtained herein or hereafter are the confidential and proprietary property of Aker MH AS and are not to be used, reproduced or disclosed in whole or in part by or to anyone without the written permission of Aker MH AS.

THIS IS A COMPUTER AIDED DRAWING AND MUST NOT BE ALTERED MANUALLY

Tolerances except as noted: Welding and Materials except as noted:

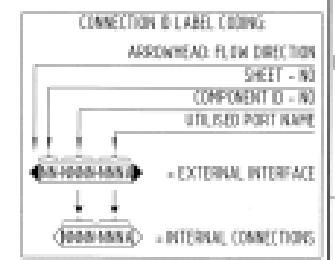
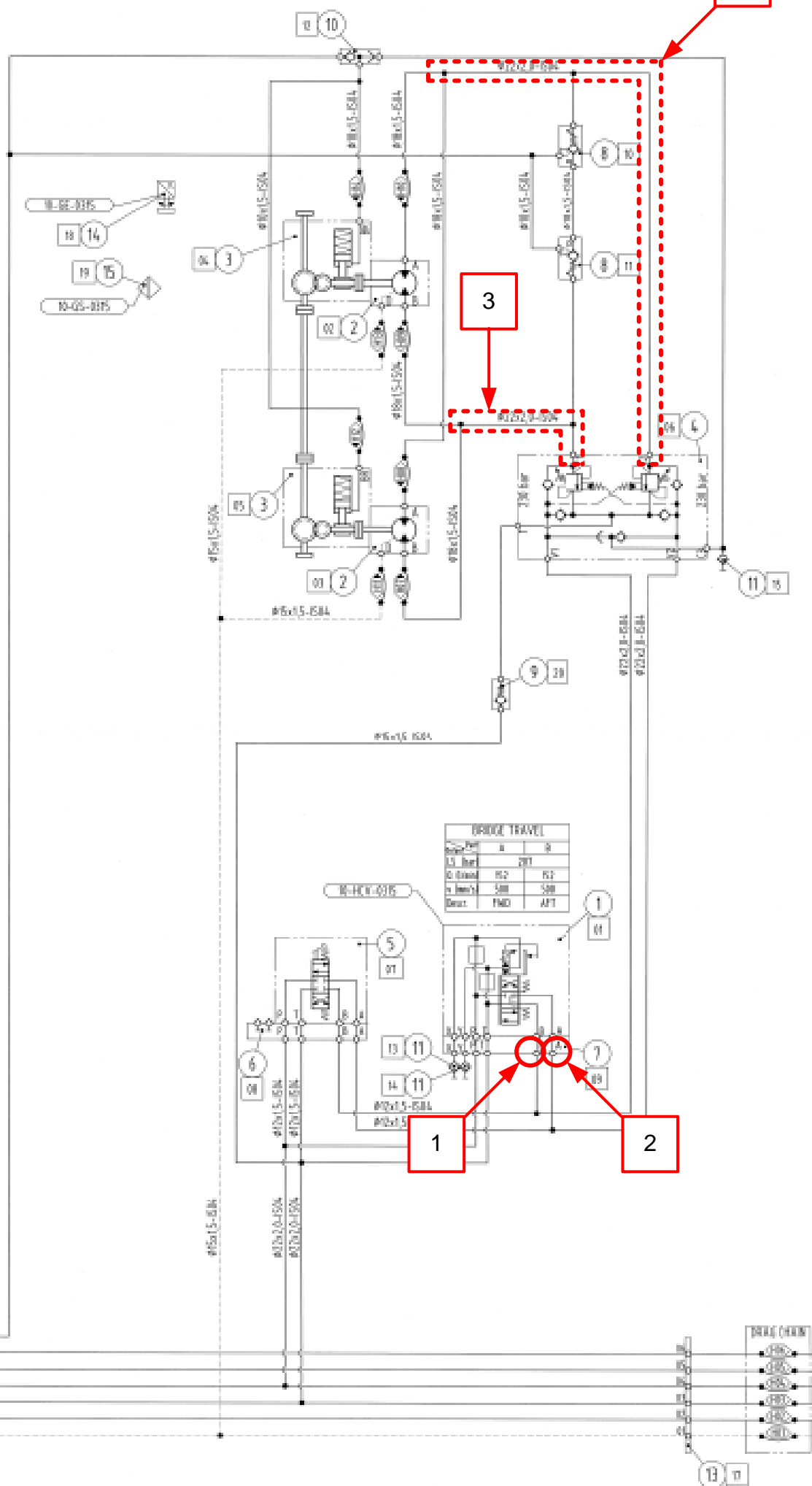
Rev.	Description of revision	Des.	Appr.	Date / Sgn.
01	ISSUED FOR CONSTRUCTION			15-DEC-19

NOTE!

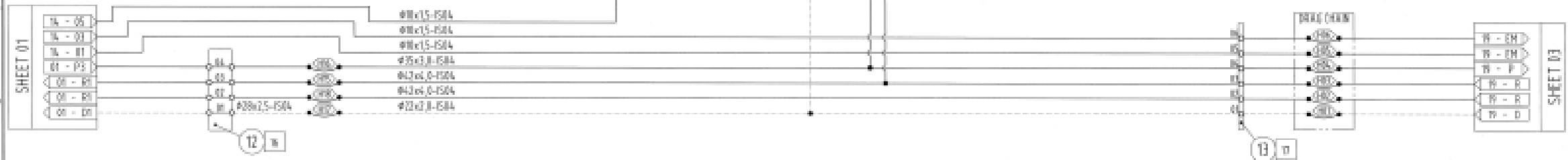
HYDRAULIC TUBE / PIPE / FITTING / FLANGE
 PROPERTIES ACC. TO MH STD. PIPING SPECIFICATION, SA17-001
 TUBE / PIPE DIMENSION / PIPING CLASS SHEET ACC. TO FLOW DIAGRAM.

PRESSURE FLUID
 HYDRAULIC MINERAL OIL ISO HV TYPE (DIN HVLPI)
 PERMISSIBLE UPPER OPERATIONAL CONTAMINATION LIMIT
 TO BE APPROVED ACCORDING TO ONE OF THE FOLLOWING STANDARDS:
 ISO 4406, CODE - / 15 / 13 BR
 SAE AS 4059, REV. E, TABLE 2, CLASS 78-F OR
 SAE AS 4059, REV. E, TABLE 1, CLASS 1

GRAPHICAL SYMBOLS
 BASED ON ISO 1219 AND EN 6017-2

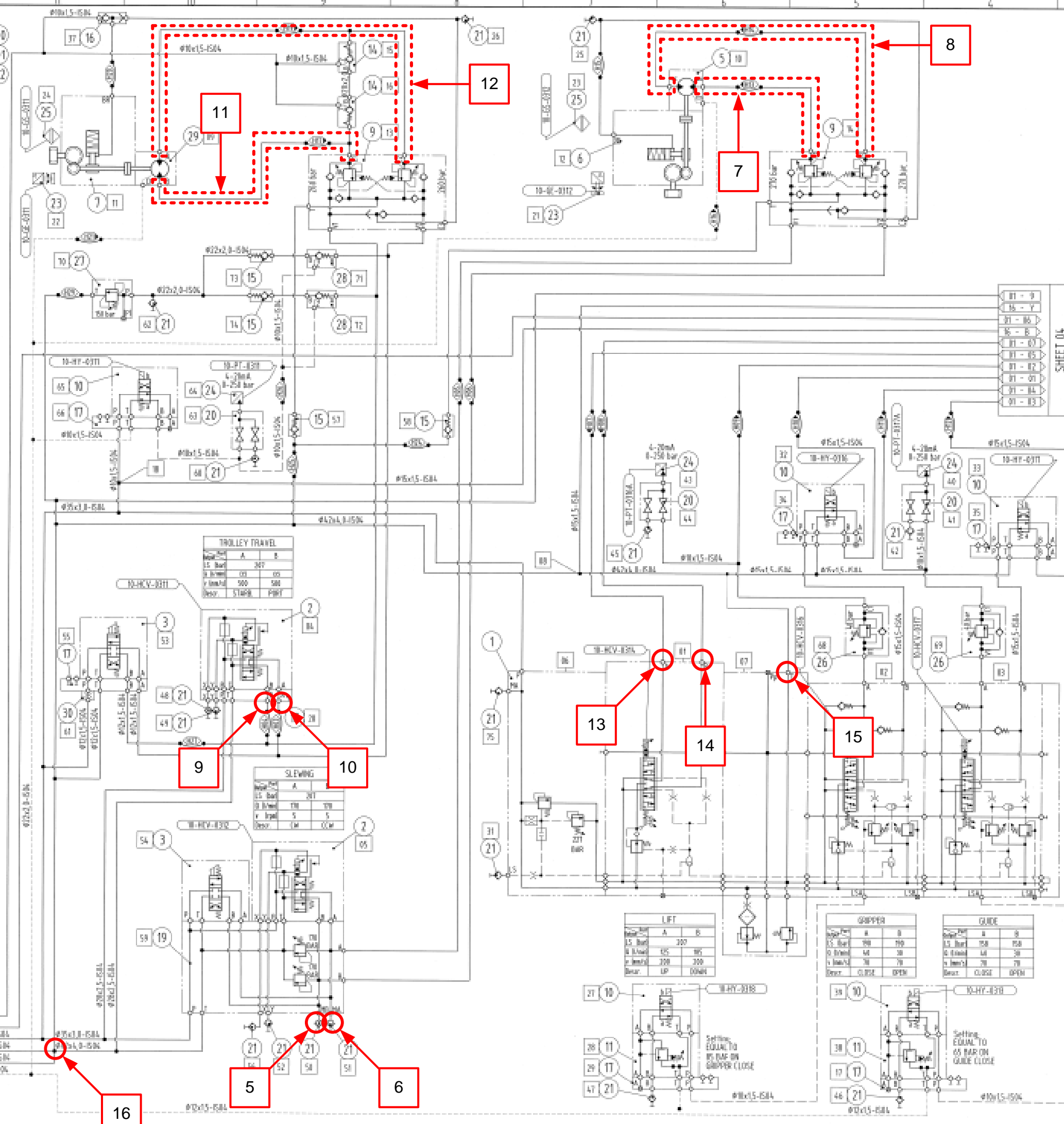


QTY	ITEM	DESCRIPTION	DRUG/MATERIAL	UNIT WEIGHT	PART NUMBER
1	00	COMPONENT ID NUMBER	MH 1312313, RANGE: 02-01 TO 02-25		63595
1	11	HOSE KIT - ISO2151-2/3	BA0078628-B001-BRIDGE TRAVEL		78628
1	16	HOSE KIT - ISO2151-2/3	BA0078625-B001-DRAG TRAVEL		78625
1	15	SENSOR W/YS MTR. CABLE (10x20)	NCB10-30-OM-4.0-10		27176
1	14	ROTARY ENCODER INTEGRATED	10 5P20M, PROFINET-OP		55860
1	13	MANIFOLD UNDER PLATE	PH 1846445		11111
1	12	MANIFOLD	PH 5125814 - PH 5125814		11111
3	11	TEST COUPLING W/BALL W/6x3/8x1/4	1-91-29-12-BTL		17991
1	10	SHUTTLE VALVE	HFDK 32-14-25-R 1/4"		10329
1	9	CHECK VALVE	RHD1/2" A3C 1/5 BAR		19580
2	8	CHECK VALVE PILOT	RH 1/2-1/2" HWP4100103		10108
1	7	SUB PLATE	0 17A/1 (BR426418)		60230
1	6	SUB PLATE COTOP BS	0212011		43689
1	5	DIRECTIONAL VALVE, INHOFF, MAN OPERATED	04-011 (S14014)		21921
1	4	MOTION CONTROL VALVE	NAA-B-30M-ST-VP 254-15,11,45-19-05-35		18857
2	3	SEM ENDRIVE GEAR W/REDUCTION BRAKE	K 171A-B 31311-010 798-25-080		61045
2	2	HYDRAULIC MOTOR, VOAC SAE B	FD-838-15-SV-S		30374
1	1	PROPORS, PROPORTIONAL DIRECTIONAL VALVE	14WRE 16 NZ1851-31/32/42/50/60/80/100/140-		62624



COMP ID	FUNCTIONAL DESCRIPTION
01-01	MAIN CONTROL VALVE
02	MAIN CONTROL VALVE TRIPLE TRAY
03	MAIN CONTROL VALVE SLEWING
04	MAIN CONTROL VALVE BELT MODULE
05	MAIN CONTROL VALVE TARM MODULE
06	TIE CONNECTION FOR RETURN LINE
07	PRIOR TRIPLE TRAY
08	MOTOR SLEWING
09	REGULAR TRIPLE TRAY
10	REGULAR SLEWING
11	REV TRIPLE TRAY
12	REV SLEWING
13	DM TRAVEL BYPASS
14	DM TRAVEL BYPASS
15	SP LOW FORCE LIMIT
16	TIE CONNECTION FOR PRESSURE LINE
17	DRAG CHAIN TROLLEY INTERFACE
18	SP MAIN CONTROL VALVE TRIPLE TRAY
19	SPEED/POSITION SENSOR SLEWING
20	SPEED/POSITION SENSOR TROLLEY
21	SLEWING OBJECT SENSOR
22	TROLLEY TRAVEL RESET SENSOR
23	TP BRAKE RELEASE SLEWING
24	TP BRAKE RELEASE TROLLEY TRAY
25	TP BRP FORCE
26	LOW FORCE LIMIT
27	SP LOW FORCE LIMIT
28	TP LS PRESSURE
29	ENABLE CRIP OPEN
30	ENABLE CRIB OPEN
31	TP GYR PRESSURE
32	TP GYR PRESSURE
33	GYR PRESSURE TRANSMITTER
34	DM CRIB PRESSURE
35	TP CRIB PRESSURE
36	DM CRIB PRESSURE TRANSMITTER
37	DM CRIB PRESSURE
38	TP HIGH PRESSURE ACTIVE GUIDE
39	TP HIGH PRESSURE ACTIVE SPP
40	TP SUPPLY PRESSURE
41	TP TARM PRESSURE
42	TP LS PRESSURE
43	TP RETURN PRESSURE
44	DM MAIN ACTUATOR TROLLEY TRAY
45	DM MAIN ACTUATOR SLEWING
46	SP FOR DM MAIN ACTUATOR TROLLEY
47	TP SUPPLY PRESSURE
48	ANTI-COLLISION TROLLEY TRAY
49	ANTI-COLLISION TROLLEY SLEWING
50	MANIPUL BLOCK
51	TP REDUCED FORCE ENABLED
52	SP/LS REDUCED FORCE
53	TP MAX FORCE PRESSURE
54	DM FOR PRESSURE TRANSMITTER
55	PT REDUCED FORCE ENABLED
56	DM FOR REDUCED FORCE DM/TP
57	HOISTING PLATE FOR DM
58	DM/TP PRESSURE TRANSMITTER
59	DM/TP PRESSURE TRANSMITTER
60	MAX FORCE LIMIT HOISTING PLATE
61	ENABLE REDUCED FORCE A-RUN
62	ENABLE REDUCED FORCE B-RUN
63	A-RUN ISOLATE VALVE
64	B-RUN ISOLATE VALVE
65	TP MAIN PRESSURE

COMP ID	FUNCTIONAL DESCRIPTION
66	TP MAIN PRESSURE
67	TP MAIN PRESSURE
68	TP MAIN PRESSURE
69	TP MAIN PRESSURE
70	TP MAIN PRESSURE
71	TP MAIN PRESSURE
72	TP MAIN PRESSURE
73	TP MAIN PRESSURE
74	TP MAIN PRESSURE
75	TP MAIN PRESSURE
76	TP MAIN PRESSURE
77	TP MAIN PRESSURE
78	TP MAIN PRESSURE
79	TP MAIN PRESSURE
80	TP MAIN PRESSURE
81	TP MAIN PRESSURE
82	TP MAIN PRESSURE
83	TP MAIN PRESSURE
84	TP MAIN PRESSURE
85	TP MAIN PRESSURE
86	TP MAIN PRESSURE
87	TP MAIN PRESSURE
88	TP MAIN PRESSURE
89	TP MAIN PRESSURE
90	TP MAIN PRESSURE
91	TP MAIN PRESSURE
92	TP MAIN PRESSURE
93	TP MAIN PRESSURE
94	TP MAIN PRESSURE
95	TP MAIN PRESSURE
96	TP MAIN PRESSURE
97	TP MAIN PRESSURE
98	TP MAIN PRESSURE
99	TP MAIN PRESSURE
100	TP MAIN PRESSURE
101	TP MAIN PRESSURE
102	TP MAIN PRESSURE



This document and all information and data disclosed herein or hereafter are the confidential and proprietary property of Aker MH AS and are not to be used, reproduced or disclosed in whole or in part by or to anyone without the written permission of Aker MH AS.

THIS IS A COMPUTER AIDED DRAWING AND MUST NOT BE ALTERED MANUALLY

Tolerances except as noted: Welding and Materials except as noted.

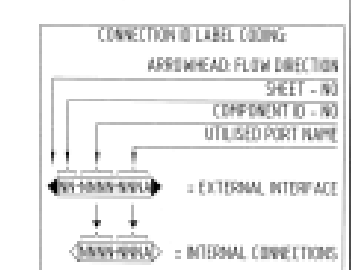
Rev.	Description of revision	Date	App.	Date / App.
01	ISSUED FOR CONSTRUCTION	19/08/20	NA	26-OCT-2019/AN

NOTE:

HYDRAULIC TUBE / PIPE / FITTING / FLANGE:
 PROPERTIES ACC. TO MH STD. PIPING SPECIFICATION, 5410-1001
 TUBE / PIPE DIMENSION / PIPING CLASS SHEET ACC. TO FLOW DIAGRAM

PRESSURE FLUID:
 HYDRAULIC MINERAL OIL ISO HV TYPE (DIN HVP1)
 PERMISSIBLE UPPER OPERATIONAL CONTAMINATION LIMIT
 TO BE APPROVED ACCORDING TO ONE OF THE FOLLOWING STANDARDS:
 ISO 4406, CODE - / 15 / 13 OR
 SAE AS 4059, REV. E, TABLE 2, CLASS TB-F OR
 SAE AS 4059, REV. E, TABLE 1, CLASS 7

GRAPHICAL SYMBOLS:
 BASED ON ISO 1219 AND EN 6047-2



Item	Comp. ID	Description	Part Number	Qty
1	02	COMPONENT ID NUMBER	MH 1312313, RANGE: 03-51 TO 03-75	6251
1	01	COMPONENT ID NUMBER	MH 1312313, RANGE: 03-26 TO 03-50	6250
1	00	COMPONENT ID NUMBER	MH 1312313, RANGE: 03-01 TO 03-25	6249
1	31	HOSE KIT -ISO1219-2/3	BAB01841-B001-CV0	18641
1	30	FRED THROTTLE ADAPTER, G 3/8, #18	DP 108800	54812
1	29	HYDRAULIC MOTOR, VQAC SAE B	PT-030-M5-SV-S	20374
2	28	HYDR PILOT OPERATED CHECK VALVE	RH 4 04W9400041	12238
1	27	PRESSURE RELIEF VALVE, PIPE MOUNTED	0005 21 00V/375 R99A241041	10182
2	26	SEQUENCE VALVE	W50-CC-39-05 Z11-03-02-05	24350
2	25	SENSOR W/TS MTR. CABLE (106283)	WCB10-30-QH-43-40	27706
3	24	PRESS TRANSMITTER W/TS MTR CABLE	PTX134 - PTX 23+PTX130EX 250 BAR	58109
2	23	ROTARY ENCODER INTEGRATED	01 59208, PROFINET-IP	55861
1	22	MANIFOLD	MH 511124	11111
16	21	TEST COUPLING W/BALL MN42/01/4	1-112-29-12-070	11992
3	20	BLOCK & BLEED VALVE, 2 VALVE MANIFOLD	HAL 574VRR1P-MH-306, W/ESP 1/4" THREAD	31972
1	19	VALVE BLOCK NO. 6	R 98720019 - R98A24369	58355
1	18	SUB PLATE	G 174/1 BR042413	10291
6	17	SUB PLATE CETOP 03	E210101	43509
1	16	SHUTTLE VALVE	HROK 23-1A-25-R 1/4"	11328
4	15	CHECK VALVE	RH01/2" A3C 0.5 BAR	19581
2	14	CHECK VALVE/PILOT	RH 03-1/2" 04W940003	10196
2	11	PRESSURE RELIEF VALVE, SANDWICH	Z0B 04VA2-4 X 200V (R9004 09886)	11631
5	10	4/3 DR. VALVE, 6 POSITION, 0.5" x 0.5"	DNA-063V2-H 240C	48964
3	9	MOTION CONTROL VALVE	VAR-B-S0N-ST-VF350-05,7145-W-05-35	10871
1	7	SLEW GEARBOX	RES12-02, R-384, H-R, Z-11	54892
1	6	SLEW GEARBOX	RES12-11, R-444, H-R, Z-11	58382
1	5	HYDRAULIC MOTOR, HOAC SAE C, 4 HOLES	PT-060-M5-SH-S	20385
2	3	DIRECTIONAL VALVE, 6WAY, MH OPERATED	DB-0111 (4/3/0/4)	21961
2	2	BRASS, PROPORTIONAL DIRECTIONAL VALVE	WVLE 1/4" W21051-D/024110VA/01010A+	62624
1	1	PROP. VALVE-B08-LIFT-GRIPPER-GUIDE	PV0 12M/32 T184405	65828

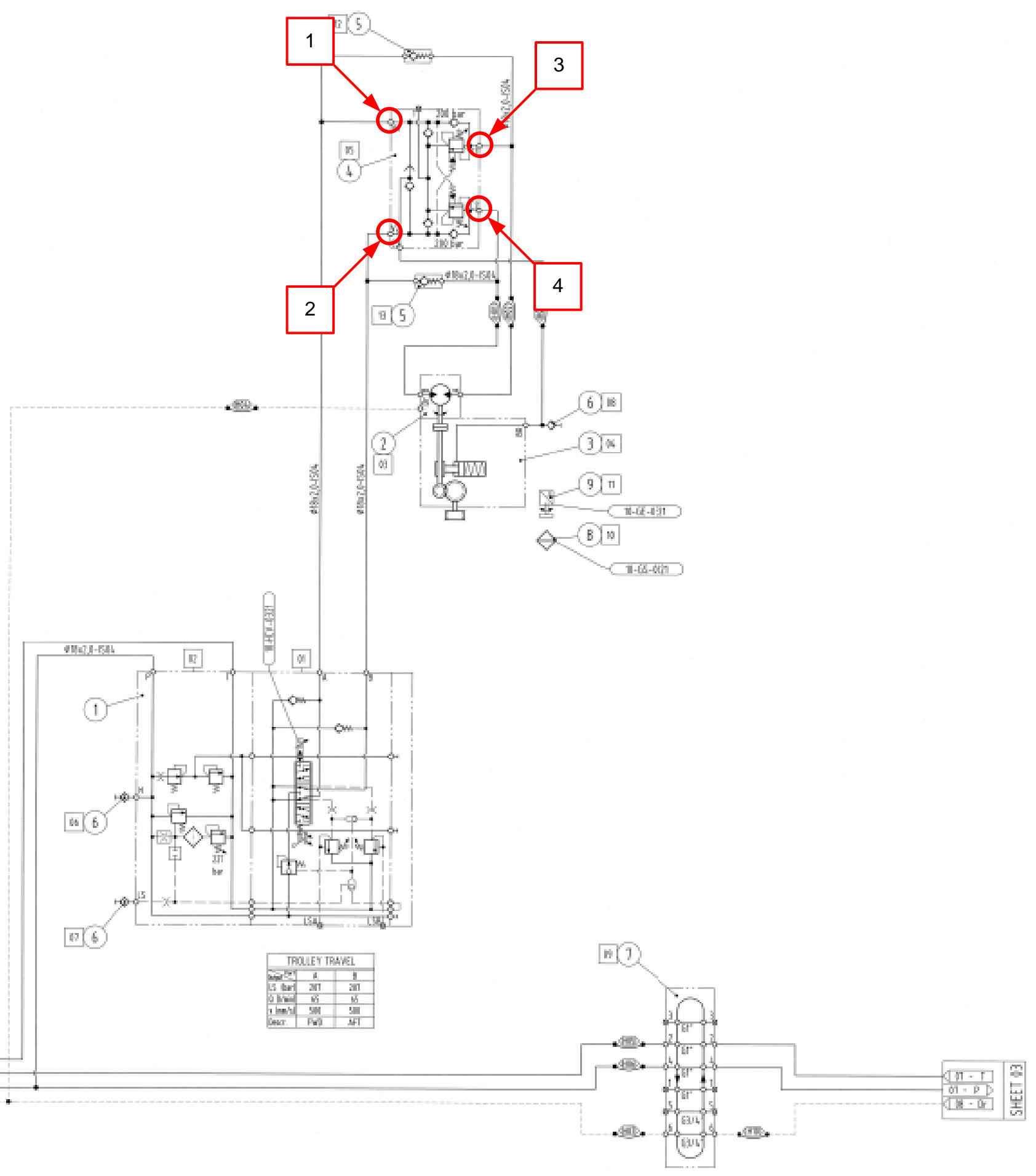
Date	Drawn	Checked	Scale	Project	Part number
26-JUN-18	151	NA	NA	BC01 BRIDGE CRANE TYPE 1942269	CVU, TROLLEY TRAVEL & SLEW HYDRAULIC FLOW DIAGRAM, SHEET 03

Appendix **C**

Measurement points, Lower guiding
arm

COMP ID/REV	FUNCTIONAL DESCRIPTION
01	RAIL CONTROL VALVE
02	RAIL CONTROL VALVE INLET HOBBLE
03	TROLLEY MOTOR
04	ROCKARM FWD TROLLEY MOTOR
05	RCH TROLLEY FWD/REV
06	TP SUPPLY PRESSURE
07	TP LS PRESSURE
08	TP BEARY RELEASE PRESS TROLLEY
09	SWHBL LEMOTION
10	TRAVEL RESET SENSOR
11	POSITION SENSOR
12	REDUSE PRESS DROP FWD
13	REDUSE PRESS DROP AFT

104



Comp ID	A	B
US Bar	201	201
KG/cm ²	15	15
PSI	290	290
Desc.	Fwd	Rev

This document and all information and data disclosed herein or hereafter are the confidential and proprietary property of Aker MH AS and are not to be used, reproduced or disclosed in whole or in part by or to anyone without the written permission of Aker MH AS.

THIS IS A COMPUTER AIDED DRAWING AND MUST NOT BE ALTERED MANUALLY

Tolerances except as noted: Welding and Materials except as noted:

DATE ISSUED BY: _____

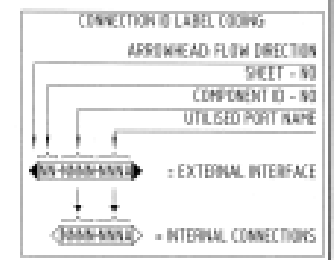
Rev	Description of revision	Des.	Appr.	Date / Sign.
01	ISSUED FOR CONSTRUCTION	U. [Signature]	[Signature]	24-SEP-10 WAKA

NOTE!

HYDRAULIC TUBE / PIPE / FITTING / FLANGE:
 PROPERTIES ACC. TO PH STD. PIPING SPECIFICATION, SA11-8011
 TUBE / PIPE DIMENSION / PIPING CLASS SHEET ACC. TO FLOW DIAGRAM

PRESSURE FLUID:
 HYDRAULIC MINERAL OIL ISO HV TYPE (DMHVL)
 PERMISSIBLE UPPER OPERATIONAL CONTAMINATION LIMIT TO BE APPROVED ACCORDING TO ONE OF THE FOLLOWING STANDARDS:
 ISO 4406, CODE - / IS / IS OR
 SAE AS 4059, REV. E, TABLE 2, CLASS 10-F OR
 SAE AS 4059, REV. E, TABLE 1, CLASS 1

GRAPHICAL SYMBOLS:
 BASED ON ISO 1219 AND EN 60617-2



COMP ID/REV	DESCRIPTION	PH 1372313 RANGE: 02-01 TO 02-25	QTY	UNIT WEIGHT	PART NUMBER
1 00	COMPONENT ID NUMBER	PH 1372313 RANGE: 02-01 TO 02-25	6265		
1 10	ROSE KIT - ISO2701-2/3	BA076204-002-TROLLEY	16206		
1 9	ROTARY ENCODER INTEGRATED	10591208, PROFBUS-OP	52061		
1 8	SENSOR W/5 MTR. CABLE (0M203)	NO30-38-0H-10-00	2106		
1 7	HYDRAULIC END SWHBL	B100-06, 2X3/4" +4XT, INDUSTRY	42625		
3 6	TEST COUPLING W/BALL MN+2/16AA	1-90-20-12-010	1093		
2 5	CHECK VALVE	RH03/4" AIC 2,0 BAR	10638		
1 4	MOTION CONTROL VALVE	VAA-0-S0R-S1-10050-05 7145-37-02-20	24990		
1 3	SLEN GEARBOX	REN2-01, R1, R1, M4, Z-14	54001		
1 2	HYDRAULIC MOTOR, YOAC SAE B	P11-019-M0-SH-S	20027		
1 1	PROP.VALVE-002-TROLLEY TRAVEL	PVG 31 T050477	60293		
Qty	Rev	Description	Drwg./Material	Unit weight	Part number
Date	Drawn	Traced	Scale		
24-JUN-10	TSR	AKA	NA		
Checked	Approved	Projection			
[Signature]	[Signature]	[Symbol]			
BC02 LOWER GUIDING ARM TYPE 1922136			Project no.	Replaced by	
TROLLEY			Format	Drwg. number	Rev.
HYDRAULIC FLOW DIAGRAM, SHEET 02			A1	1921314	01



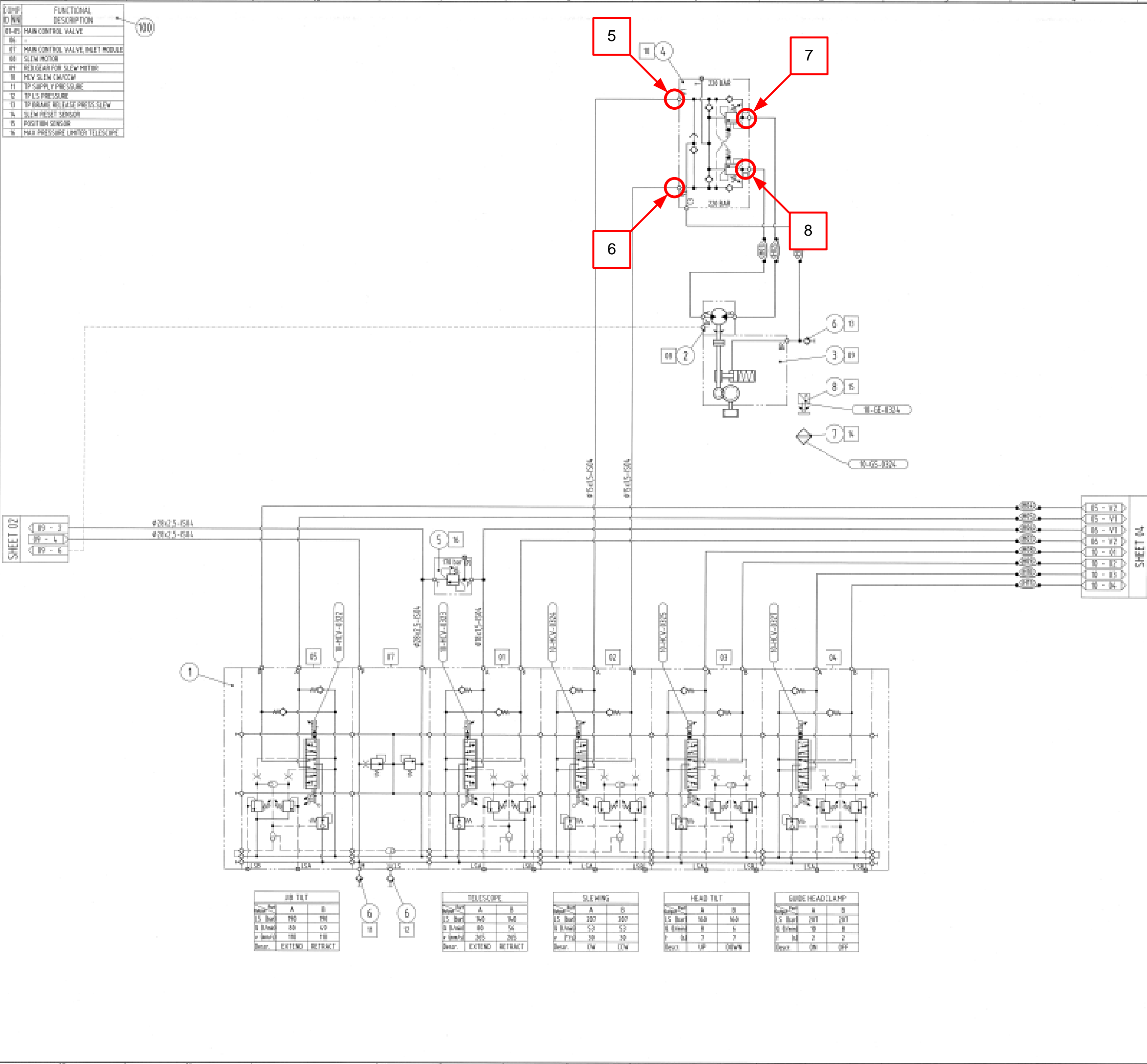
This document and all information and data disclosed herein or hereafter are the confidential and proprietary property of Aker MH AS and are not to be used, reproduced or disclosed in whole or in part by or to anyone without the written permission of Aker MH AS

THIS IS A COMPUTER AIDED DRAWING AND MUST NOT BE ALTERED MANUALLY

Tolerances except as noted: Milling and Materials except as noted

Rev.	Description of revision	Doc.	App.	Date / Sig.
01	ISSUED FOR CONSTRUCTION	1/16/20	SM	26-SEP-19/AMA

COMP ID / NO	FUNCTIONAL DESCRIPTION
01-05	MAIN CONTROL VALVE
06	-
07	MAIN CONTROL VALVE, INLET MODULE
08	SLEW MOTOR
09	REVERSE GEAR FOR SLEW MOTOR
10	REV SLEW MOTOR
11	TP SUPPLY PRESSURE
12	TP LS PRESSURE
13	TP DRUM NO. 1 (A) PRESSURE
14	SLEW PRESS. SENSOR
15	POSITION SENSOR
16	TRAIL PRESSURE LIMITER TELESCOPE

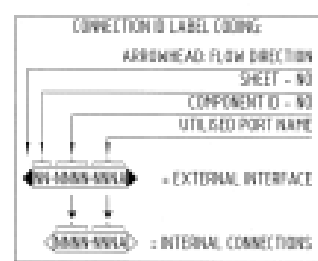


NOTE!

HYDRAULIC TUBE / PIPE / FITTING / FLANGE:
 PROPERTIES ACC. TO MH STD. PIPING SPECIFICATION, SA17-001
 TUBE / PIPE DIMENSION / PIPING CLASS SHEET ACC. TO FLOW DIAGRAM

PRESSURE FLUID:
 HYDRAULIC MINERAL OIL ISO HV TYPE (DM HVLFI)
 PERMISSIBLE UPPER OPERATIONAL CONTAMINATION LIMIT
 TO BE APPROVED ACCORDING TO ONE OF THE FOLLOWING STANDARDS:
 ISO 4406, CODE - / 5 / 10-00
 SAE AS 4059, REV. E, TABLE 2, CLASS 7 B-F OR
 SAE AS 4059, REV. E, TABLE 1, CLASS 1

GRAPHICAL SYMBOLS:
 BASED ON ISO 1219 AND EN 60717-2



COMP ID	NO	COMPONENT ID NUMBER	DESCRIPTION	QTY	UNIT	WEIGHT
1	06	MH 1372313	RANGE: 03-01 TO 03-25	63509		
1	09	BA0876287-8C02-CVU & SLEWING		76287		
1	08	ID 591288, PROFIBUS-DP		55861		
1	07	NO10-38-0M-10-NO		2706		
3	06	1-90-29-12-000		1893		
1	05	0805 75 008/280 (R00824)M03		25374		
1	04	VAA-8-S08-ST-VP58-05 7145-B-01-35		28077		
1	03	RES0-02, R=384, M=10, Z=7		54682		
1	02	PI2-018-MS-SV-S		20374		
1	01	PAG 32 11858473		63232		

Qty	Item	Description	Drawg./Material	Unit weight	Part number

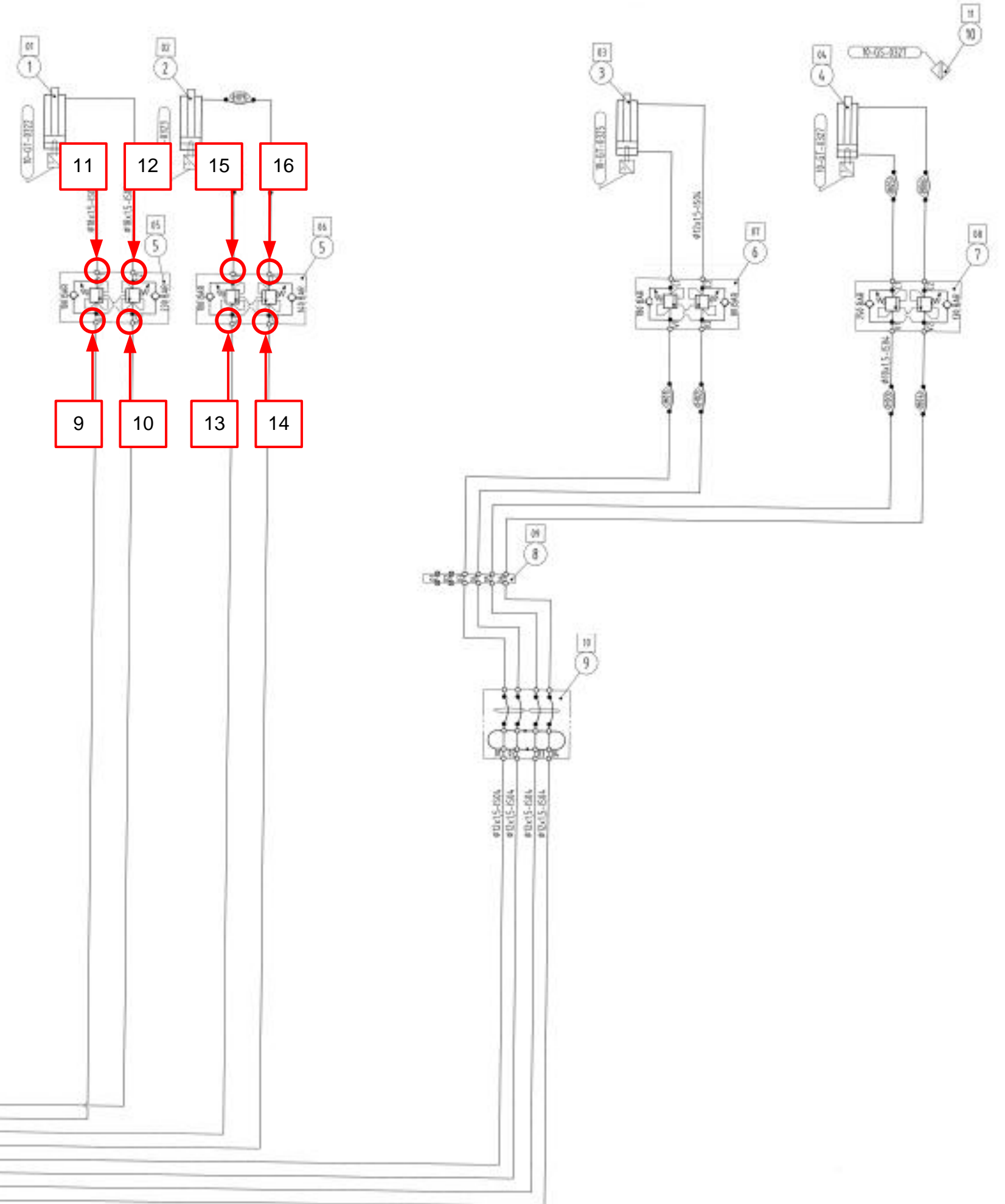
Date	Drawn	Traced	Scale	 Aker Solutions Aker MH AS
26-SEP-19	TS2	AKA	NA	
Checked	Approved	Projector		Prepared by: _____ Approved by: _____ Format: Drawing number: _____ Rev: _____

BC02 LOWER GUIDING ARM TYPE 192136
 CONTROL VALVE UNIT & SLEWING
 HYDRAULIC FLOW DIAGRAM, SHEET 03

Format: A1 Drawing number: 1921315 Rev: 01

COMP ID	FUNCTIONAL DESCRIPTION
01	HS TILT
02	TELESCOPE
03	HEAD TILT
04	GRAB HEAD AMP
05	LCV HS TILT
06	LCV TELESCOPE
07	LCV HEAD TILT
08	LCV GRAB HEAD CL AMP
09	BULKHEAD PLATE TO HOSE REEL
10	HOSE REEL, BLADE HEAD/HEAD TILT
11	PIPE DETECTOR SENSOR

100



This document and all information and data disclosed herein or hereunder are the confidential and proprietary property of Aker MH AS and are not to be used, reproduced or disclosed in whole or in part by or to anyone without the written permission of Aker MH AS

THIS IS A COMPUTER AIDED DRAWING AND MUST NOT BE ALTERED MANUALLY

Tolerances except as noted: Milling and Turnwork except as noted

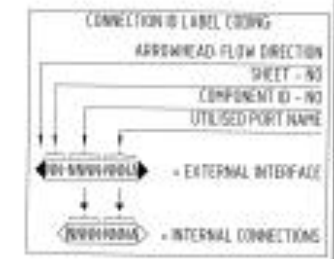
REV	DESCRIPTION OF REVISION	CHK	APP	DATE / SIGN
01	ISSUED FOR CONSTRUCTION	U/Am	Spr	24-SEP-2016/AA

NOTE:

HYDRAULIC TUBE / PIPE / FITTING / FLANGE:
 PROPERTIES ACC. TO MH STD. PIPING SPECIFICATION, SA13-0011
 TUBE / PIPE DIMENSION / PIPING CLASS SHEET ACC. TO FLOW DIAGRAM

PRESSURE FLUID:
 HYDRAULIC MINERAL OIL ISO HV TYPE (DIN HVLPI)
 PERMISSIBLE UPPER OPERATIONAL CONTAMINATION LIMIT TO BE APPROVED ACCORDING TO ONE OF THE FOLLOWING STANDARDS:
 ISO 4406, CODE - / IS / IS OR
 SAE AS 4059, REV. E, TABLE 2, CLASS 1 B-F OR
 SAE AS 4059, REV. E, TABLE 1, CLASS 7

GRAPHICAL SYMBOLS:
 BASED ON ISO 1219 AND EN 60917-2



Qty	Item	Description	Draw. Material	Unit weight	Part number
1	00	COMPONENT ID NUMBER	PHI 1372313, RANGE 04-01 TO 04-25		6/913
1	11	HOSE KIT - ISO12151-2/3	BAC026268-BC02-HYDRAULIC SYSTEMS		76288
1	10	SENSOR W/TS MTR. CABLE (10x28x8)	NE810-38-0M-L8-80		27706
1	9	10PL. HOSE REEL, W/HOSE, MARINE EDITION	A445295 06/RT, 137DEMAC, 4, 1M Hose		76480
1	8	BULKHEAD UNION PLATE	PH 1924-842		11111
1	7	DOUBLE ACTING OVERCENTRE VALVE	V850-DE-NA 0542 25-18-82-35		19347
1	6	DOUBLE ACTING OVERCENTRE VALVE	V850-DE-NA 0542 25-18-82-28		30676
2	5	DOUBLE ACTING OVERCENTRE VALVE PLUS	V850-DE-CC 0542 05-18-84-35		22431
1	4	HYDRAULIC TUBING (MTR) W/TEMPERATURE SENSOR	CM 250 CH 063/04 0X08190 0H82, SA29		51613
1	3	HYDRAULIC TUBING (MTR) W/TEMPERATURE SENSOR	CM 250 CH01 063/03200230 1PH 0H82, SA29		58491
1	2	HYDRAULIC TUBING (MTR) W/TEMPERATURE SENSOR	CM 250 CH01 063/04015171PH 0H82, SA29		58498
1	1	HYDRAULIC TUBING (MTR) W/TEMPERATURE SENSOR	CM 250 CH01 025/0300754 1PH 0H82, SA29		58489

SHEET 03

24-826-10 | Scale: NA | AkerSolutions Aker MH AS

BC02 LOWER GLIDING ARM TYPE 1922136
 HYDRAULIC SYSTEMS
 HYDRAULIC FLOW DIAGRAM, SHEET 04

Formal	Drawing number	Rev.
A1	1921316	01

Appendix D

Functions, θ_1 and θ_3

From equation 2.31 and 2.33 this expression is solved for $\theta_1, f_1(d_1)$:

$$\begin{aligned} \theta_1 = & -\log\left(d_1^2 \cdot \left(\frac{2191}{7619925550} - \frac{34 \cdot i}{761992555}\right)\right) \\ & + \sqrt{\left(\frac{87247290729882095616}{14515816346885700625} + d_1^4 \cdot \left(\frac{4684881}{14515816346885700625} - \frac{297976 \cdot i}{2903163269377140125}\right)\right)} \\ & + d_1^2 \cdot \left(\frac{3287691974112 \cdot i}{2903163269377140125} - \frac{51690222243972}{14515816346885700625}\right) \\ & - \frac{5549254869553217536 \cdot i}{2903163269377140125} \Bigg) / 2 \\ & - \frac{6043551423}{3809962775} + \frac{187568004 \cdot i}{761992555} \Bigg) \cdot i \quad (D.1) \end{aligned}$$

Expression for $\theta_3, f_3(d_3)$:

$$\begin{aligned} \theta_3 = & -\log\left(d_3^2 \cdot \left(\frac{47i}{29407824} + \frac{193}{73519560}\right) + \left(\frac{21153577395728}{3127966263075} + \right.\right. \\ & \left. d_3^4 \cdot \left(\frac{9071i}{270256285129680} + \frac{3473}{200189840836800}\right) + \right. \\ & \left. d_3^2 \cdot \left(-\frac{798302426i}{16891017820605} - \frac{152822419}{6255932526150} + \right.\right. \\ & \left. \left. \frac{221000979621824i}{16891017820605}\right)^{0.5} / 2 - \frac{16985158}{9189945} - \frac{2068141i}{1837989}\right) \cdot i \quad (D.2) \end{aligned}$$

Appendix **E**

Valve, Technical data

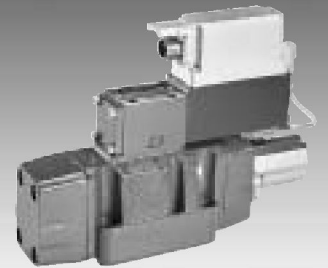
Servo solenoid valves with positive overlap and on-board electronics

RE 29089/01.05
Replaces: 05.04

1/22

Type 4WRLE 10...35, symbols E./W.

Nominal size 10, 16, 25, 35
Unit series 3X
Maximum working pressure P, A, B 350 bar, T 250 bar
Nominal flow rate 50...1,100 l/min (Δp 10 bar)



Overview of contents

Contents	Page
Features	1
Ordering data and scope of delivery	2
Preferred types	3
Function, sectional diagram	3
Accessories	4
Control oil supply	4
Symbols	5 and 6
Technical data	7 to 9
On-board trigger electronics	10
Characteristic curves	11 to 15
Unit dimensions	16 to 19
Mounting hole configurations	20 and 21

Variants on request

- For standard applications
- Special symbols and characteristic curves with/without intermediate plates

Features

- Pilot operated servo solenoid valves NG10 to NG35 with positive overlap, see symbols E./W. and characteristic curves
- Pilot valve NG6, with control piston and sleeve in servo quality
- Actuated on one side, 4/4 fail-safe position when switched off
- Control solenoid with integral position feedback and on-board valve electronics (OBE), calibrated at the factory
- Main stage with approx. 20% overlap and position feedback
- Electronically compensated, calibrated overlap, see characteristic curve range ± 0.5 V
- Spool with linear travel, with anti-rotation element
- Flow characteristic
 - S = Progressive
 - NG16 and 25 with load tap C1/C2
- Suitable for electrohydraulic controllers in production systems with more demanding requirements
- For subplate attachment, mounting hole configuration NG10 to ISO 4401-05-05-0-94, NG16 to ISO 4401-07-06-0-94, NG25 to ISO 4401-08-07-0-94 and NG32 to ISO 4401-10-08-0-94
- Subplates as per catalog section, NG10 RE 45055, NG16 RE 45057, NG25 RE 45059 and NG32 RE 45060 (order separately)
- Plug-in connectors to DIN 43563-AM6, see catalog section RE 08008 (order separately)

Ordering data and scope of delivery

4WRL	E		Z	S	J -3X	H / G24		K0 / A1	M	*
------	---	--	---	---	-------	---------	--	---------	---	---

With **on-board**
trigger electronics

= E

Nominal size 10

= 10

Nominal size 16

= 16

Nominal size 25

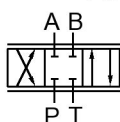
= 25

Nominal size 35¹⁾

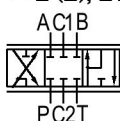
= 35

Symbols

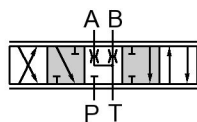
= E, E1



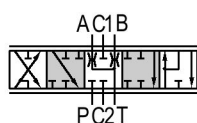
= E (Z), E1 (Z)



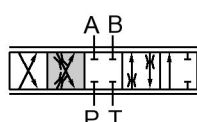
= W, W1



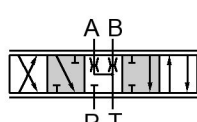
= W (Z), W1 (Z)



= E4



= W4



 Transitional symbols

With symbol E1, E1(Z), E4, W1(Z), W4:

P → A: q_v B → T: $q_{\sqrt{2}}$

P → B: $q_{\sqrt{2}}$ A → T: q_v

Further information
in plain text

M = NBR seals,
suitable for mineral oils
(HL, HLP) to DIN 51524

**Interface for
trigger electronics**

A1 = Setpoint input ± 10 V

Electrical connection

K0 = without plug-in connector, with
plug to
DIN 43563-AM6

Order plug-in connector separately

Control oil supply "x", control oil outlet "y"

No code = "x" = external, "y" = external

E = "x" = internal, "y" = external

ET = "x" = internal, "y" = internal

T = "x" = external, "y" = internal

Voltage supply of trigger electronics

G24 = +24 V DC

H = Highflow version (on request)

3X = Unit series 30 to 39
(installation and connection dimensions unchanged)

J = **Overlap compensation signal**
See characteristic curve range: ± 0.5 V

Flow characteristic

Progressive

S = **Nominal flow rate at 10 bar valve pressure difference**

Nominal size

10 = 50 or 85 l/min

16 = 180 l/min

25 = 350 or 430 l/min

35 = 1,100 l/min

Z = With load tap C1/C2

¹⁾ NG35 is a high flow version of the NG32,
ports P, A, B and T have $\varnothing 50$ mm in the
main stage.

Contrary to the standard, ports P, A, B
and T may be drilled to max. $\varnothing 48$ mm in the
control block.

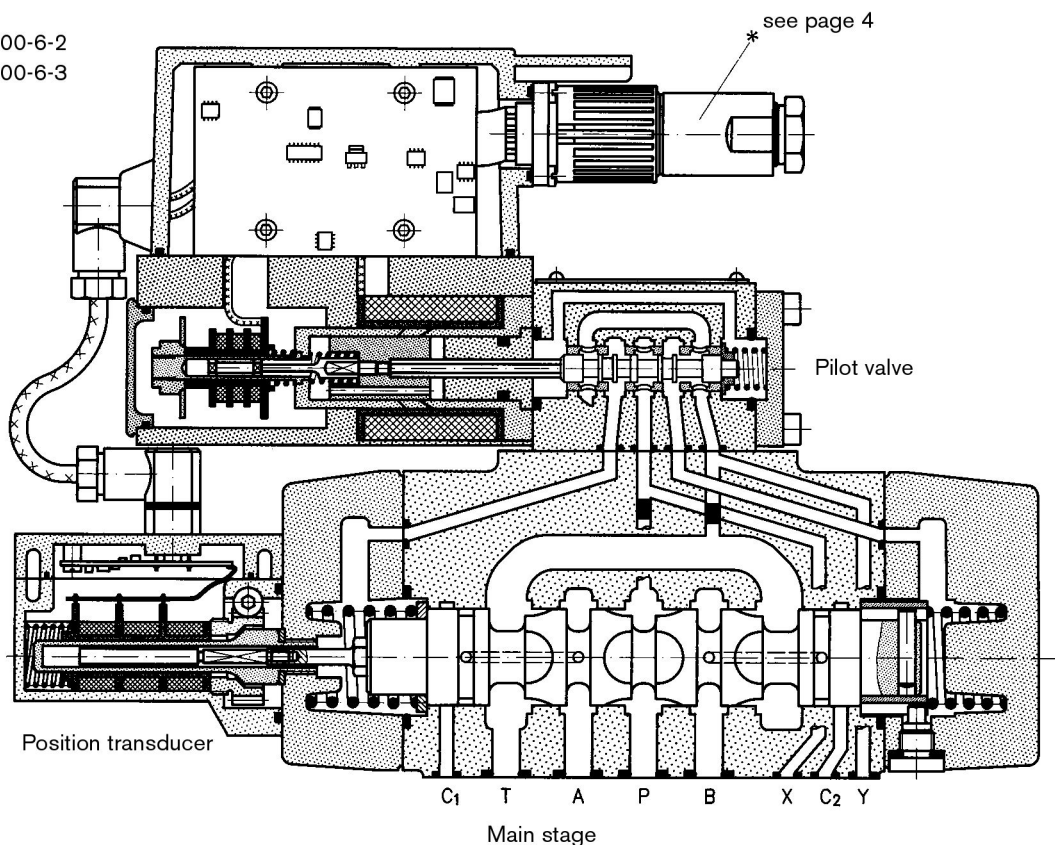
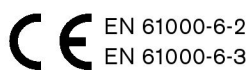
These valves therefore provide higher flow
rates $Q_A : Q_B$.

Preferred types (available at short notice)

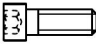

Type 4WRLE	Material No.	Type 4WRLE	Material No.
E, E1, E4, W, W1, W4	NG10	E (Z), E1 (Z), E4, W (Z), W1 (Z), W4	NG25
4WRLE10E-80SJ-3X/G24KO/A1M	0 811 404 700	4WRLE25EZ-350SJ-3X/G24KO/A1M	0 811 404 454
4WRLE10E-80SJ-3X/G24ETKO/A1M	0 811 404 713	4WRLE25EZ-350SJ-3X/G24TKO/A1M	0 811 404 466
4WRLE10E1-80SJ-3X/G24KO/A1M	0 811 404 701	4WRLE25EZ-350SJ-3X/G24ETKO/A1M	0 811 404 481
4WRLE10E1-80SJ-3X/G24ETKO/A1M	0 811 404 715	4WRLE25E1Z-350SJ-3X/G24KO/A1M	0 811 404 455
4WRLE10E4-80SJ-3X/G24KO/A1M	0 811 404 714	4WRLE25E4-350SJ-3X/G24KO/A1M	0 811 404 459
4WRLE10W-50SJ-3X/G24ETKO/A1M	0 811 404 704	4WRLE25WZ-350SJ-3X/G24KO/A1M	0 811 404 456
4WRLE10W-80SJ-3X/G24KO/A1M	0 811 404 702	4WRLE25W1Z-350SJ-3X/G24EKO/A1M	0 811 404 476
4WRLE10W-80SJ-3X/G24ETKO/A1M	0 811 404 707	4WRLE25W1Z-350SJ-3X/G24KO/A1M	0 811 404 457
4WRLE10W1-80SJ-3X/G24KO/A1M	0 811 404 703	4WRLE25W4-350SJ-3X/G24ETKO/A1M	0 811 404 471
4WRLE10W4-80SJ-3X/G24KO/A1M	0 811 404 711	4WRLE25W4-350SJ-3X/G24KO/A1M	0 811 404 472
E (Z), E1 (Z), W (Z), W1 (Z), W4	NG16	W	NG35
4WRLE16EZ-180SJ-3X/G24ETKO/A1M	0 811 404 319	4WRLE35W-1100SJ-3X/G24KO/A1M	0 811 404 504
4WRLE16EZ-180SJ-3X/G24TKO/A1M	0 811 404 318		
4WRLE16EZ-180SJ-3X/G24KO/A1M	0 811 404 305		
4WRLE16E1Z-180SJ-3X/G24KO/A1M	0 811 404 306		
4WRLE16WZ-180SJ-3X/G24KO/A1M	0 811 404 307		
4WRLE16W1Z-180SJ-3X/G24ETKO/A1M	0 811 404 327		
4WRLE16W1Z-180SJ-3X/G24KO/A1M	0 811 404 308		
4WRLE16W4-180SJ-3X/G24ETKO/A1M	0 811 404 328		
4WRLE16W4-180SJ-3X/G24KO/A1M	0 811 404 333		

Function, sectional diagram

Servo solenoid valve 4WRLE10...35



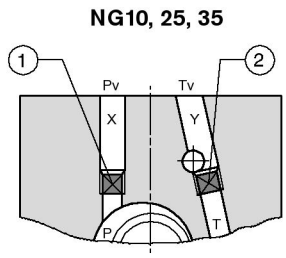
Accessories, not included in scope of delivery

Fastening screws 	NG10	4 x M6 x 40, DIN 912-10.9	2910 151 209	
	NG16	2 x M6 x 45, DIN 912-10.9	2910 151 211	
		4 x M10 x 50, DIN 912-10.9	2910 151 301	
	NG25	6 x M12 x 60, DIN 912-10.9	2910 151 354	
	NG35	6 x M20 x 90, DIN 912-10.9	2910 151 532	
* 	Plug-in connectors 6P+PE, see also RE 08008		KS	1 834 482 022
			KS	1 834 482 026
			MS	1 834 482 023
			MS	1 834 482 024
			KS 90°	1 834 484 252

Testing and service equipment

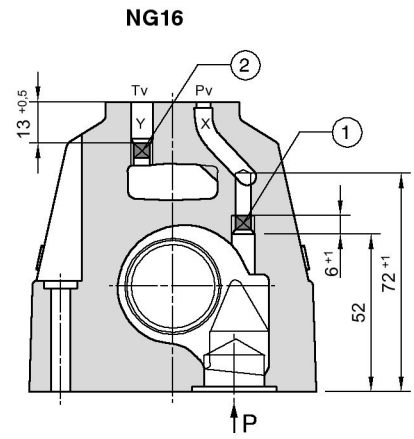
- Test box type VT-PE-TB3, see RE 30065
- Test adapter 6P+PE type VT-PA-2, see RE 30068

Control oil supply



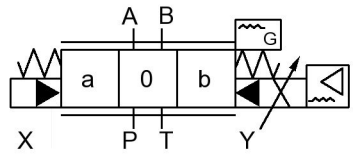
NG10, 25, 35

Plug ① ②
 NG10...25 **1 813 464 007 SW 3**
 NG35 **1 813 464 001 SW 4**

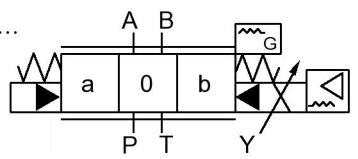


NG16

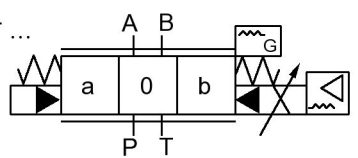
Type ... -3X ...



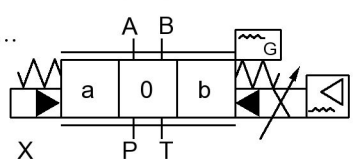
Type ... -3X ... E ...



Type ... -3X ... ET ...

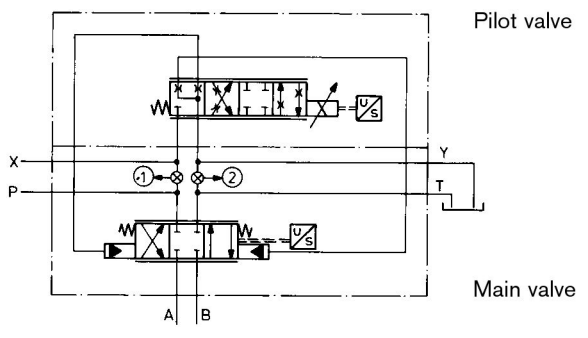


Type ... -3X ... T ...



No code = "x" = external, "y" = external
E = "x" = internal, "y" = external
ET = "x" = internal, "y" = internal
T = "x" = external, "y" = internal

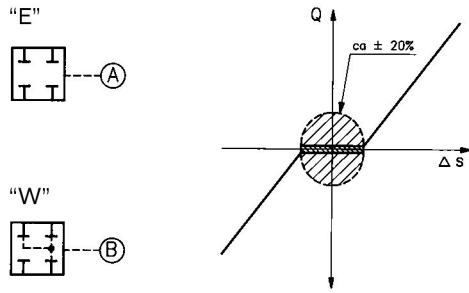
Symbol in detail



Conversion

The pilot valve can be supplied with oil both via ports X and Y (external) and from the main flow ducts P and T.
 In the basic version, the valve is equipped with the plugs ① and ②, i.e. X and Y are external.
 For valve versions with X and/or Y as internal, see ordering overview or carry out the conversion (see diagram above).
 When the control oil supply or outlet is changed, the part number must also be changed.

Symbols in mid position "E" or "W" ..



Spool valves with overlap

With symbol "E", leakage oil in the two work chambers A and B of the control piston results in a build-up of pressure in A or B, which then causes a connecting cylinder to drift out of position. In many cases, the "W" symbol is a better solution. With a setpoint of "0", the control piston moves into the overlapped mid position.

In this mid position, pressure is then relieved from ports A and B with small openings to T.

This also supports the function of external check valves.

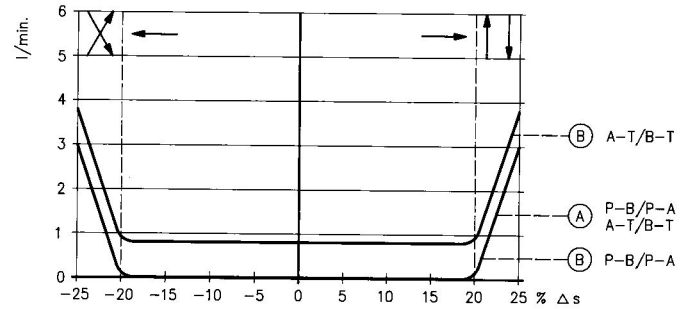
Flow in mid position "leakage pressure relief"

$$Q = f(\Delta s)$$

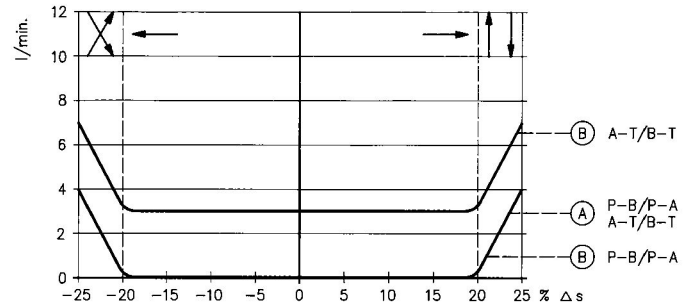
$$0 \dots \pm 25\%$$

$$Q_x = Q_{nom} \cdot \sqrt{\frac{\Delta p_x}{5 \text{ bar}}}$$

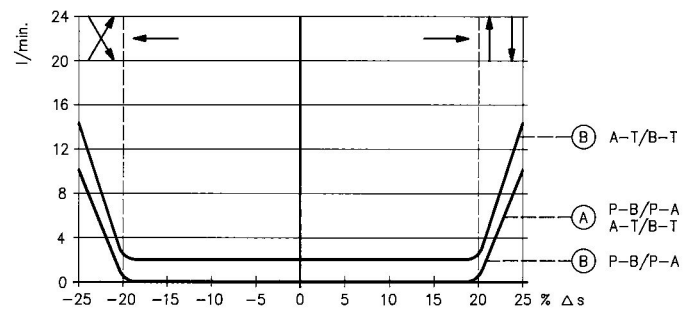
NG10



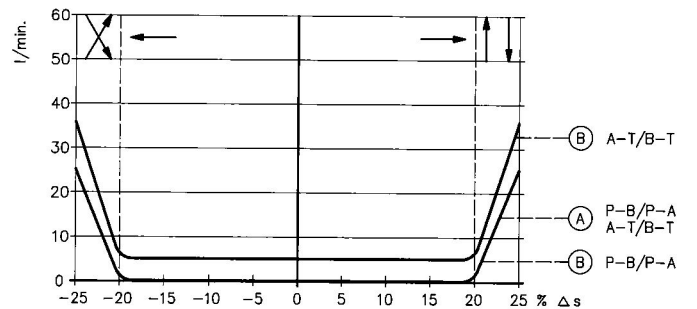
NG16



NG25



NG35

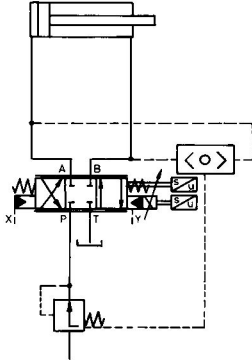


Load tap C1/C2

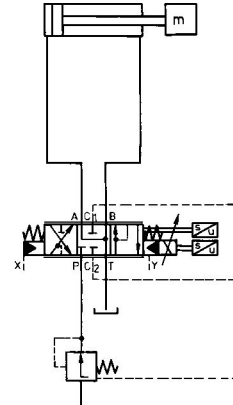
To compensate for fluctuations in the load or supply pressure, proportional valves are combined with pressure compensators. The load is tapped through a shuttle valve for the NG10 and 35, and through two additional ports C1 and C2 for NG16 and 25 ("4WRL" and "4WRLE" only).

The pressure compensator therefore always receives the correct pressure signal even in the event of negative load. When using pressure compensators, external control oil supply should always be selected.

NG10, 35



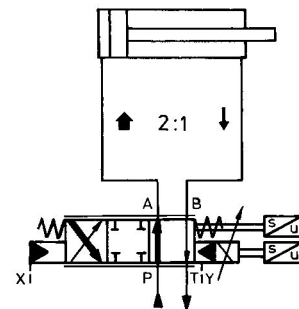
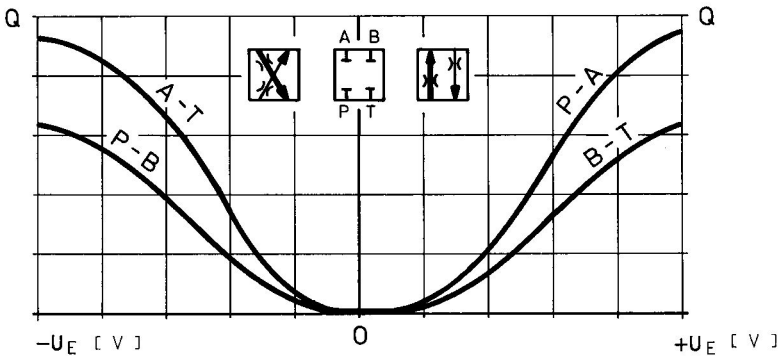
NG16, 25



Asymmetrical valve spool $Q_A : Q_B = 2:1$

The two throttle cross-sections of proportional directional control valves are usually symmetrical.

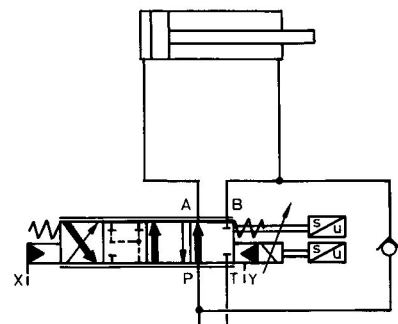
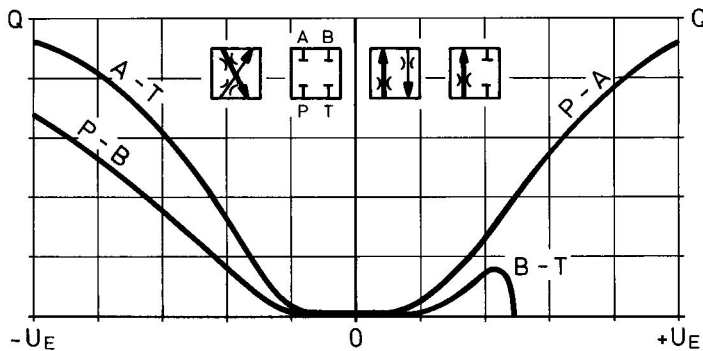
In order to adapt to differential cylinders with different with asymmetrical metering notches are available. A comparison of the flow rates can be found in the product range overview "Preferred types, characteristic curves".



Valve spools in a differential circuit

In order to produce differential circuits, valve spools with an additional "4th position" are available (see diagram). It is sufficient to install a check valve in the consumer lines. In addition, a symbol (spool) with internal B-P connection is

employed for certain "branch-oriented solutions". However, we recommend that you consult the BRH Application Center with regard to these special symbols. As a rule, a simulation or knowledge of this type of system is required.



Technical data


General

Construction	Spool type valve, pilot operated				
Actuation	Servo solenoid valve NG6, with position controller for pilot valve and main stage				
Type of mounting	Subplate, mounting hole configuration NG10...35 (ISO 4401-...)				
Installation position	Optional				
Ambient temperature range	°C	-20 ... +50			
Weight	kg	NG10 8.7	NG16 10.6	NG25 18.4	NG35 81
Vibration resistance, test condition	max. 25 g, shaken in 3 dimensions (24 h)				

Hydraulic (measured with HLP 46, $\vartheta_{oil} = 40^\circ\text{C} \pm 5^\circ\text{C}$)

Pressure fluid	Hydraulic oil to DIN 51524 ... 535, other fluids after prior consultation				
Viscosity range	recommended	mm ² /s	20 ... 100		
	max. permitted	mm ² /s	10 ... 800		
Pressure fluid temperature range	°C	-20 ... +70			
Maximum permissible degree of contamination of pressure fluid Purity class to ISO 4406 (c)	Class 18/16/13 ¹⁾				
Direction of flow	See symbol				
Nominal flow at $\Delta p = 5$ bar per notch ²⁾	l/min	NG10	NG16	NG25	NG35
		50, 80	180	350	1,100
Max. working pressure in P, A, B		350	350	350	350
Max. pressure in X (ext.)		280			
Max. pressure in P (X = int.)		280			
Max. pressure in T (Y = ext.)	bar	250			
Max. pressure in T (Y = int.)		250			
Max. pressure in Y (ext.)		250			
Min. control oil pressure of "pilot stage"		8			
Q_{max}	l/min	170	450	900	3,500
Q_N pilot valve (supply pressure) $\Delta p = 35$ bar	l/min	2	4	12	40
Leakage of pilot valve at 100 bar	cm ³ /min	<150	<180	<350	<1,100
Leakage of main stage Sb "E" at 100 bar Q_N : Sb "W", see graph on page 5	l/min	<0.25	<0.4	<0.6	<1.1

Static/Dynamic

Overlap in mid position	≈18 ... 22 % of spool stroke, electrically adjustable for $U_{D-E} \pm 0.5$ V				
Spool stroke, main stage	± mm	4	7	10	12.5
Control oil volume of main stage 100 %	cm ³	1.1	4.3	11.3	41.5
Control oil requirement 0 ... 100 %, $x = 100$ bar	l/min	2.2	4.7	11.7	15.6
Hysteresis	%	< 0.1, scarcely measurable			
Manufacturing tolerance	%	< ±5 (Q_{max})			
Response time for 0 ... 100 %, $x = 100$ bar	ms	<40	<80	<80	<130
Response time for 0 ... 100 %, $x = 10$ bar	ms	<150	<250	<250	<500
Switch-off behavior	After electrical shut-off (pilot valve in "fail-safe") Main stage moves to spring-centered mid position (Sb "E../W..")				
Thermal drift	<1 % at $\Delta T = 40^\circ\text{C}$				
Calibration	At factory ±1 %, see flow curve				
Conformity	 EN 61000-6-2 EN 61000-6-3				

¹⁾ The purity classes stated for the components must be complied with in hydraulic systems.
Effective filtration prevents problems and also extends the service life of components.
For a selection of filters, see catalog sections RE 50070, RE 50076 and RE 50081.

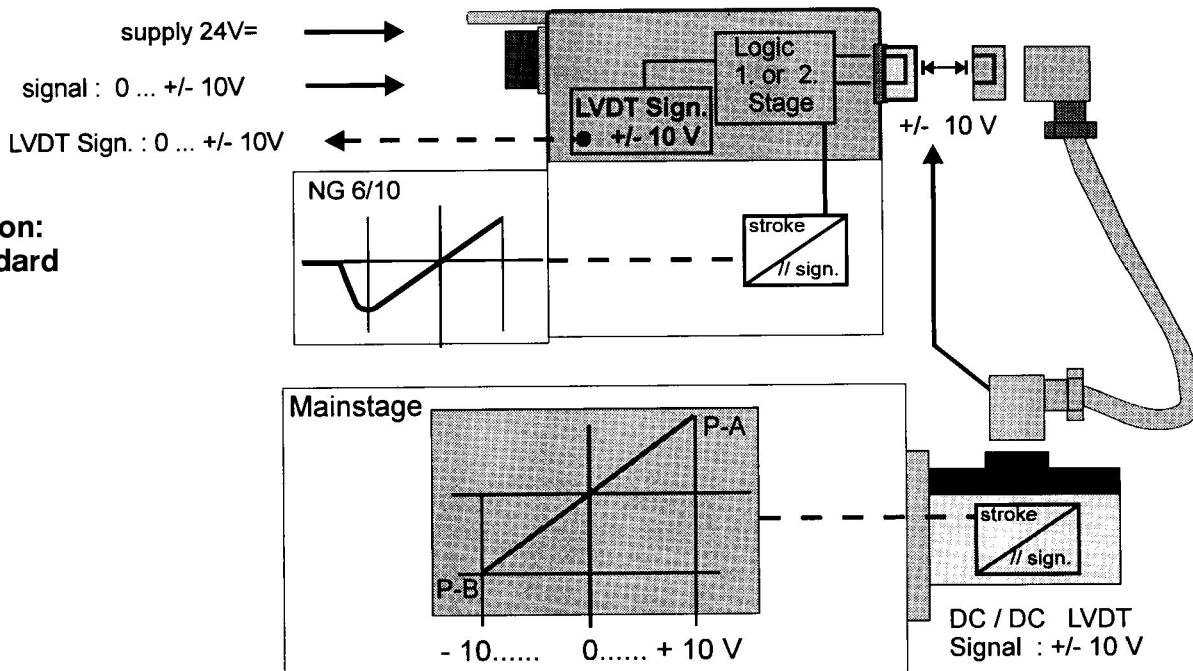
²⁾ Flow rate at a different Δp $q_x = q_{nom} \cdot \sqrt{\frac{\Delta p_x}{5}}$

Technical data

Electric pilot valve NG6, valve with on-board electronics

Cyclic duration factor	%	100
Degree of protection		IP 65 to DIN 40050 and IEC 14434/5
Connection		Plug-in connector 6P+PE, DIN 43563
Power supply		24 V DC _{nom}
Terminal A:		min. 21 V DC/max. 40 V DC
Terminal B: 0 V		Ripple max. 2 V DC
Power consumption		Solenoid \square 45 mm = 40 VA max.
External fuse		2.5 A _F
Input, "Standard" version		Difference amplifier, $R_i = 100 \text{ k}\Omega$
Terminal D: U_E		0... $\pm 10 \text{ V}$
Terminal E:		0 V
Max. differential input voltage at 0 V		$\left. \begin{array}{l} D \rightarrow B \\ E \rightarrow B \end{array} \right\} \text{max. } 18 \text{ V DC}$
Test signal, "Standard" version		LVDT
Terminal F: U_{Test}		0... $\pm 10 \text{ V}$
Terminal C:		Reference 0 V
Protective conductor and screen		See pin assignment (installation conforms to CE)
Recommended cable		See pin assignment up to 20 m 7x0.75 mm ² up to 40 m 7x1 mm ²
Calibration		Overlap and P-A at +8 V, calibrated at the factory, see valve characteristic curve

Version: Standard



Important

Pilot operated servo solenoid valves with positive overlap perform their function in open or closed-loop-controlled axes and have approx. 20% overlap when switched off. This condition does not constitute an active, safe basic position. For this reason, many applications require the use of "external check valves" or certain sandwich-mounted valves, which must be taken into account during the On/Off switching sequence.

Further testing of the complex algorithm

F.1 Intro

To learn about the complex method and how sensitive it is to the input parameter like population, and boundary conditions, some experimental testing was done. This test was based on the step response of the control directional valve(see section 2.2). This system was chosen because it had few variables and the best solution was relatively easy to find. For each parameter setting the algorithm run hundred times and logged each error value. The error in this case is the deviation between the smallest possible error and the error in each optimization routine.

F.2 Results

The routine is ran a hundreded times and x number of solutions are devided into two groups:

$$\text{Gr.1:} \quad ERROR < E_{best} \pm 0.4\%$$

$$\text{Gr.2:} \quad E_{best} \pm 0.4\% < ERROR < E_{best} \pm 2.0\%$$

Error value:

$$E_v = \sum e^2 \quad (\text{F.1})$$

$$ERROR = E_v - E_{best} \quad (\text{F.2})$$

Error function in algorithn:

$$Err = E_v \cdot K \quad (\text{F.3})$$

E_{best} : Best/lowest possible error.

E_v : Error value, obtained in each routine.

ERROR: Calculated error deviation.

Err : Costfunction used in the algorithm.

APPENDIX F. FURTHER TESTING OF THE COMPLEX ALGORITHM

The table below show 17 different test parameter settings. Each parameter design is ran 100 times with the complex algorithm.

Test no.	C	K	B	x	y
1	3	1	$\pm 60\%$	2	98
2	3	10	$\pm 60\%$	32	68
3	3	50	$\pm 60\%$	80	20
4	3	100	$\pm 60\%$	89	11
5	3	1000	$\pm 60\%$	96	4
6	5	10	$\pm 60\%$	70	30
7	5	50	$\pm 40\%$	99	1
8	5	50	$\pm 60\%$	99	1
9	5	50	$\pm 80\%$	100	0
10	5	50	$\pm 100\%$	100	0
11	5	50	$\pm 280\%$	85	15
12	5	50	$\pm 350\%$	52	47
13	10	50	$\pm 280\%$	91	9
14	15	50	$\pm 280\%$	48	52
15	15	50	$\pm 60\%$	100	0
16	20	50	$\pm 280\%$	0	99
17	30	50	$\pm 280\%$	0	97

Table F.1: Experimental data

C: Population

K: Error gain

B: Boundary condition for the parameters, ζ and ω . Upper and lower symmetric boundary compared to the best values, $\zeta = 0.90$ and $\omega = 52.5$.

x: Number of solutions with a deviation less than 0.4% of the best possible error, $0.807 \cdot 10^{-3}$.

y: Number of solutions with a deviation less than 2% and higher than 0.4%

F.3 Effect of changing the error gain

The error function is given by the equation F.3. By freezing the parameters B and C I tested the effect of changing K.

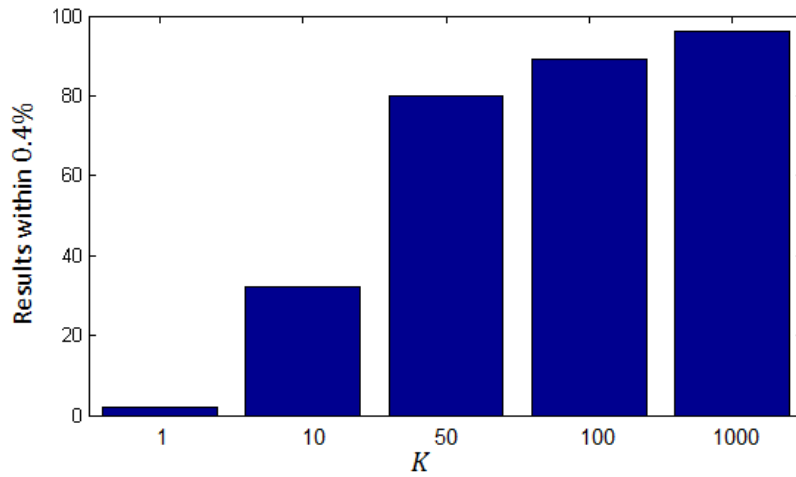


Figure F.1: Effect of changing the parameter K. $C = 3$, $B = \pm 60\%$

F.4 Effect of changing the population

To see the effect of the population parameter, C , I set the error gain to 50 and boundaries to 250%.

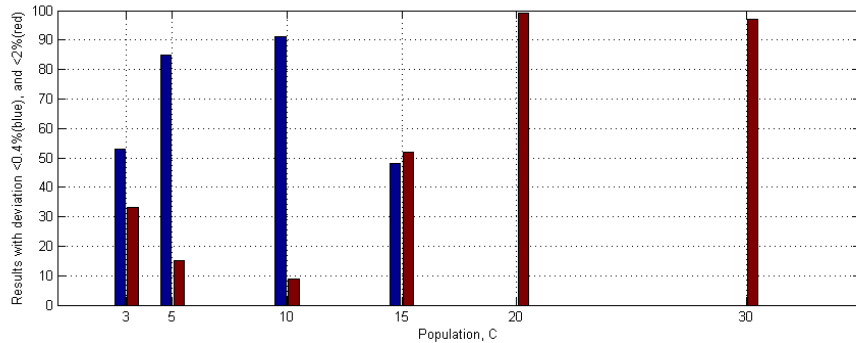


Figure F.2: Deviation dependent on population. Stats from tabular F.1. Blue bars has a deviation $< 0.4\%$, red has $< 2\%$ and $> 0.4\%$

The figure F.2 show that a to high population will increase the error. A population of 30 will in this case lead to no results within 0.4% . This result is valid for this test and this test only, and it could be possible that the best population will change dependent on the size of the parameter boundaries. This indication is verified by comparing test result number 3 and 8, see table F.1.

F.5 Effect of changing the boundaries

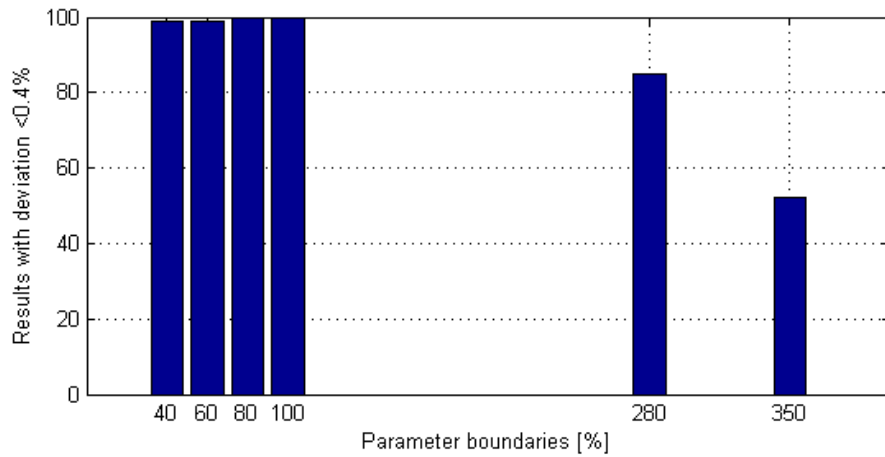


Figure F.3: Deviation dependent on parameter boundaries

From this I conclude that the result is not very sensitive to the boundary conditions, as long as they embrace the optimal parameter size. The figure (F.3) show that our result will get a bit less optimal with high bandwidth on the boundary settings. A high bandwidth can be compensated with a larger population(see F.4). A consequence of increasing bandwidth and population is a significant increase in simulation time. I also notice a small but escalated error deviation when the boundaries are very low. This abnormal result is not significant and is ignored.

Appendix G

Simulink model of valve

$$\begin{aligned}\zeta &= 0.90 \\ \omega &= 52.5 \\ A_{btv} &= 1.25e-4 \\ A_n &= 2.08e-006\end{aligned}$$

APPENDIX G. SIMULINK MODEL OF VALVE

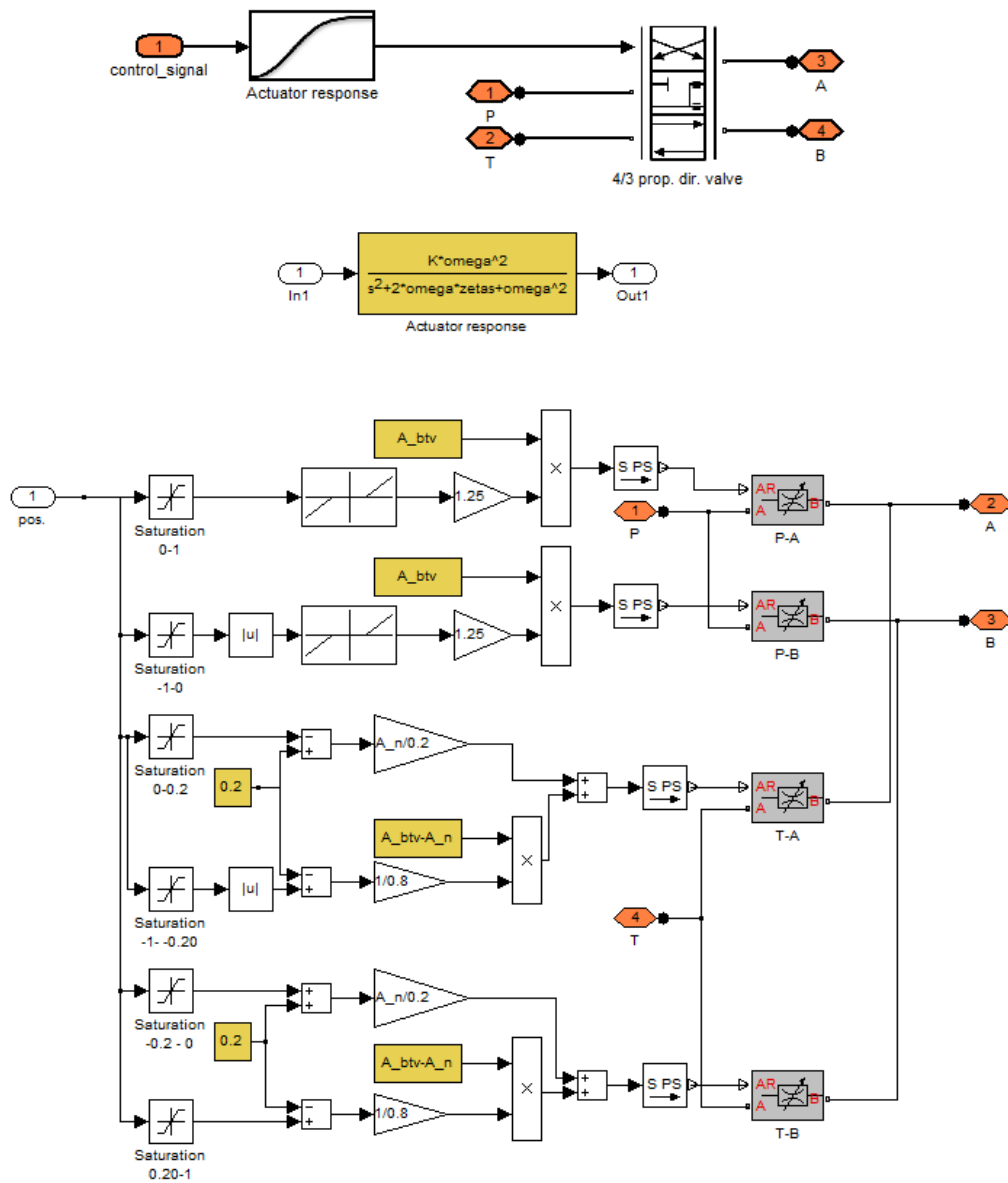


Figure G.1: Simulink model of directional control valve

Appendix **H**

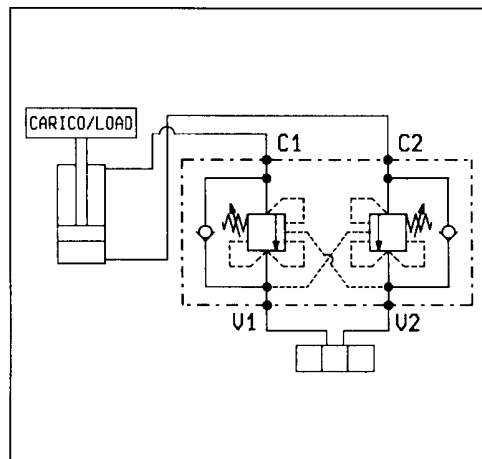
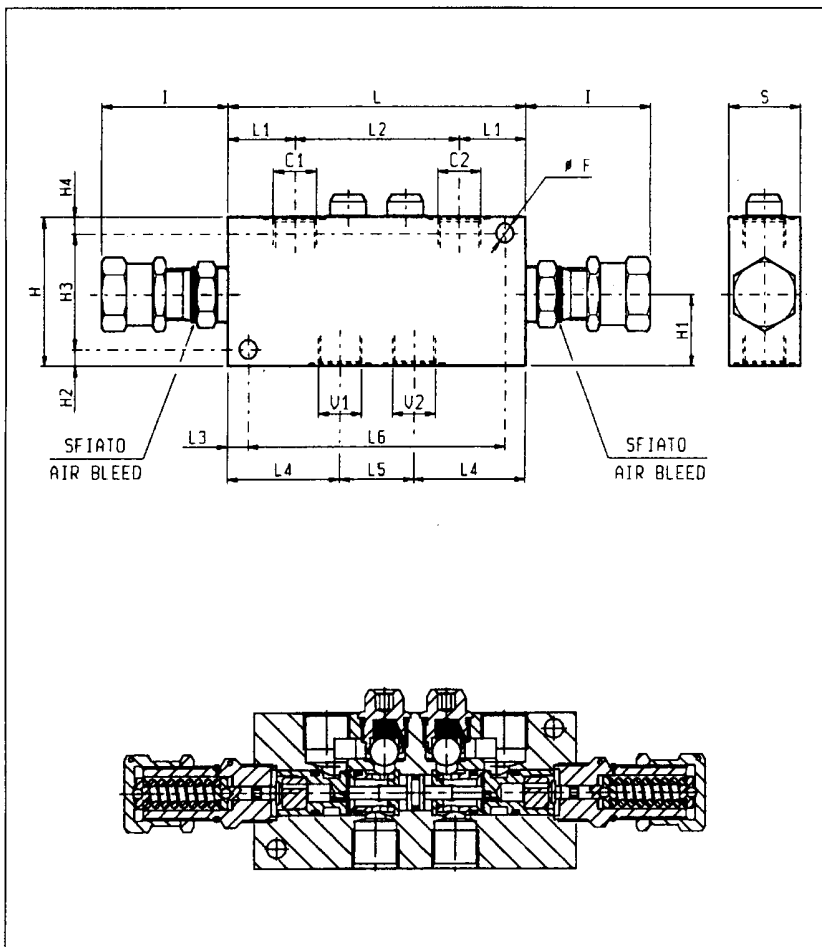
VBSO over center valve



BILANCIAMENTO, DOPPIO EFFETTO, VERSIONE "CC"
DUAL PILOT ASSISTED, "CC" TYPE OVERCENTRE

VBSO-DE-CC

05.42.05- X - Y - Z



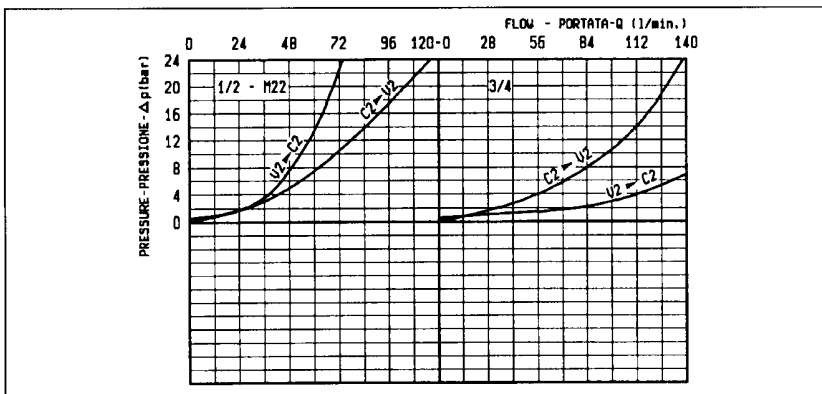
DATI TECNICI / TECHNICAL DATA

Pressione max. 350 bar
 Max. pressure

Portata max. vedi diagramma
 Flow see performance graph

Taratura della valvola: almeno 1.3 volte superiore alla pressione indotta dal carico
 Pressure setting: at least 1.3 times the load induced pressure

40	155	50	62.5	10	107	34	175	65	10	70	10	38	90	10.5	3/4	2.15
35	125	36	54.5	10	86	29.5	145	65	8	54	8	33	70	8.5	M22	1.45
35	125	36	54.5	10	80	32.5	145	65	8	54	8	33	70	8.5	1/2	1.45
S	L6	L5	L4	L3	L2	L1	L	I	H4	H3	H2	H1	H	F	Y	Peso kg Weight kg



X	RAPPORTO DI PILOTAGGIO PILOT RATIO
02	8.2 : 1
10	3.2 : 1

Z	MOLLE / SPRINGS				
	Campo taratura min - max bar Adj. press. range bar	Incremento press. bar / giro vite Press. increase bar / turn	Taratura standard bar (Q = 5 l/min) Std. setting bar (made at = 5 l/min)	Cod. ordinazione Ordering code	Colore Colour
20	60-210	54	200	03.51.01.075	verde green
35	100-350	95	350	03.51.01.059	giallo yellow

Y	ATTACCHI / PORT SIZE	
	V1-V2-C1-C2	
03	G 1/2	
04	G 3/4	
89	M22x1.5	

Hydraulic Motor F12 series

Specifications

Frame size	30	40	60	80	110
Displacement [cm ³ /rev] [cu. in./rev]	30 1.83	40 2.44	59.8 3.65	80.4 4.90	110.1 6.72
Motor operating speed [rpm]					
max intermittent	7100	6400	5600	5200	4700
max continuous	5600	5000	4300	4000	3600
min continuous	50	50	50	50	50
Max pump selfpriming speed [rpm]	2850	2650	2350	2350	2200
Torque (theor.) at 100 bar [Nm] [In-lb]	47.6 29	63.5 38.7	94.9 58.1	127.6 77.5	174.8 106.6
Motor input flow					
max intermittent [l/min] [gpm]	213 56.3	256 67.6	335 88.5	418 110.4	517 136.6
max continuous [l/min] [gpm]	168 44.4	200 52.8	257 67.9	322 85.1	396 104.6
Output power					
max intermittent [kW] [HP]	110 150	130 177	175 238	220 300	270 361
max continuous [kW] [HP]	70 95	85 115	110 150	153 184	165 221
Operating pressure					
max intermittent [bar] [psi]	480 7000	480 7000	480 7000	480 7000	480 7000
max continuous [bar] [psi]	420 6000	420 6000	420 6000	420 6000	420 6000
Max case pressure at 1500 rpm [bar] [psi]	14 200	12 175	12 175	10 145	9.5 140
Main circuit temperature, max. [°C] [°F]	80 176	80 176	80 176	80 176	80 176
min. [°C] [°F]	-40 -40	-40 -40	-40 -40	-40 -40	-40 -40
Fluid viscosity, max. [mm ² /s] [SUS]	1000 5000	1000 5000	1000 5000	1000 5000	1000 5000
min. [mm ² /s] [SUS]	8 58	8 58	8 58	8 58	8 58
Fluid contamination level (ISO code 4406)	18/13	18/13	18/13	18/13	18/13
Mass moment of inertia (x10 ⁻³) [kg m ²] [ft lb s ²]	1.7 1.3	2.9 2.1	5 3.7	8.4 6.2	11.2 8.2
Weight [kg] [lb]	12 26	16.5 36	21 46	26 57	36 79